2D OXIDE DIELECTRIC NANOSHEETS STRUCTURED NANOFILMS FOR ULTRATHIN, FLEXIBLE, TRANSPARENT CAPACITOR FABRICATION AND BIOLOGICAL APPLICATIONS

BEGÜMNUR KÜÇÜKCAN

Thesis for the Master's Program in Bioengineering

Graduate School

Izmir University of

Economics

Izmir

2024

2D OXIDE DIELECTRIC NANOSHEETS STRUCTURED NANOFILMS FOR ULTRATHIN, FLEXIBLE, TRANSPARENT CAPACITOR FABRICATION AND BIOLOGICAL APPLICATIONS

BEGÜMNUR KÜÇÜKCAN

THESIS ADVISOR: ASSOC. PROF. DR. ÖZGE SAĞLAM
THESIS CO-ADVISOR: ASST. PROF. DR. FATMA PINAR GÖRDESLİ DUATEPE

A Master's Thesis
Submitted to
the Graduate School of Izmir University of Economics
the Department of Bioengineering

Izmir
2024

ETHICAL DECLARATION

I hereby declare that I am the sole author of this thesis and that I have conducted my work in accordance with academic rules and ethical behaviour at every stage from the planning of the thesis to its defence. I confirm that I have cited all ideas, information and findings that are not specific to my study, as required by the code of ethical behaviour, and that all statements not cited are my own.

Name, Surname: Begümnur Küçükcan

Date:03.01.2024

Signature:

ABSTRACT

2D OXIDE DIELECTRIC NANOSHEETS STRUCTURED NANOFILMS FOR ULTRATHIN, FLEXIBLE, TRANSPARENT CAPACITOR FABRICATION AND BIOLOGICAL APPLICATIONS

Küçükcan**,** Begümnur

Master's Program in Bioengineering

Advisor: Assoc. Prof. Dr. Özge Sağlam
Co-Advisor: Asst. Prof. Dr. Fatma Pınar Gördesli Duatepe

January, 2024

In this thesis, Dion-Jacobson (DJ) type $KCa_2NaNb_4O_{13}$ layered materials were synthesized using the solid-state calcination method. $KCa_2NaNb_4O_{13}$ materials were chemically exfoliated to produce colloidal solutions containing $Ca_2NaNb_4O_{13}$ nanosheets. 2.4 nm thick and 3.5 μm lateral size nanosheets were successfully produced in a solution with a $TBA^+:H^+$ molar ratio of 1:16. These nanosheets then deposited on indium tin-oxide – polyethylene terephthalate (ITO-PET), Si, Ti/Au-Si, Ti/Au-glass, and ITO-glass substrates using the Langmuir-Blodgett (LB) deposition technique. Additionally, 10, 15, and 20 layers of nanofilms were deposited onto ITO-PET substrates and patterned with photolithography technique. The patterns deposited with 75 nm ITO thin layer to develop transparent and flexible capacitors with electrodes ranging from 250 x 250 $μm^2$ to 75 x 75 $μm^2$. In capacitors, an increase in the number of dielectric layers led to a decrease in the leakage current values.

Furthermore, $Ca_2NaNb_4O_{13}$ nanosheets-structured nanofilms were patterned using electron beam lithography (EBL) technique and deposited with 15/20 nm Ti/Au on Si, Ti/Au-Si, Ti/Au-glass, and ITO-glass substrates with dimensions ranging from 20 x 20 μm^2 to 250 x 250 nm^2. I-V measurements were performed using the c-AFM. On the other hand, the polar and apolar surface tension components, as well as the work of adhesion of $Ca_2NaNb_4O_{13}$ nanosheets-structured nanofilms on Si and ITO-PET substrates were investigated through contact angle measurements with surface thermodynamics-based mathematical modelling. Thus, nanofilm adhered more on ITO-PET in water. Bacterial biofilm formation on both bare and nanofilm-deposited substrates was studied and analyzed using the crystal violet (CV) staining procedure.

Keywords: Two-dimensional materials, perovskite nanosheets, Langmuir-Blodgett deposition technique, ultra-thin capacitors, surface tension, bacterial biofilm formation.

ÖZET

ULTRA İNCE, ESNEK VE TRANSPARAN KAPASİTÖR ÜRETİMİ VE BİYOLOJİK UYGULAMALAR İÇİN İKİ BOYUTLU OKSİT DİELEKTRİK NANOLEVHALAR İLE YAPILANDIRILMIŞ NANOFİLMLER

Küçükcan**,** Begümnur

Biyomühendislik Yüksek Lisans Programı
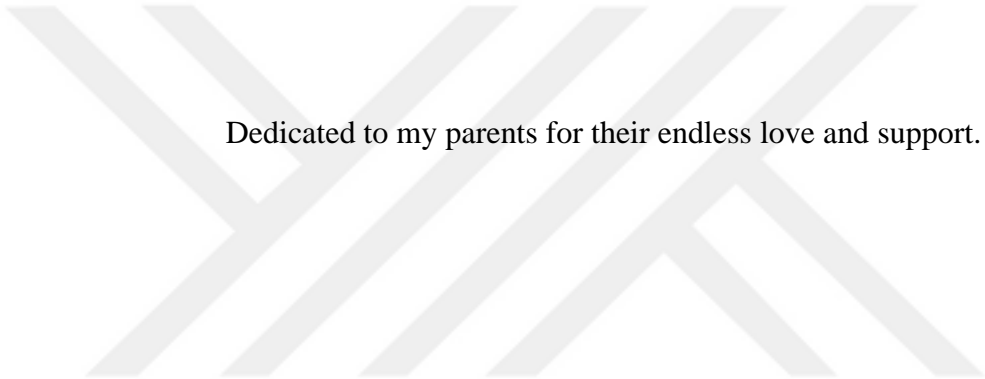
Tez Danışmanı: Doç. Dr. Özge Sağlam
Tez İkinci Danışmanı: Dr. Öğr. Üyesi Fatma Pınar Gördesli Duatepe

Ocak, 2024

Bu tezde, Dion-Jacobson (DJ) tipi $KCa_2NaNb_4O_{13}$ katmanlı malzemeler katı hal yöntemi kullanılarak sentezlenmiştir. $KCa_2NaNb_4O_{13}$ katmanlı malzemelerinin kimyasal pullandırma yöntemi ile 2.4 nm kalınlığında ve 3.5 µm yanal boyutlarında $Ca_2NaNb_4O_{13}$ nanolevhaları içeren kolloidal solüsyonlar elde edilmiştir. Bu kolloidal solüsyonlar arasında $TBA^+:H^+$ oranı 1:16 olan solüsyon nanolevha üretimi için kullanılmıştır. Bu nanolevhalar, Langmuir-Blodgett (LB) kaplama yöntemi kullanılarak indiyum kalay-oksit – polietilen tereftalat (ITO-PET), Si, Ti/Au-Si, Ti/Au-cam ve ITO-cam alttaşları üzerine kaplanmıştır. Ek olarak, 10, 15 ve 20 katmanlı nanofilmler ITO-PET alttaşları üzerine kaplanmış ve optik litografi tekniği kullanılarak desenlenmiştir. Bu desenler, 75 nm kalınlığında ITO ile kaplanarak, 250 x 250 μm^2' den 75 x 75 μm^2' ye kadar değişen boyutlarda şeffaf ve esnek kapasitörler üretilmiştir. 10, 15 ve 20 katmanlı nanofilmlerini içeren kapasitörlerde, dielektrik katman sayısındaki artış, kaçak akım değerlerini azalttığı gözlemlenmiştir. Ayrıca, Si,

Ti/Au-Si, Ti/Au-cam ve ITO-cam alttaşları üzerindeki nanofilmler, elektron demet litografisi (EBL) ile desenlenmiş ve 15/20 nm kalınlığında Ti/Au ile kaplanmıştır. Ti/Au-Si, Ti/Au-cam ve ITO-cam alttaşlar üzerinde de 20 x 20 μm^2' den 250 x 250 nm^2' ye kadar değişen boyutlarda Ti/Au elektrotlar da üretilmiştir. C-AFM ölçümleri ile bu elektrotların I-V analizleri yapılmıştır. Öte yandan, $Ca_2NaNb_4O_{13}$ nanolevhaları ile üretilmiş nanofilmlerin Si ve ITO-PET alttaşları üzerindeki polar ve apolar yüzey gerilimleri, adezyon çalışmaları, yüzey termodinamiği temelli matematiksel modelleme ile hesaplanmıştır. Böylece, nanofilm ile ITO-PET arasındaki artan polar bağlanma, suda daha güçlü bir adezyona sebep olduğu tespit edilmiştir. Hem kaplanmamış hem de nanofilm kaplanmış Si ve ITO-PET alttaşlar üzerindeki bakteriyel biyofilm oluşumu, kristal viyole (CV) boyama yöntemi ile analiz edilmiştir.

Anahtar Kelimeler: İki boyutlu malzemeler, perovskite nanolevhalar, Langmuir-Blodgett kaplama yöntemi, ultra-ince kapasitörler, yüzey gerilimi, bakteriyel biyofilm oluşumu

Dedicated to my parents for their endless love and support.

ACKNOWLEDGEMENTS

TABLE OF CONTENTS

LIST OF TABLES

LIST OF FIGURES

LIST OF ABBREVIATIONS

DJ – Dion-Jacobson

RP – Ruddlesden-Popper

AU - Aurivillus

TBA^+ - Tetra-n-butylammonium ion

H^+ - Hydrogen ion

ITO-PET – Indium Tin Oxide-Polyethylene Terephthalate

LB – Langmuir-Blodgett

EBL – Electron Beam Lithography

AFM - Atomic Force Microscopy

c-AFM – Conductive Atomic Force Microscopy

CV – Crystal Violet

d^0 – State in transition metals, meaning d orbital is empty

ε_r – Dielectric constant

TiO_2 – Titanium dioxide

HfO_2 – Hafnium dioxide

Al_2O_3 – Aluminum oxide

$(Ba_{1-x}Sr_x)TiO_3$ – Barium strontium titanate, x represents the possible variations of composition ratio between Ba and Sr.

2D – Two-dimensional

h-BN – Hexagonal boron nitrides

TMDCs – Transition metal dichalcogenides

κ – Kappa symbol

$\tan\delta$ – Tangent of the dielectric loss angle

$\mu F/cm^2$ – Microfarads per square centimeter, capacitance density

nm – Nanometer

DFT – Density Functional Theory

ωTO – Transverse Optical Phonon Frequencies

ωL – Lowest Phonon Frequencies

GO – Graphene Oxide

E. coli – Escherichia coli

S. aureus – Staphylococcus aureus

$\mu g/mL$ – Micrograms per milliliter

Ag^+ - Silver ion

Tm/Er – Thulium/Erbium elements

Si – Silicon

SiO_2 – Silicon dioxide

EUV – Extreme Ultraviolet

FIB – Focused Ion Beam

UV – Ultraviolet

MEMS – Micro-Electro-Mechanical Systems

ICs – Integrated Circuits

CPU – Central Processing Unit

SEM – Scanning Electron Microscopy

K_2CO_3 – Potassium carbonate

$CaCO_3$ – Calcium carbonate

Na_2CO_3 – Sodium carbonate

Nb_2O_5 – Niobium (VI) oxide

°C – Degrees Celsius

h – Hour

min – Minute

K^+ - Potassium ion

HNO_3 – Nitric acid

rpm – Revolutions per minute

$M\Omega$ – Megaohms

TBAOH – Tetrabutylammonium Hydroxide

wt% - Weight Percent

H_2O – Water

mL – Milliliter

g – Gram

ITO-glass – Indium Tin Oxide deposited glass

Ti/Au-glass – Titanium/Golden deposited glass

Ti/Au-Si – Titanium/Golden deposited Silicon

CH_3COCH_3 – Acetone

CH_3CH_2OH – Ethanol

$CH_3CH(OH)CH_3$ – Isopropanol

γ – Surface tension

Ө - Theta

HM – Harmonic Mean

µL – Microliter

CH_2I_2 – Diiodomethane

γ^p_L – Polar component of the surface tension for the liquid

γ^d_L – Dispersive (apolar) component of the surface tension for the liquid

γ^p_S – Polar component of the surface tension for the substrate

γ^d_S - Apolar component of the surface tension for the substrate

γ_L – Total surface tension of the liquid

γ_S – Total surface tension of the substrate

mJ/m^2 – Millijoules per square meter, unit of surface energy

W_{adh} – Work of adhesion

$S1$ – $Ca_2NaNb_4O_{13}$ nanosheets-structured Langmuir-Blodgett nanofilms

$S2$ – Bare Si and ITO-PET substrates

W^p_{adh} – Work of polar adhesion

W^d_{adh} – Work of dispersive adhesion

UV/Vis – Ultraviolet/Visible, a type of spectroscopy

PMMA A4/A2 – Polymethylmethacrylate A4/A2

kV – Kilovolt

pA – Picoampere

µm – Micrometer

$µC/cm^2$ – Microcoulombs per square centimeter

EHT – Electron High Tension

AZ5214E – A specific type of negative photoresist

AZ400K – A specific developer solution used in photolithography

mW/cm^2 – Milliwatts per square centimeter

I – Current, unit is ampere

V – Voltage, unit is volt

C – Capacitance, measured in Farads

Hz – Hertz, frequency unit

kHz – Kilohertz

MHz – Megahertz

ITO – Indium Tin Oxide

d – Thickness of the dielectric layers, measured in meters

S – Area of the electrode, measured in square meters

ε_0 – Permittivity of the vacuum, measured in Farads per square meter

v/v – Volume per volume

H_2SO_4:H_2O_2 – Sulfuric acid and hydrogen peroxide, piranha solution

PS – Polystyrene

XRD – X-ray Powder Diffraction

Cu Kα radiation – Copper K-alpha radiation

XPS – X-ray Photoelectron Spectroscopy

EDX – Energy-Dispersive X-ray Spectroscopy

eV – Electron Volt

S_a – Arithmetic Mean Roughness

S_q – Root Mean Square Roughness

DM – Diiodomethane

A/cm^2 – Ampere per square centimeter, leakage current unit

CHAPTER 1: INTRODUCTION

1.1. Layered Perovskites

Layered perovskites have ABO_3 crystal structure made up of BO_6 octahedral units. Cations are located between the host layers created by these BO_6 units. These cations, connected to the BO_6 units by electrostatic interactions are ionically exchangeable (Rondinelli et al., 2012).
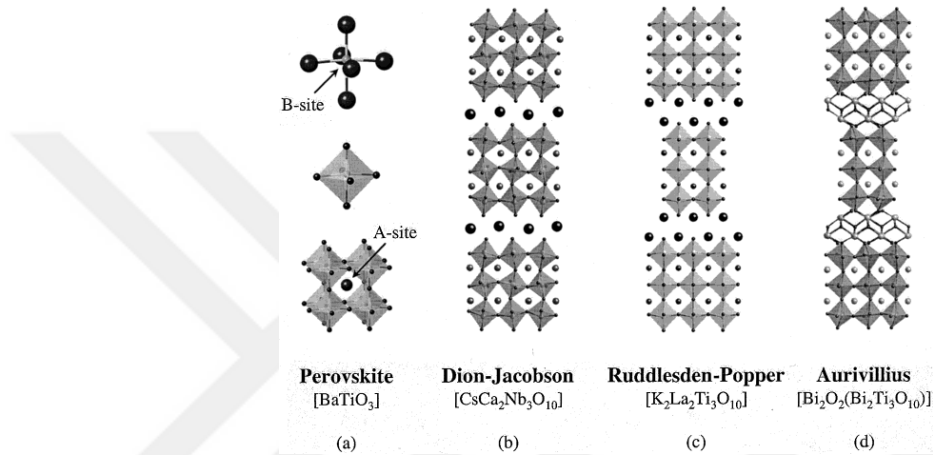
Figure 1. Schematic representation of crystal structures of layered perovskites (a) octahedral unit and BO_6 octahedral units combined with corner sharing, (b) Dion-Jacobson (DJ) type layered perovskite crystal structure, (c) Ruddlesden-Popper (RP) type layered perovskite crystal structure, (c) Aurivillius (AU) type layered perovskite crystal structure. (Source: Schaak and Mallouk, 2002).

Layered perovskites can be divided into three distinct classes, as represented in Figure 1. These classes are: (a) DJ type, denoted by the formula $A[A'_{n-1}B_nO_{3n+1}]$, (b) RP type, represented by $A_2[A'_{n-1}B_nO_{3n+1}]$, and (c) AU type, expressed as $(Bi_2O_2)[A_{n-1}(B)_nO_{3n+1}]$. In these formulas, A indicates alkali metal cations that can be exchanged between layers. A' represents either alkaline earth metals or lanthanides located between the octahedral BO_6 units, and B stands for the transition metals such as Nb^{5+}, Ta^{5+}, Ti^{4+} or Mn^{4+}, which are located in the center of these octahedral units. The term "n" specifies the number of BO_6 octahedral units in the matrix. The host layers of layered perovskite structures carry a negative charge and are held together by cations, serving as intermediary layers that determines the differences among these

1

three phases. Alterations in these intermediary layers affect the chemical structure and characteristics of layered perovskites. For the DJ and RP phases, the spatial arrangement of the atoms in the interlayer defines the perovskites' ion exchange and linkage capacities (Schaak and Mallouk, 2002). Typically, these atoms within the interlayer are alkaline salt cations, with the unique distinction between these phases arising from an alkaline cation in the empirical formula.

Perovskite oxides exhibit various properties such as dielectric (Yang et al., 2020), ferroelectric (Gao et al., 2020), and piezoelectric (Nan et al., 2019). Thus, they are utilized in applications like capacitors (Kim et al., 2000) and memory devices (Liu et al., 2018), as well as in energy storage systems (Hussain et al., 2017). However, when the thickness of perovskite oxide thin films is dropped below to a certain nanometer, size-dependent effects arise that negatively affect the dielectric and ferroelectric properties of these films, leading to an increase in leakage current (Kim et al., 2000; Junquera and Ghosez, 2003). Therefore, the anticipated characteristics of the thin films become unobservable, disabling its functionality. Nevertheless, these challenges are not encountered in perovskite oxide nanosheets derived from layered perovskites. Owing to the d^0 transition metals in their B regions, these dielectric perovskite oxide nanosheets are insulating and exhibit a wide band-gap (Ebina et al., 2012; Kim et al., 2016). Moreover, to overcome the 'dead layer' problem, dielectric perovskite oxide nanosheets can be assembled layer-by-layer using bottom-up methods, fabricating nanofilms that maintain their dielectric properties (Osada et al., 2010).
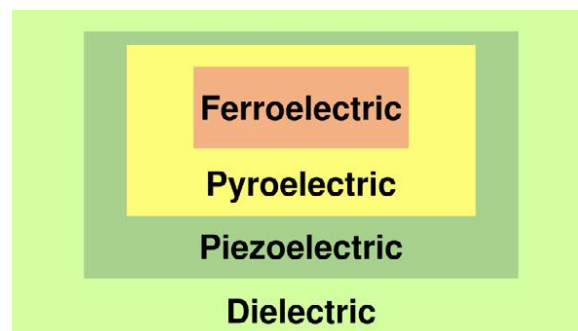
Figure 2. Classification of dielectric materials (Source: Sekine et al., 2022).

Dielectric materials can be divided into two main categories: metal oxides with centrally symmetric (non-polar) atomic arrangements and ferroelectric/perovskite materials exhibiting anisotropic behaviours with high dielectric structures ($\varepsilon_r > 1000$) [See in Figure 2]. Examples of metal oxides include compounds such as TiO_2, HfO_2, and Al_2O_3. Notably, HfO_2 has become commercially essential in modern electric devices (Müller et al., 2015). However, despite their low loss attributes, these oxides do not always achieve high dielectric expectations ($\varepsilon_r < 100$). In contrast, ferroelectric/perovskite materials have high dielectric properties due to their anisotropic structure. For instance, oxides like $(Ba_{1-x}Sr_x)TiO_3$ are ferroelectric due to their significant static dipole moments. Additionally, oxide materials with high dielectric constants can be produced using the atomic layer deposition technique. Yet, producing these materials in the ultra-thin region (< 20 nm) can lead to dielectric breakdown due to size-related effects (Chen et al., 2006). Therefore, two-dimensional (2D) materials are considered to be a strong alternative against miniaturization problems. Advancements in 2D materials, including graphene (Novoselov et al., 2004; Novoselov et al., 2005), hexagonal boron nitrides (Knobloch et al., 2021; Zhang et al., 2017), and transition metal dichalcogenides (Manzeli et al., 2017; Choi et al., 2017) are paving the way for miniaturizing devices across broad range of applications.

1.2 Two-Dimensional Oxide Nanosheets

Two-dimensional (2D) oxide materials gained an interest after the isolation of graphene in 2004 (Novoselov et al., 2004). Since then, 2D oxide materials considered to be the good alternatives for silicon-based technologies. Unlike graphene, which is produced by mechanical exfoliation, 2D oxide nanosheets are derived by chemically exfoliating layered oxide materials. These nanosheets exhibit various properties due to their unique structural and functional characteristics, including dielectric (Li et al., 2010), magnetic (Jantsky et al., 2014), optical (Wang et al., 2018), superconducting (Ogino et al., 2009), and photocatalytic (Shimizu et al., 2018) properties. Their thickness can vary from 1 nm to a few nanometers, with their lateral area can reach up to 10 μm.

Exfoliation process involves separating layered materials into single layers. This method has been effectively applied to materials like layered perovskites, titanium

oxides, and manganese oxides to produce 2D single layers (Ma and Sasaki, 2015). The separation into nanometer-thin single layers is through protonation process requiring the interaction of large molecule solvents with hydrogen atoms in the intermediary layers (Osada and Sasaki, 2009). Furthermore, producing nanofilms by nanosheets can be integrated with metal complexes, polyions, and beam epitaxy to create hybrid materials, the design of superlattice structures, and the fabrication of devices. Layer-by-layer and flocculation methods, often referred to as beaker epitaxy, can produce nanofilms consist of these 2D nanosheets. Particularly, the layer-by-layer method which is an electrostatic sequential adsorption technique, is effective for producing nanometer-scale composite films. This wet chemical process is not only methodologically straightforward, cost-effective, and eco-friendly compared to beam epitaxy, but it also provides researchers an opportunity to work at atomic scale. Perovskite nanosheets, one of the members of the 2D family of materials obtained by the chemical exfoliation of layered perovskites, demonstrate various properties including high – κ dielectric (Kim et al., 2016; Khan et al., 2020; Zhang et al., 2022), photocatalytic (Jiang et al., 2017; Zheng et al., 2021), photoluminescence (Gunay et al., 2021; Gunay et al., 2022), electrochemical (Xiong et al., 2019; Majee et al., 2020), and ferroelectric (Osada et al., 2017; Khan et al., 2020). Furthermore, nanofilms made of 2D perovskite nanosheets having highly orderly morphology exhibit high dielectric characteristics (Osada et al., 2008).

Osada and Sasaki (2018) developed a novel solution-based, bottom-up method for producing $Ca_2Nb_3O_{10}^-$ nanosheets-structured nanofilms derived from DJ type layered perovskites for dielectric/electrode applications. The multilayered films composed of $Ca_2Nb_3O_{10}^-$ nanosheets consistently exhibited a dielectric constant (ε_r) of about 210, regardless of their thickness, with a dielectric loss ($\tan\delta$) between 2-5%. Notably, in ultra-thin regions (< 20 nm), these 2D perovskite nanosheets surpassed perovskite-structured thin films in terms of ε_r values. The dielectric constants of both $Ca_2Nb_3O_{10}^-$ and $Sr_2Nb_3O_{10}^-$ nanosheets exceeded 200. This indicates that nanofilms composed of 2D nanosheets hold significant potential as their dielectric properties remain constant, irrespective of size. Further studies by Osada et al. (2008 & 2011) and Li et al. (2011) have reinforced these findings, showing that multilayer films from various nanosheets maintain stable dielectric characteristics, even at 10 nm thickness.
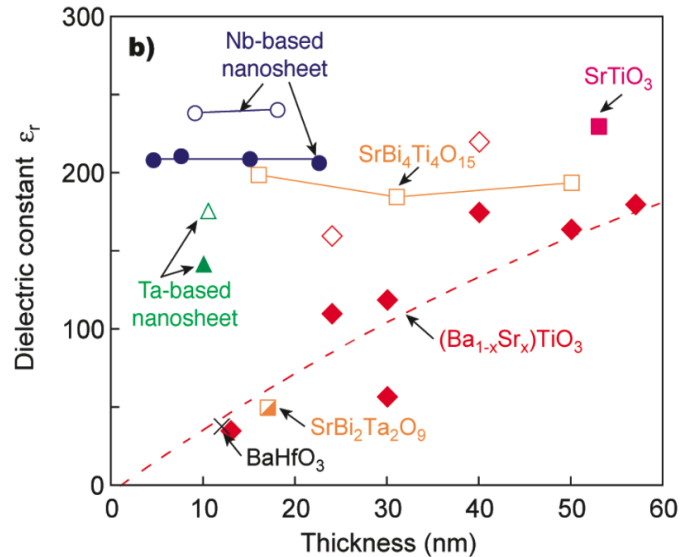
Figure 3. Dielectric constant (ε_r) values of perovskite nanosheets and perovskite thin films (Source: Osada et al., 2010).

Figure 3 presents a comparative analysis of the ε_r values between perovskite nanosheets and various perovskite-structured thin films (Osada et al., 2010). In the ultra-region (< 20 nm), the ε_r value for perovskite nanosheets exceeds that of other perovskite thin films. Specifically, $Sr_2Nb_3O_{10}$ and $Ca_2Nb_3O_{10}$ nanosheets exhibit ε_r values that are ten times greater than those of $(Ba_{1-x}Sr_x)TiO_3$ films of identical thickness, reaching values above 200. Unlike the dielectric collapse observed in $(Ba_{1-x}Sr_x)TiO_3$ due to size-related effects, the high ε_r values of perovskite nanosheets remain constant, even below 10 nm. These results indicate that perovskite nanosheets are suitable materials for thin capacitors with high storage capacity.

In a study developing ultra-thin capacitors based on 2D oxide nanosheets, the Langmuir-Blodgett method was employed to deposit $Ca_2Nb_3O_{10}^-$ nanosheets onto $SrRuO_3$ substrate to produce sandwich-like structure with the alignment of metallic and dielectric layers (Wang et al., 2014). Impressively, the developed ultra-thin capacitor for this study exhibited a capacitance density of approximately 30 $\mu F/cm^2$, even at a nanofilm thickness of 28 nm. This performance significantly surpasses commercial $BaTiO_3$ capacitors by around 2000-fold, which offer about a capacitance density of 20 $\mu F/cm^2$ at a 5×10^4 nm thickness, and is almost tenfold greater than HfO_2-based ultra-thin capacitors which have a capacitance density of approximately 0.9 $\mu F/cm^2$ at 10 nm thickness.

In another study conducted by Li et al. (2017), focused on the dielectric and ferroelectric properties of $Ca_2Na_{n-3}Nb_nO_{3n+1}$ nanosheets. They discovered that these properties are directly influenced by the modification of the 'n' in the structure of the layered material. When 'n' was set at 6, the dielectric constant reached a high value of around 470, the highest among the ultra-thin dielectric materials. However, the lowest leakage current value of $\sim 10^{-9}$ A/cm^2 was observed at 0.5V when 'n' was at 4, attributed to the fact that these nanosheets have the largest lateral area. Furthermore, the study highlighted the value of ε_r, is dependent on 'n', which represents the BO_6 octahedral units positioned along the z-axis. This observation was theoretically endorsed by density functional theory (DFT) calculations. These calculations unfolded the n-dependent changes between the squares of the polar phonon frequencies (ωTO) for $Ca_2Na_{n-3}Nb_nO_{3n+1}$ nanosheets and the lowest phonon frequencies (ωL) for their layered form, $KCa_2Na_{n-3}Nb_nO_{3n+1}$. The softening in ($\omega L$) was found to be the cause of increase in the ε_r, which was due to the continuous linkage of -B-O-B- bonds along the layers of layered perovskites. This correlation was further confirmed in the $Ca_2Na_{n-3}Nb_nO_{3n+1}$ nanosheets' ωTO frequency, revealing that an increase in 'n' and the softening of ωTO frequencies were the factors leading to an increase in the dielectric constant, ε_r.

1.2.1. Physicochemical surface characteristics and biological applications of 2D oxide nanosheets

2D oxide nanosheets are emerging as versatile materials due to their unique physicochemical properties and potential in biological applications. Ultra-thin, and with a high surface area, these nanosheets exhibit exceptional mechanical and electronic properties, offering advantages in strength, flexibility, and chemical stability. To understand the interaction of 2D oxide nanosheets or their coatings with other materials, contact angle measurements are essential (Zhang et al., 2019). Furthermore, physicochemical characterization can support the understanding of how these materials interact within biological environments (Yadav et al., 2017; Choudhary et al., 2019).

In biological contexts, 2D oxide nanosheets possess adaptable surface characteristics making them suitable for various biological applications including targeted drug delivery (Yadav et al., 2018) and biosensing, thanks to their electronic properties. Moreover, they have shown potential in cancer treatments, specifically in photothermal therapy (Yin et al., 2017). They can also serve as contrast agents in imaging techniques (Zhang et al., 2015; Chawda et al., 2019), exhibit antimicrobial properties (Liu et al., 2011; Perreault et al., 2015), and contribute to advancements in tissue engineering (Tang et al., 2019; Zheng et al., 2021).

In a study, graphene oxide (GO) was coated onto a polymer substrate to investigate its antimicrobial activity against gram-negative *Escherichia coli (E. coli)* and gram-positive *Staphylococcus aureus (S. aureus)*. (Liu et al., 2018). The findings revealed that these coatings were more effective against *E. coli*, compared to *S. aureus.* It was stated that the primary mechanism for the antibacterial activity was oxidative stress, rather than physical or mechanical cell damage. This effectiveness is attributed to smooth and edge-free characteristics of the coatings. In a different study, the antibacterial activity of GO coated surfaces prepared by two methods was investigated (Yadav et al., 2017). The functional groups of GO, as well as the nanosheets size and roughness of the nanosheets, were identified as key factors inhibiting both *E. coli* and *S. aureus*. The study noted enhanced bacterial adhesion observed on coatings that were rougher and less uniformly thick. When discussing the antibacterial activity of 2D oxide nanosheets or their coatings on the substrates, GO sheets are often used due to their excellent antimicrobial property. However, in notable research, Günay et al. (2022) demonstrated antibacterial and antibiofilm capabilities of Ag^+ intercalated Tm/Er co-doped layered perovskites and their 2D single oxide nanosheets against *Escherichia coli* and *Bacillus subtilis* pathogens. Their findings revealed that, at a concentration of 100 µg/mL, nanosheets combined with Ag^+ ions exhibited strong antibacterial and antibiofilm activity.

In this thesis, the bacterial biofilm formation of 2D oxide nanosheets-structured nanofilms on Si and ITO-PET substrates was studied, building upon our previous work on the physicochemical characterization of 2D oxide nanosheets on Si and ITO-PET substrates (Küçükcan et al., 2023).

1.3 Langmuir-Blodgett Deposition Technique

The Langmuir-Blodgett (LB) method, a type of thin film deposition technique, is applied to coat amphiphilic molecules that floats on water onto a solid substrate. The LB method is a straightforward and effective method to assemble 2D oxide nanosheets. Using this deposition technique, nanofilms can be piled up by the assembling the 2D oxide nanosheets to a specified thickness, leading to uniformly structured nanofilms (Osada et al., 2008) as shown in Figure 4. Applying this deposition technique sequential manner allows for the layer-by-layer assembly of nanofilms made up of single-layer nanosheets (Akatsuka et al., 2009; Yim et al., 2021).
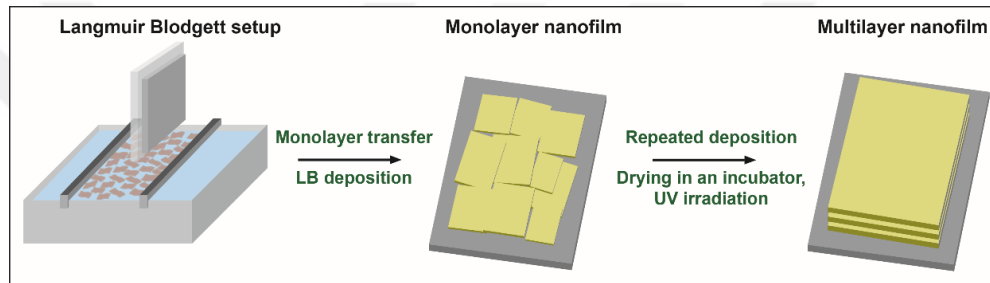
Figure 4. Schematic illustration for multi-layered 2D oxide nanosheet films using the LB deposition technique (Source: Osada et al., 2008).

The LB method involves creating nanosheets-structured uniform monolayer nanofilm on the air-liquid interface in an LB trough. This is achieved by pushing the barriers together to ensure a densely packed structure. Subsequently, using a vertical dipping LB method, this monolayer containing nanosheets can be layered onto hydrophobic substrates such as Si and ITO-PET substrates (Küçükcan et al., 2023). Up to now, various 2D perovskite nanosheets have been deposited onto conductive ITO-glass substrates employing this LB method (Muramatsu et al., 2005).

1.4. Ultra-Thin Capacitors

Flat-panel displays developed on transparent and flexible substrates are vital for wearable electronic device applications because of their distinct characteristics, such as high optical clarity, flexibility, and lightness. Meanwhile, capacitors are considered to have a significant role in electric and electronic engineering technologies, especially

when it comes to performing quick charge and discharge functions within the pixel driver circuits of flat panel displays (Chen et al., 2004). For each pixel to display its color brightness, capacitors should have high capacitance and low leakage current values. This allows for longer charge retention (storage time) when the pixel is in the off state (Nomura et al., 2006). The capacitors produced for wearable electronic devices should be ultra-thin, optically transparent, and should offer flexibility. Furthermore, while having these properties, it is crucial for the capacitors to keep their capacitance levels.

With technological advancements, the number of transistors in integrated circuits are expected to double roughly every two years (Moore, 1965; Moore, 1975). If the current silicon-based technology continued to be relied upon, there will be miniaturization issues in electronic circuit elements. This issue has led researchers to explore nanotechnology and nanomaterials as potential candidates for silicon-based technology. One of the objectives of these advancements was to develop more compact capacitors with high capacitance (Evangelou et al., 2006).

Researchers are extensively working on thin-film capacitors structured by high-dielectric materials as an alternative to silicon-based technologies for applications like flexible flat-panel displays, dynamic random-access memories (Scott, 1998), non-volatile memories (Lu et al., 2005), and tunable devices (Im et al., 2000). Typically, the oxide layer beneath a transistor's gate is composed of SiO_2. However, with a gate length of 60 nm, the oxide thickness drops below a crucial ~1.5 nm threshold. This drop results in problems such as quantum capacitance and leakage current in the oxide layer (Huff et al., 2005). Therefore, high dielectric materials can be used to further reduce gate length in transistors.

1.5. Lithography Techniques

Lithography is the process used in both microfabrication and nanofabrication to pattern parts of a thin film or the substrates. The patterns are transferred onto a substrate with dimensions ranging from micrometers down to nanometers. The lithographic techniques, when combined with other fabrication processes like deposition and etching, enable the production of high-resolution topographies. These processes can be reiterated multiple times to produce complex micro/nanoscale

devices including integrated circuits, sensors, and nanophotonic structures (Pimpin and Srituravanich, 2012).
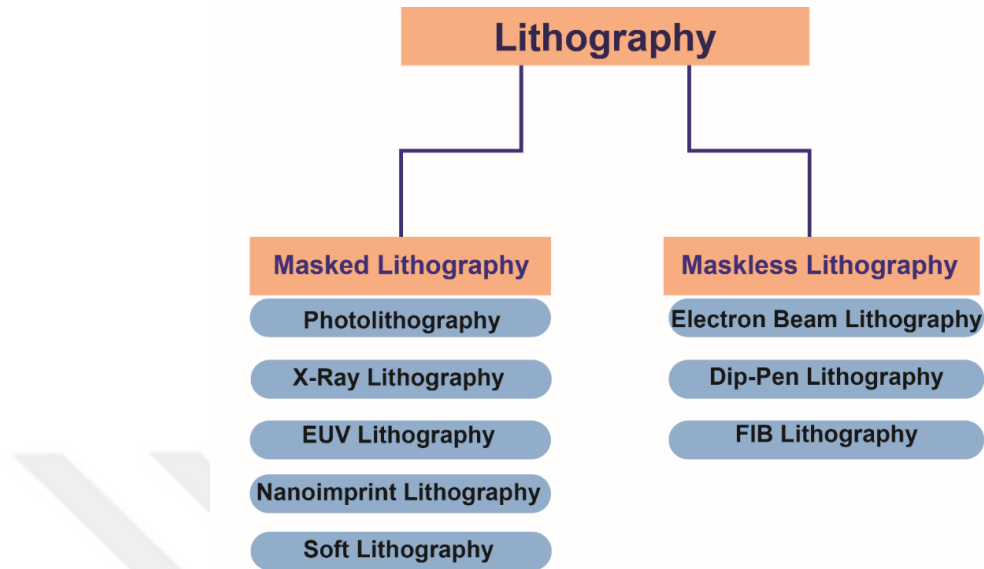
Figure 5. Schematic representation of lithographic techniques.

The lithographic techniques can be divided into two groups which are masked lithography and maskless lithography [See in Figure 5]. The masked lithography techniques are photolithography (Chiu and Shaw, 1997), x-ray lithography, extreme ultraviolet (EUV) lithography, nanoimprint lithography, and soft lithography. On the other hand, the maskless lithography techniques are electron beam lithography (EBL), dip-pen lithography, and focused ion beam (FIB) lithography (Menon et al., 2005). These techniques have been developed to achieve various levels of resolution, throughput, and cost-effectiveness, depending on applications' requirements. In this thesis, photolithography and EBL techniques were employed to produce ultra-thin transparent capacitors made-up of 2D oxide dielectric nanosheets structured nanofilms.

1.5.1. Photolithography

Photolithography is a fundamental process in semiconductor manufacturing and nanofabrication using ultraviolet (UV) light to transfer a pattern from a photomask to a light-sensitive polymer (photoresist) on a substrate (Madou, 2002). The interaction of UV light with the photoresist causes a chemical alteration, allowing the exposed or

non-exposed areas to be selectively removed by a developer solution [See in Figure 6 (a)]. The remaining parts of patterned resist can then serve as a temporary mask for following steps like etching or deposition to fabricate various micro/nanoscale structures (Pimpin and Srituravanich, 2012).
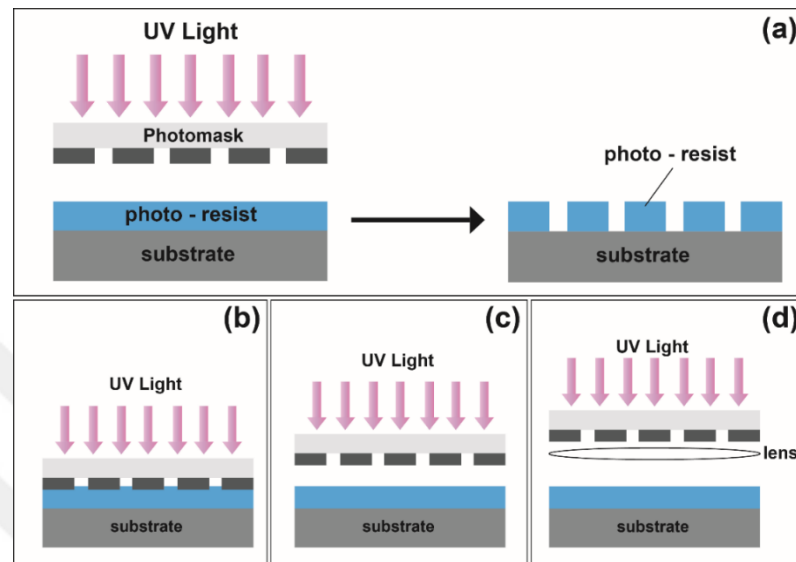
Figure 6. (a) Schematic illustration of photolithography, three types of photolithography (b) contact printing, (c) proximity printing, and (d) projection printing (Source: Pimpin and Srituravanich, 2012).

Figure 6 (a) represents the general steps of photolithography, which are UV exposure and development. There are three types of photolithography techniques: contact printing shown in Figure 6 (b), proximity printing represented in Figure 6 (c), and projection printing method shown in Figure 6 (d). Contact printing and proximity printing can be achieved when the photomask contacted with the resist or in a very close proximity like a few micrometers, respectively. Typically, these methods have a minimum feature size as 2-3 μm (Madou, 2002). Their throughput is very high and they can be used for production of various micro-electrochemical system (MEMS) devices. On the other hand, projection printing, often referred to as a "stepper", uses an optical lens system to project a deep-UV from an excimer laser (with a wavelength of either 193 or 248) onto the photoresist. This allows for a pattern size reduction of 2-10 times, making it possible to produce high-resolution patterns down to sizes as tiny as a few tens of nanometers (37 nm) (Gates et al., 2005). Also, projection printing has very high throughput which can have a production of 60-80 wafers/hr., can be

employed for advanced electronics including advanced integrated circuits (ICs), central processing unit (CPU) chips (Pease and Chou, 2008).

1.5.2. Electron beam lithography

Electron beam lithography (EBL) is a specialized technique used in semiconductor manufacturing and nanofabrication. EBL directly writes custom patterns onto a substrate coated with an electron-sensitive resist using a focused beam of electrons instead of using light to project patterns as photolithography. The interaction of the electrons with the resist induces chemical changes, allowing for either exposed or non-exposed areas to be developed away (Altissimo, 2010).

EBL is known for its high resolution, capable of defining structures at the nanometer scale. However, EBL writes one point at a time since it is a serial writing process, it tends to be slower and more resource-intensive than photolithography (Pease and Chou, 2008). Despite this, EBL has an ability to achieve extremely fine patterns to be used in applications where high resolution is required. These applications are varying from mask fabrication (Menon et al., 2005), production of ICs (Pfeiffer, 2010), to patterning of photonic crystals (Wang et al., 2009; DeRose et al., 2008) and nanofluidic channels (Baba et al., 2003).
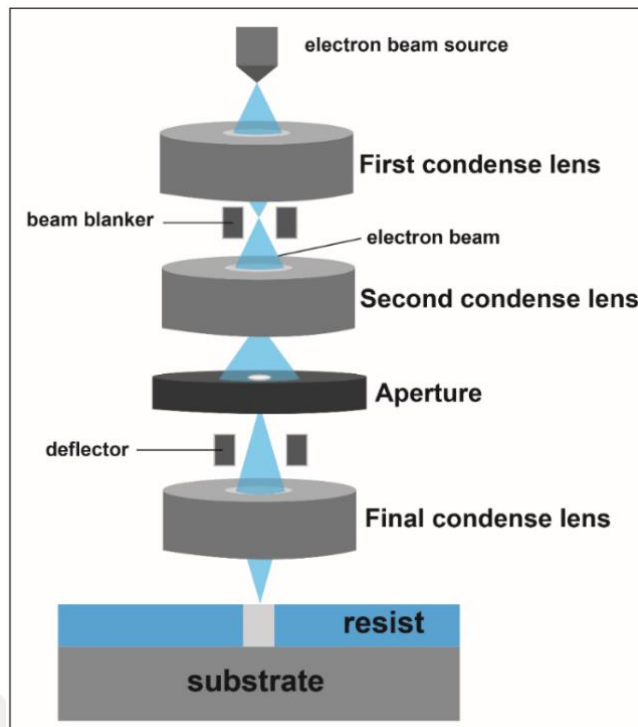
Figure 7. Schematic illustration of EBL: A concentrated electron beam targets the resist to pattern by exposing point by point (Source: Pimpin and Srituravanich, 2012).

As seen in Figure 7, EBL system consists of several essential components including electron source to produce a stream of electrons, electron column compromising series of electromagnetic lenses and apertures designed to focus and shape the electron beam, beam blanker to deflect the electron beam on and off allowing for precise control of where the electron beam exposes the resist, and deflection system made up of electromagnetic coils or plates to guide and scan the electron beam across the substrate in a controlled manner. EBL process takes place in a high vacuum to prevent beam scattering and ensure the electron beam's purity. The substrate is positioned at the stage, and detector system monitors the EBL operation. This entire system is controlled by a computerized control system (Altissimo, 2010).

Previously, EBL was notably expensive. However, recent advancements have enabled the conversion of scanning electron microscopes (SEM) into EBL systems, making them more accessible in fabrication processes (Raith, 2011). This modification permits precise scanning of electron beam spots to produce nanoscale patterns, effectively transforming SEM into EBL systems (Pimpin and Srituravanich, 2012).

CHAPTER 2: MATERIALS AND METHODS

2.1. Synthesis of Layered Perovskites

In this thesis, DJ-type layered perovskites, represented as $KCa_2NaNb_4O_{13}$, were synthesized using the solid-state calcination method. $KCa_2NaNb_4O_{13}$ layered perovskite was synthesized by mixing potassium carbonate (K_2CO_3, Sigma-Aldrich 99.99%), calcium carbonate ($CaCO_3$, Sigma-Aldrich 99.99%), sodium carbonate (Na_2CO_3, Sigma-Aldrich 99.99%), and niobium (VI) oxide (Nb_2O_5, Sigma-Aldrich 99.99%) in stoichiometric amounts in an agate mortar for 30 minutes. The mixture was then annealed in a muffle furnace at 1200 °C for 12h with a heating rate of 10 °C/ min (Knyazev et al., 2019).

Table 1. Synthesis conditions of DJ-type perovskites

Layered Perovskite	Chemicals	Amount (g)	Synthesis Conditions
$KCa_2NaNb_4O_{13}$	K_2CO_3	0.14325 (50% excess)	(i) 1200 ℃ - 12 h (30 ℃/ min)
	$CaCO_3$	0.277	
	Na_2CO_3	0.1095 (50% excess)	
	Nb_2O_5	0.736	
$KCa_2NaNb_4O_{13}$	K_2CO_3	0,0955	(ii) 1200 ℃ - 12 h (30 ℃/ min) (iii) 1200 ℃ - 12 h (10 ℃/ min)
	$CaCO_3$	0,277	
	Na_2CO_3	0,073	
	Nb_2O_5	0,736	

As shown in Table 1, for synthesizing the DJ-type $KCa_2NaNb_4O_{13}$ layered perovskite, an excess 50% of K_2CO_3 and Na_2CO_3 have been added to the mixture due to their volatilization at high temperatures. Moreover, $KCa_2NaNb_4O_{13}$ layered perovskite annealed at (i) 1200 °C for 12 hours, with a 30 °C/ min heating rate. Similarly, the synthesis of layered $KCa_2NaNb_4O_{13}$ material, conducted without any excess K_2CO_3 and Na_2CO_3 and annealed at two different conditions: (ii) and (iii) (See in Table 1).

2.2. Synthesis of 2D Oxide Nanosheets

2.2.1. Ion exchange procedure of layered perovskites

The ion exchange, or protonation procedure, is the initial stage of nanosheet synthesis. During protonation, K^+ ions located between the layers are replaced with H^+ ions from an acid solution. Thus, treating layered perovskites with this acid solution elevates the acidity level of the layers, preparing layered perovskites for the exfoliation stage (See in Figure 8).
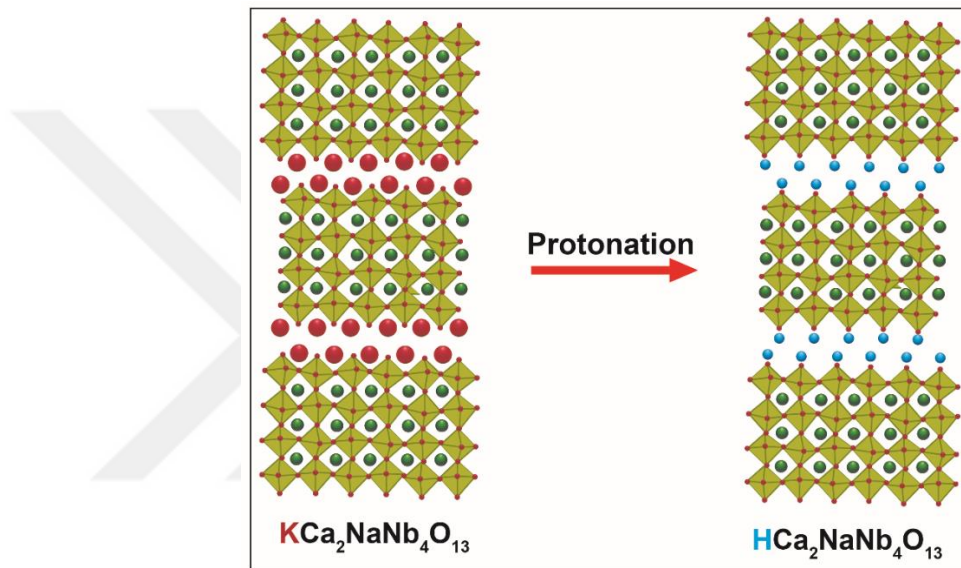
Figure 8. Schematic illustration of protonation procedure (Source: Li et al., 2017).

To obtain the protonated form of $KCa_2NaNb_4O_{13}$ material, 5 g of the layered material was treated with 200 mL 5 M nitric acid (HNO_3, Sigma Aldrich 70% purity) for 4 days at room temperature on an orbital shaker at 130 rpm (Shangguan and Yoshida, 2001). Then, the protonated form, $HCa_2NaNb_4O_{13}$, was repeatedly cleaned with ultra-pure water (resistivity of 18.2 MΩ, from Stakpure Omnia Tap 6) and left to dry in an incubator at 60 °C overnight.

2.2.2. Exfoliation procedure of layered perovskites

The second stage of nanosheet synthesis is called as the exfoliation procedure. In this stage, the ionic interaction force between the layers of layered oxide materials with high charge densities was reduced using tetrabutylammonium hydroxide (TBAOH -

(C_4H_9)$_4$NOH - Sigma Aldrich 40 wt% in H_2O) solution. This led to the separation of the crystalline layers and the formation of single oxide nanosheets (See in Figure 9). Solutions derived from this procedure are termed colloidal solutions.
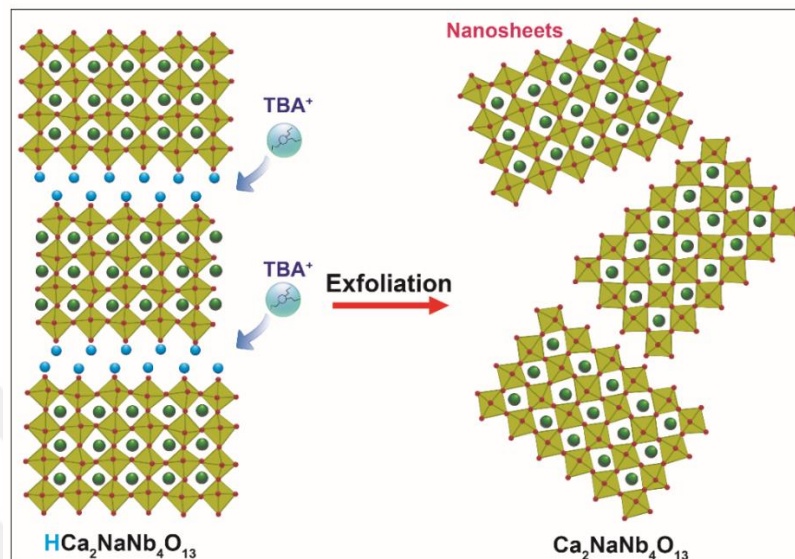
Figure 9. Schematic illustration of exfoliation procedure.

Table 2. Exfoliation parameters of $Ca_2NaNb_4O_{13}$ single oxide nanosheets

Protonated material	Exfoliation Parameters	Exfoliation Procedure	TBA$^+$:H$^+$ molar ratios
$HCa_2NaNb_4O_{13}$	0.1 g protonated layered material + 20 mL TBAOH solution	2 h shaking, 20 h precipitation	8:1
		7 h shaking, 20 h precipitation	8:1
$HCa_2NaNb_4O_{13}$	0.1 g protonated layered material + 20 mL TBAOH solution	4 h shaking at 100 rpm, 24 h precipitation	16:1
			8:1
			4:1
			2:1
			1:1
			1:2
			1:4
			1:8
			1:16

In Table 2, colloidal solutions of $Ca_2NaNb_4O_{13}$ single oxide nanosheets were prepared by using 0.1 g of the protonated material in a combined 20 mL volume of ultra-pure water and TBAOH solution. These solutions were produced at different $TBA^+:H^+$ molar ratios. Initially, to obtain $Ca_2NaNb_4O_{13}$ single oxide nanosheets in a colloidal solution, 0.1 g of protonated $HCa_2NaNb_4O_{13}$ layered material was mixed in a 20 mL volume of ultra-pure water and TBAOH at a $TBA^+:H^+$ ratio of 8:1. This mixture was shaken on an orbital shaker for 2 hours and 7 days. Then, the solution was precipitated for 20 hours (Yuan et al., 2016).

Similarly, colloidal solutions containing $Ca_2NaNb_4O_{13}$ single oxide nanosheets were produced by taking 0.1 g of $HCa_2NaNb_4O_{13}$ layered material in a 20 mL mixture of ultra-pure water and TBAOH solution and shaking at 100 rpm on an orbital shaker for 4 days. The molar ratios of $TBA^+:H^+$ in the colloidal solutions were determined as 16:1, 8:1, 4:1, 2:1, 1:1, 1:2, 1:4, 1:8, and 1:16 (Yuan et al., 2014). Here, the amount of H^+ denotes the molar ratio of the hydrogen atom that is replaced with potassium ions in the protonation procedure of layered material.

2.3. Langmuir-Blodgett film deposition of 2D oxide nanosheets

2.3.1. Langmuir-Blodgett deposition technique
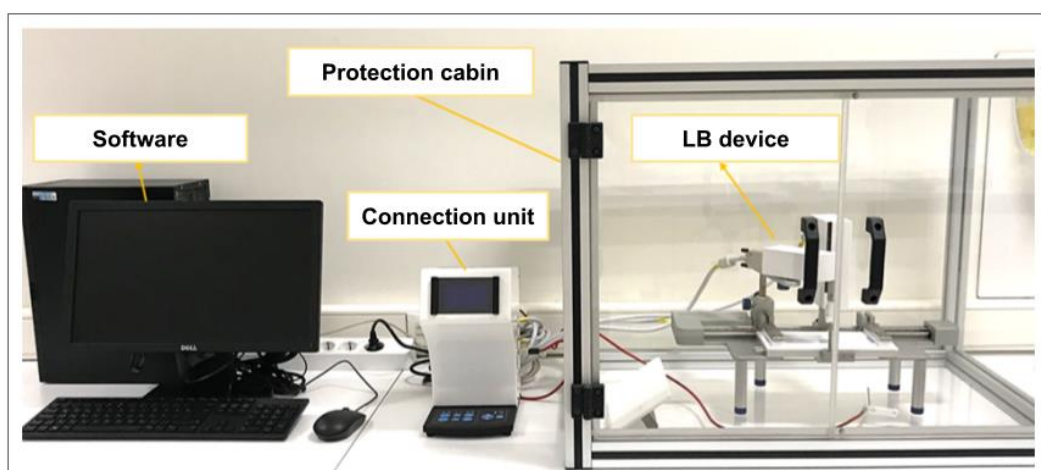
Figure 10. General view of LB system.

As shown in Figure 10, the LB system comprises a surface pressure sensor, dipping mechanism, barriers, temperature probe, Wilhelmy probe, and a connection unit. The protection cabin is also present to ensure that environmental conditions do not affect the coating. The coating parameters are determined using software specific to the LB system.
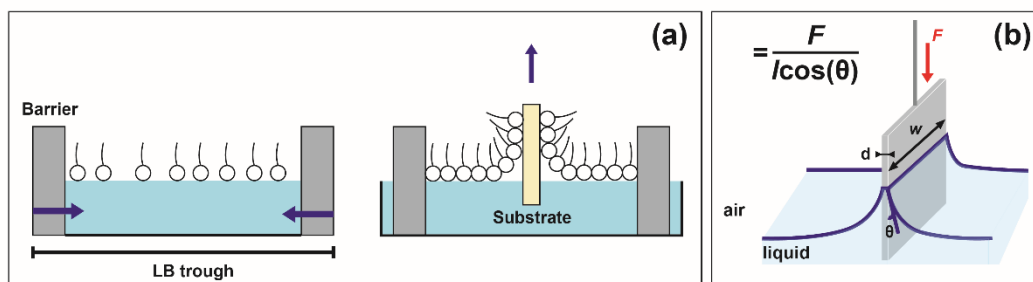
Figure 11. (a) Schematic illustration of LB deposition technique, (b) Wilhelmy plate.

As seen in Figure 11 (a), the LB device consists of two main parts. The first part is a trough with a deep groove, designed for the transfer of nanosheet-containing solutions and the dipping of the substrates. In the second part, there are barriers moving at a predetermined speed for compressing the nanosheets. The substrates used in this thesis, such as Si, ITO-PET, ITO-glass, titanium/golden coated glass (Ti/Au-glass), and titanium/golden coated Si (Ti/Au-Si), have hydrophobic surfaces. This characteristic allows nanosheets to be coated onto these substrates by moving them upward from the air-liquid interface at a specific speed as shown in Figure 11 (a). Before depositing nanosheets on the substrates, these substrates were washed in an ultrasonic bath with acetone (CH_3COCH_3 - Sigma Aldrich $\geq$ 99.9%), ethanol (CH_3CH_2OH – ISOLAB $\geq$ 99.9%), and isopropanol ($CH_3CH(OH)CH_3$ – Merck $\geq$ 99.8%). The Wilhelmy plate, which measures the surface tension obtained as a result of compressing the nanosheets with barriers, and the Wilhelmy equation are provided in Figure 11 (b). In the equation, "l" represents the perimeter of the part of the plate remaining in the liquid. This perimeter is obtained by adding the thickness "d" and the length "w" of the Wilhelmy plate *(l = 2w + 2d).* The specified angle Ө is the contact angle between the liquid and the plate. However, when coating with the LB device, the contact angle rarely measured; either literature values are used, or it is assumed that there is complete wetting.

2.3.2. Nanofilm fabrication with Langmuir-Blodgett technique

Nanofilm deposition has been carried out on substrates including Si, ITO-PET, ITO-glass, Ti/Au-glass, and Ti/Au-Si using colloidal solutions of $Ca_2NaNb_4O_{13}$ single oxide nanosheets with LB deposition technique. In a study conducted by Yuan et al. (2016), nanosheets containing colloidal solutions were diluted to obtain 500 mL of LB solution, and then 50 mL of this LB solution was transferred to the LB trough for nanofilm deposition. However, it was found that nanofilms could not be deposited with this method, and the studies continued with the optimized version of the LB method.
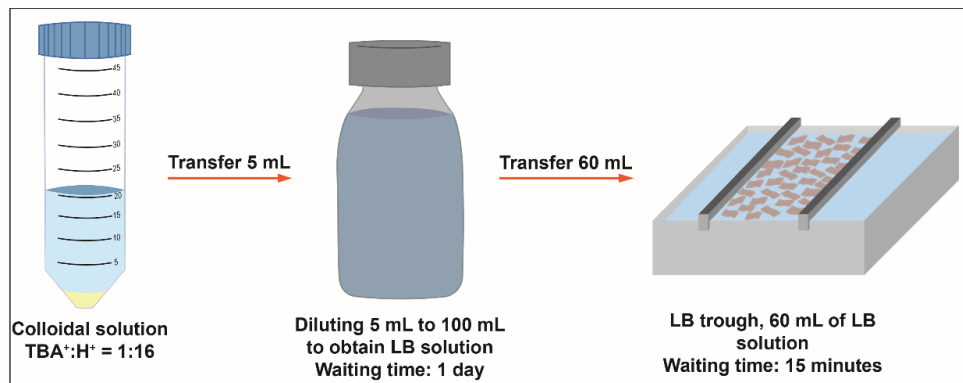
Figure 12. Schematic illustration of LB deposition technique.

LB solutions were prepared by diluting colloidal solutions 20 times by volume, as shown in Figure 9, and these LB solutions were allowed to rest for 1 day. Then, 60 mL of the LB solution was transferred to the LB trough, and it was left for 15 minutes to ensure the formation of an air-liquid interface and stabilize the surface tension before deposition. After each deposition, Si substrates were dried in an incubator at 110 °C for 20 minutes, followed by an hour of UV light exposure to degrade TBA^+ residues from the surface. On the other hand, ITO-PET substrates were dried at 60 °C for 20 minutes and then left under UV light for an hour. Also, the list of multilayer nanofilm containing ITO-PET samples were given in Table 3.

Table 3. List of nanofilm deposited ITO-PET samples with LB deposition technique

Nanosheets	Number of Nanofilm Layers	Sample
$Ca_2NaNb_4O_{13}$	10	ITO-PET/Sample 1
$Ca_2NaNb_4O_{13}$	10	ITO-PET/Sample 2
$Ca_2NaNb_4O_{13}$	10	ITO-PET/Sample 3
$Ca_2NaNb_4O_{13}$	10	ITO-PET/Sample 4
$Ca_2NaNb_4O_{13}$	15	ITO-PET/Sample 5
$Ca_2NaNb_4O_{13}$	20	ITO-PET/Sample 6

2.3.3. Physicochemical characterization of 2D oxide nanosheets on Si and ITO-PET substrates

The roughness analysis of both nanofilms and uncoated substrates were taken across 20 x 20 μm scanned area according to the previously described procedure (Przykaza et al., 2019; Szafran et al., 2022). The wettability characteristics of both uncoated Si and ITO-PET substrates, along with nanofilm coated substrates, were analysed by measuring the contact angles of two different liquids – ultra-pure water and diiodomethane (CH_2I_2, abcr Gmbh 99% purity). The sessile drop method was applied using optical tensiometer device. The contact angles were calculated by the tensiometer's software, which fits the profile of each liquids droplet on the surfaces. A volume of 5 µL for ultra-pure water and 2 µL for diiodomethane was dropped based on a case study conducted by Biolin Scientific with the Theta optical tensiometer (link ref). Each contact angle measurement was replicated twice on two samples of each substrate, all under room temperature and ambient humidity conditions.

Surface tension, represented by the γ, is universally recognized as being proportional to the intermolecular energy. This energy results from the combination of polar components and apolar components. The contact angle, denoted as Θ, correlates with the polar aspect of the surface tension, influenced by dipole interactions such as dipole moments and hydrogen bonds. Additionally, it relates to the apolar component of the surface tension, which is due to dispersion energy. This relationship is described by the harmonic mean (HM) model, a concept based on the thermodynamics (Wu,

1971). Integrating the HM model with Young's equation, a specific mathematical relationship is acquired:

$$(1 + \cos\theta)\,\gamma_L = 4\left(\frac{\gamma_L^p \gamma_S^p}{\gamma_L^p + \gamma_S^p} + \frac{\gamma_L^d \gamma_S^d}{\gamma_L^d + \gamma_S^d}\right) \quad (1)$$

γ^p_L *and* γ^d_L represent the polar and apolar (dispersive) components of the surface tension for the probing liquid (L), while γ^p_S and γ^d_S correspond to the polar and apolar components of the surface tension for the substrate (S). It is important to note that the total surface tension of the liquid (γ_L) is the sum of its polar and apolar components ($\gamma^p_L + \gamma^d_L$), as is the case for the substrates ($\gamma_S = \gamma^p_S + \gamma^d_S$). The calculation of the polar and apolar components of surface tension for both bare Si and ITO-PET substrates, as well as for $Ca_2NaNb_4O_{13}$ nanosheets-structured LB nanofilms on these substrates, was conducted by applying Equation 1, using contact angle measurements of ultra-pure water and diiodomethane. Specifically, the values for γ^p_L *and* γ^d_L were 51 and 21.8 mJ/m^2 for ultra-pure water (van Oss, 2006), and 2.3 and 48.5 mJ/m^2 for diiodomethane (Park et al., 2011; Gordesli et al., 2012), respectively. The study also interprets the polar surface tension component (γ^p) as the Lewis acid-base component, including both electron-acceptor and electron-donor characteristics, in line with the van Oss model (van Oss, 2006), a widely recognized approach in the literature (Jurak et al., 2016; Ewa et al., 2017; Ewa et al., 2018; Jurak et al., 2019).

The adhesion of $Ca_2NaNb_4O_{13}$ nanosheets-structured LB nanofilms (referred to as S_1) to the surfaces of Si and ITO-PET substrates (referred to as S_2) was separately calculated using Equation 2 (in air) and Equation 3 (in water) to determine the work of adhesion (W_{adh}). The concept of W_{adh}, as explained by the Dupre equation, is linked to the surface and interfacial tensions and is defined as the energy required to detach a unit area of two contacting phases (Comyn, 2021):

$$W_{adh} = \gamma_{S_1} + \gamma_{S_2} - \gamma_{(S_1-S_2)} \quad (2)$$

$$W_{adh} = \gamma_{(S_1-L)} + \gamma_{(S_2-L)} - \gamma_{(S_1-S_2)} \quad (3)$$

The components of interfacial tension as detailed in Equations 2 and 3 were determined using the HM model, as depicted below (Wu, 1971):

$$\gamma_{(S_1-S_2)}^P = \gamma_{S_1}^P + \gamma_{S_2}^P - 4\left[\frac{\gamma_{S_1}^P \; \gamma_{S_2}^P}{\gamma_{S_1}^P + \gamma_{S_2}^P}\right] \qquad (4)$$

$$\gamma_{(S_1-S_2)}^d = \gamma_{S_1}^d + \gamma_{S_2}^d - 4\left[\frac{\gamma_{S_1}^d \; \gamma_{S_2}^d}{\gamma_{S_1}^d + \gamma_{S_2}^d}\right] \qquad (5)$$

$$\gamma_{(S_1-S_2)} = \gamma_{(S_1-S_2)}^P + \gamma_{(S_1-S_2)}^d \qquad (6)$$

The interfacial tensions, specified in Equation 3, were calculated by incorporating the surface tension components of S_1 and L, and S_2 and L into Equations 4-6. Furthermore, the calculations of W^P_{adh} and W^d_{adh} were based on the polar and apolar surface and interfacial tension components, according to Equations 2 and 3, respectively.

To verify the results of the mathematical modelling and contact angle measurements of $Ca_2NaNb_4O_{13}$ nanosheets-structures nanofilms on Si and ITO-PET substrates, the exfoliation and dispersion of $HCa_2NaNb_4O_{13}$ in various concentrations of aqueous TBAOH solutions were studied. A range of aqueous TBAOH solutions with varying concentrations (0.001 to 10 wt%) were prepared, each with specific surface tensions between 32 and 68 mJ/m^2, a concentration span is known to typically promote hydrate formation (Nashed et al., 2016). Additionally, the dispersion of $HCa_2NaNb_4O_{13}$ dispersion in ultra-pure water was examined, with the surface tension of water considered to be 72 mJ/m^2. For each solution, as previously discussed in the exfoliation procedure of 2D oxide nanosheets, 0.1 g of protonated powder and TBAOH at different concentrations were mixed in 20 mL of ultra-pure water. These mixtures were then mechanically shaken at 130 rpm on an orbital shaker for 4 days and left to stand at room temperature for 3 days before UV/Vis absorption analysis. The absorbance of each suspension was measured at 272 nm, correlating with the surface tensions of the varied TBAOH solutions. The $Ca_2NaNb_4O_{13}$ nanosheets exhibited significant UV light absorption below 330 nm, particularly at 272 nm, due to their large band gap (Ebina et al., 2012; Kim et al., 2016). The peak absorbance was utilized

to determine the total surface tension of the $Ca_2NaNb_4O_{13}$ nanosheets. These procedures were repeated three times for consistency.

2.4. Patterning of LB Nanofilms with Electron Beam Lithography and Optic Lithography

The specified EBL method was applied on substrates such as Si, ITO-PET, Ti/Au-glass, Ti/Au-Si, and ITO-glass. Initially, ITO-PET/ Sample 1 was patterned with EBL method. Using the "Layout Editor" application, square shaped patterns with areas of 10 x 10 nm, 20 x 20 nm, 50 x 50 nm, 100 x 100 nm, and 200 x 200 nm applied onto ITO-PET/ Sample 1. Before the EBL process, the sample underwent various procedures. ITO-PET/Sample 1 was fixed to spin-coating chuck using a vacuum prior to patterning with EBL. Subsequently, the ITO-PET/Sample 1 was coated with polymethylmethacrylate A4 (PMMA A4) using a spin coating device at 4000 rpm for 40 seconds. After that, the sample was dried using a hot plate at 180 °C for 3 minutes. Then, the sample was dried with nitrogen gas and left to cool for 2 minutes. However, on the next attempt, due to the deformation of ITO-PET substrate at 180 °C, as shown in Figure 13, it was attached to the chuck using double-sided tape and then vacuum-sealed.
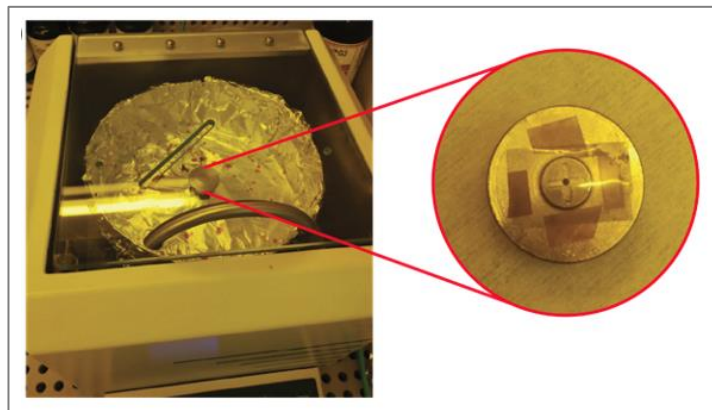
Figure 13. Spin-coating device and fixed ITO-PET sample on the chuck with double-sided tape.

ITO-PET/Sample 1 fixed onto the chuck was first coated with the conductive polymer, aquaSave, using a spin-coating device, and was subsequently coated with

PMMA A4. After undergoing these procedures, EBL application was conducted for ITO-PET/Sample 1. EDL conditions were 30 kV and 125.87 pA. However, patterns were not fabricated in the dose tests conducted under these conditions. As a result, the optical lithography technique was adopted for ITO-PET samples. The ITO-PET samples were patterned using optical lithography and deposited with ITO to create electrodes of various sizes. In comparison, Si, Ti/Au-glass, Ti/Au-Si, and ITO-glass substrates, being more rigid and not flexible as ITO-PET substrates, were patterned with EBL technique and coated with Ti/Au.

2.4.1. Patterning of LB films on Si, Ti/Au, ITO-glass substrates with EBL technique

Si, Ti/Au-glass, Ti/Au-Si, and ITO-glass substrates were coated with PMMA A4 and PMMA A2 using the spin-coating device at 4000 rpm for 40 seconds. Then, the substrates were heated on a hot plate at 180 °C for 3 minutes, dried with nitrogen gas, and left to cool for 2 minutes. EBL application on Si and ITO-glass substrates was performed with a 30 kV electron high tension (EHT), a beam current of 147 pA, and an aperture size of 30 μm to create square patterns with dimensions ranging from 20 μm, 10 μm, 5 μm, 1 μm, 500 nm, 300 nm, 250 nm, 100 nm, to 50 nm. The dose test range was between 100-1300 $\mu C/cm^2$. After the EBL process, the resist was stripped using acetone, and Ti/Au deposition was applied with a thickness of 15/20 nm. Similarly, the EBL technique was applied using the parameters shown in Table 4 for Si and ITO-glass substrates, but with the dose test range between 100-600 $\mu C/cm^2$.

Table 4. EBL parameters

Resist	Speed	Ramp	Time
PMMA A2	4000 rpm	1000 rpm/sec.	40 sec.
EHT	**Aperture Size**	**Beam Current**	**Dose Test**
30 kV	30 μm	147 pA	100-1300 $\mu C/cm^2$ for Si and ITO-glass substrates
			100-600 $\mu C/cm^2$

			for Ti/Au-glass and Ti/Au-Si substrates

2.4.2. Patterning of LB films on ITO-PET substrates with optic lithography technique and deposition of ITO electrodes

For ITO-PET substrates, optical lithography technique was employed as an alternative to EBL method (See in Figure 14). The process involved the following steps: ITO-PET/Sample 2 was vacuumed onto the chuck of the spin-coating device. Then, it was coated with AZ5214E negative photoresist at a speed of 4000 rpm for 40 seconds. After coating, the solvent-coated substrate was dried using a hot plate at 110 °C for 60 seconds, and gently vacuumed to the lithography device. The photomask contains square patterns of 5 different sizes, which are 75 µm, 100 µm, 150 µm, 200 µm, and 250 µm. The mask aligner of the device has a power of 3.5 mW/cm^2. The initial light exposure lasted 31 seconds. The substrate was then heated once more at 110 °C for 120 seconds, followed by exposure to UV light for 62 seconds. Wet stripping was performed for 27 seconds using a 1:4 mixture of AZ400K and deionized water. Finally, the resist was removed with acetone.
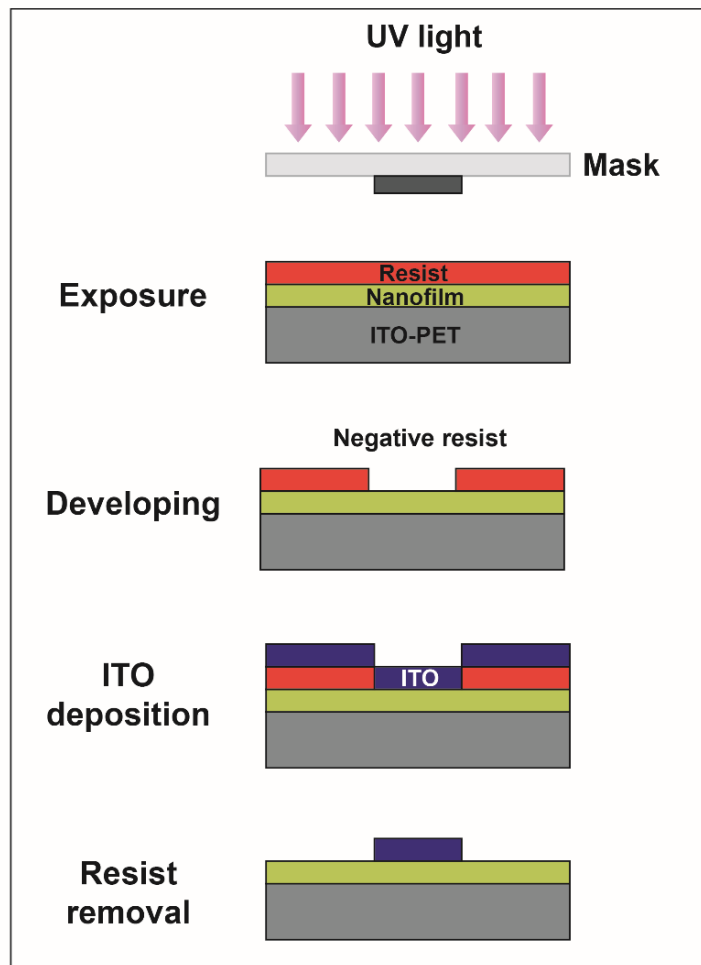
Figure 14. Schematic illustration of optic lithography technique with negative resist.

ITO deposition was applied on the patterns created by optical lithography using magnetic sputtering method. The magnetic sputtering device is shown in Figure 15 (a). The thickness of the ITO deposited on the patterns was determined as 75 nm, resulting in electrodes of various sizes. Then, the negative resist was removed with acetone from the ITO-PET sample.

Figure 15. (a) Magnetic sputtering device (Leybold, UNIVEX 350), (b) ITO target, (c) optic lithography applied ITO-PET/Sample 1 fixed on Si with thermal tape.

2.5. Structural, Mechanical, Electrical, and Optical Characterization of Ultra-Thin Capacitors

2.5.1. Optical analyses of LB nanofilms
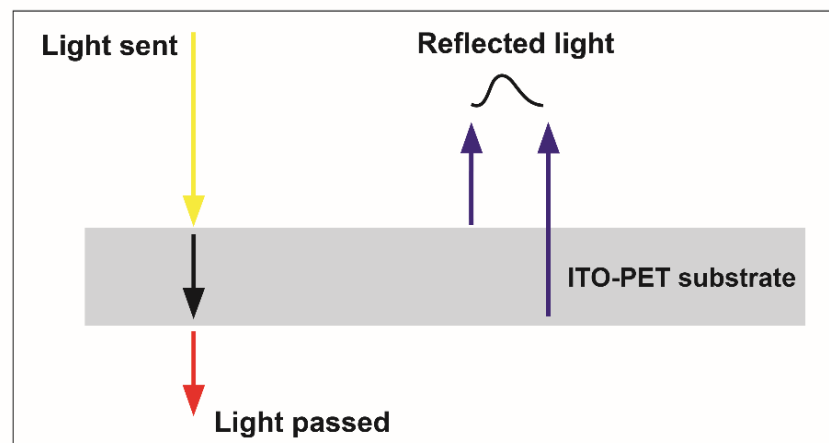
Figure 16. Schematic illustration of spectral reflectance analysis.

Spectral reflectance measurements were carried out using Filmetrics device to analyse the thickness and refractive indices of monolayer and ten-layer nanofilms. This device operates similar to ellipsometry device but, as shown in Figure 16, the angle incident light is always fixed at 90°. Therefore, this analysis only focused on reflectance values of nanofilms. As a result of the reflectance measurements, the percentage of reflectance of the nanofilms and the optical constants, n and k, were obtained.

2.5.2. Electrical analysis of capacitors fabricated in different sizes

Electrical analyses of ITO-PET substrates were conducted on ITO electrodes of five different sizes obtained by optical lithography technique on nanofilms with 10, 15, and 20 layers. The electrical analysis began with current (I)-voltage (V) measurements, subsequently followed by capacitance (C)-frequency (Hz) measurements on ITO electrodes.
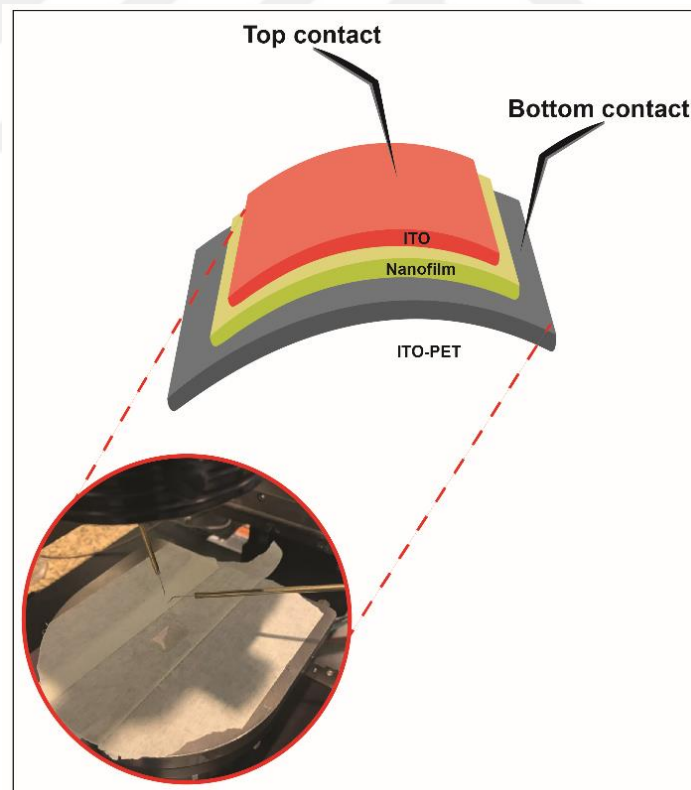
Figure 17. Schematic illustration of I-V measurements and application method on 10-layer nanofilm coated ITO-PET substrate.

I -V measurements were conducted on ITO electrodes of five different size on ITO-PET substrates. As shown in Figure 17, the bottom contact was taken from a 0.5 cm size uncoated section of ITO-PET substrate, while the top contact was applied on the ITO electrodes of various sizes. Leakage current values for the ITO electrodes on the ITO-PET substrates were obtained by dividing the current values from the I-V measurements by the electrode areas.

Similarly, like I-V measurements, frequency-dependent capacitance measurements were conducted on ITO electrodes on ITO-PET substrates. These capacitance measurements were within the 1 kHz to 1 MHz frequency range and were specifically carried out on 10-layer ITO-PET/Sample 4, 15-layer ITO-PET/Sample 5, and 20-layer ITO-PET/Sample 6.

The dielectric constant was calculated for the 10-layer ITO-PET/Sample 4, 15-layer ITO-PET/Sample 5, and 20-layer ITO-PET/Sample 6, measuring film thickness of each layer using atomic force microscopy (AFM).

Table 5. Measured film thicknesses of ITO-PET samples

Sample	Film Thickness
10-layer ITO-PET/Sample 4	41.309 nm
15-layer ITO-PET/Sample 5	65.140 nm
20-layer ITO-PET/Sample 6	76.380 nm

The impact of frequency-dependent capacitance on the dielectric on the dielectric constant for each electrode, across five different sizes, was calculated using the Equation 7:

$$\varepsilon_r = \frac{C.d}{S.\varepsilon_0} \qquad (7)$$

In the formula, C (F) represents the frequency-dependent capacitance, d (m) denotes the film thickness of the dielectric layers, S (m^2) stands for the area of the electrode, and ε_0 (F/m^2) denotes the permittivity of the vacuum. The permittivity constant ε_0 has a fixed value of 8.854×10^{-12} F/m^2.

2.5.3. Bending strengths of capacitors patterned in different sizes

The bending strength measurements were conducted by compressing the flexible ITO-PET substrates in the same direction and with the same magnitude five times to determine the changes in the frequency-dependent capacitance values.

2.6. Biofilm formation on Monolayer Nanofilm Deposited Si and ITO-PET Substrates

2.6.1. Bacterial growth conditions and preparation of Si and ITO-PET substrates

E. coli (ATCC 25404) bacterial strain was studied. The stock cultures containing this strain were diluted to 2% (v/v) and then added to Luria broth. The cultures were incubated for 12 to 16 hours at 30 °C on an orbital shaker at 170 rpm (Moreira et al., 2017). Following the overnight activation, the culture was further diluted to 1% (v/v) in fresh media. Bare Si and ITO-PET substrates, as well as monolayer nanofilm-deposited Si and ITO-PET substrates were placed inside a 12-well plate. The freshly prepared cultures were then added to the wells, and the plates were left to incubate at 37 °C in a static incubator for 48 hours. After 48 hours of incubation, the growth analysis of bacterial cells was conducted using UV/Vis absorption spectra at a wavelength of 600 nm.

Si and ITO-PET substrates were prepared in 1 x 1 cm^2 dimensions. Si substrates were cleaned using a piranha solution (H_2SO_4:H_2O_2) in a 3:1 (v/v) ratio to remove organic molecules from the surfaces of the substrates, followed by rinsing with isopropanol and ultra-pure water. In contrast, ITO-PET substrates were washed with acetone, ethanol, and ultra-pure water, each in an ultrasonication bath for 10 minutes. Both of the substrates, as well as those with monolayer nanofilm-deposited Si and ITO-PET substrates, were exposed to UV light before being placed inside the well-plates.

2.6.2. Crystal violet assay
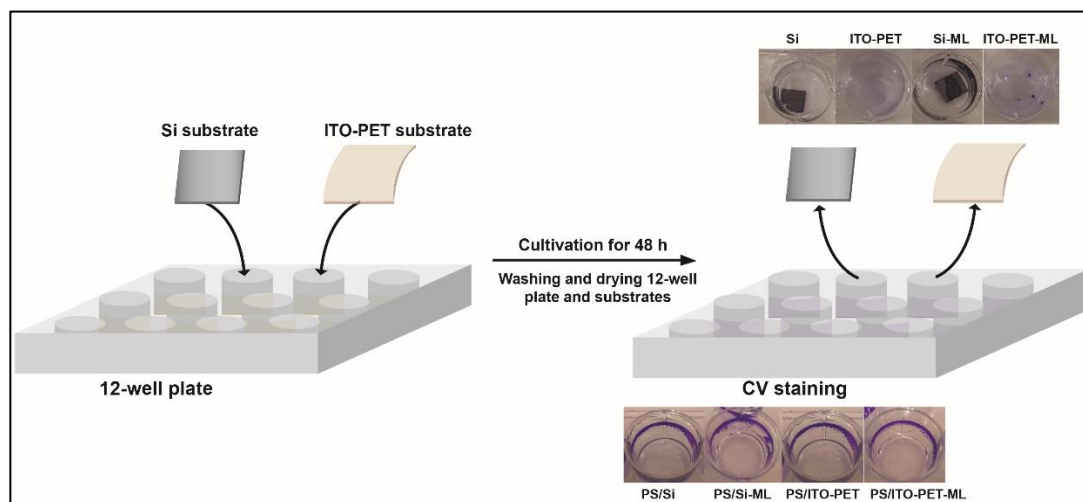
Figure 18. Schematic illustration of crystal violet assay.

To quantitatively analyze biofilm formation, crystal violet (CV) assay was performed using the *biofilm staining procedure* as shown in Figure 18. Before staining, both the substrates and 12 well-plates were washed three times with ultra-pure water to remove cells not contributing to biofilm formation. After drying the well plates, a 0.1% (v/v) CV solution was applied and left to stand for 10 minutes for staining. The CV then removed by washing both the substrates and well-plates three times with ultra-pure water, followed by drying. Each well and the substrates were then photographed. To each well containing polystyrene (PS) and the substrates, 4.5 mL of 95% (v/v) ethanol was added and left until the CV dissolved. The samples were subsequently analyzed again using the UV/Vis spectroscopy at a wavelength of 595 nm.

2.7. Characterization

The crystalline structure of the layered perovskites was analysed using X-ray powder diffraction (XRD) with Cu Kα radiation (1.5406 Å) using Philips X' Pert Pro apparatus. The surface morphology of the layered materials was examined using SEM (Carl Zeiss 300VP). UV/Vis absorption analysis on colloidal solutions with varying TBA^+:H^+ molar ratios was conducted with Perkin Elmer Lambda 750 spectrophotometer, operating in absorption mode for nanosheet characterization.

Transmittance analysis for nanofilms on both ITO-PET and ITO-glass substrates was performed using the same UV/Vis spectrophotometer, with repeating the analysis after each nanofilm deposition. The AFM (Hitachi 5100 N) was used to determine the thickness and lateral sizes of nanosheets, as well as for the nanofilm characterization on Si and Ti/Au substrates. Additionally, AFM was employed to calculate the arithmetic mean roughness (S_a) and the root mean square roughness (S_q) of nanofilms on Si and ITO-PET substrates, also conducted on uncoated Si and ITO-PET substrates. c-AFM were also used for I-V measurements of the nanoscale capacitors fabricated on Ti/Au-Si, Ti/Au-glass, and ITO-glass substrates. The contact angle measurements on nanofilms, and uncoated Si and ITO-PET substrates were conducted using Theta optical tensiometer (Biolin Scientific/ Attension). The EBL system (e-line Plus Raith) was applied on Si, Ti/Au, and ITO-glass substrates, while the ITO-PET substrates were patterned using an optical lithography system (MA6 Mask Aligner) due to their flexible structure. The ITO deposition on patterns was conducted using magnetic sputtering device, UNIVEX 350 (Leybold), to create electrodes on ITO-PET substrates. The frequency-dependent capacitance values of the resulting electrodes were measured using Keithley 2612B system Sourcemeter, and the I-V measurements were measured with Flanium device. The characterization of patterns was visualized using an optical microscope (Nikon) and SEM (Raith e-Line). Reflectance analyses of the ITO-PET substrates were conducted using Filmetrics device. X-ray photoelectron spectroscopy (XPS) analysis of nanofilm-deposited ITO-PET substrates were conducted using Thermo Scientific K-Alpha Photoelectron Spectrometer.

CHAPTER 3: RESULTS AND DISCUSSION

3.1. Structural Analysis of Layered Perovskites
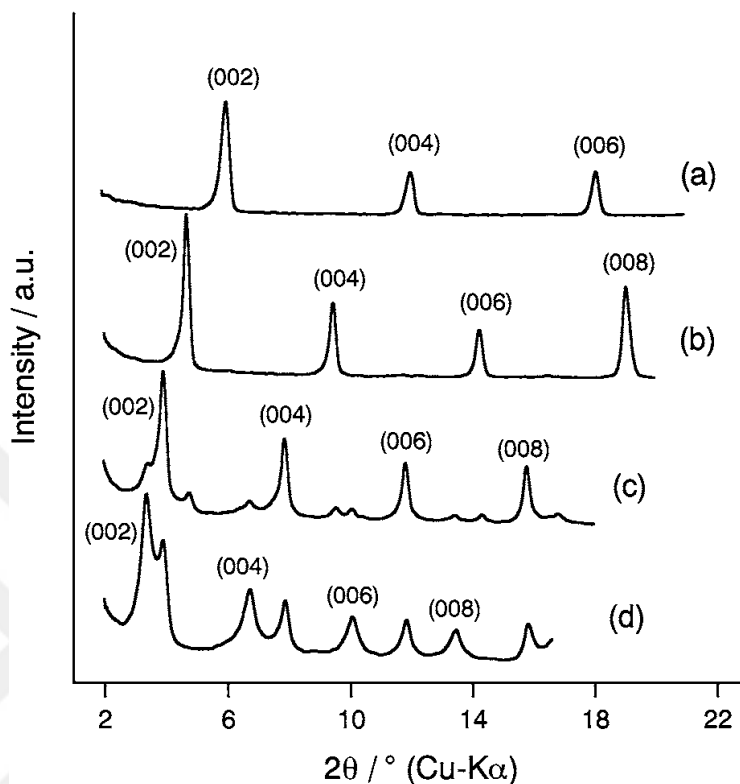
Figure 19. XRD patterns of K[Ca$_2$Na$_{n-3}$Nb$_n$O$_{3n+1}$], (a) n = 3, (b) n = 4, (c) n = 5, (d) n = 6 (Shangguan and Yoshida, 2001).

Shangguan and Yoshida (2001) initially synthesized the KCa$_2$NaNb$_4$O$_{13}$ layered material by separately synthesizing KCa$_2$Nb$_3$O$_{10}$ and NaNbO$_3$. These two materials were then mixed and annealed again in muffle furnace. The resulting XRD patterns of the K[Ca$_2$Na$_{n-3}$Nb$_n$O$_{3n+1}$] layered materials, with varying values of n, are depicted in Figure 19. According to these XRD patterns, pure phases of compounds with n = 3, 4 were successfully synthesized, while combinations with n > 4 showed the presence of other members of series. For example, a small phase of n = 4, 6 was detected in the n=5 compound, and a minor phase of n = 5 was observed in the n = 6 compound. The peak in the (002) miller index shifted to lower 2Θ value as n increased, indicating that the thickness of the perovskite layers was consistent with the addition of NaNbO$_3$.
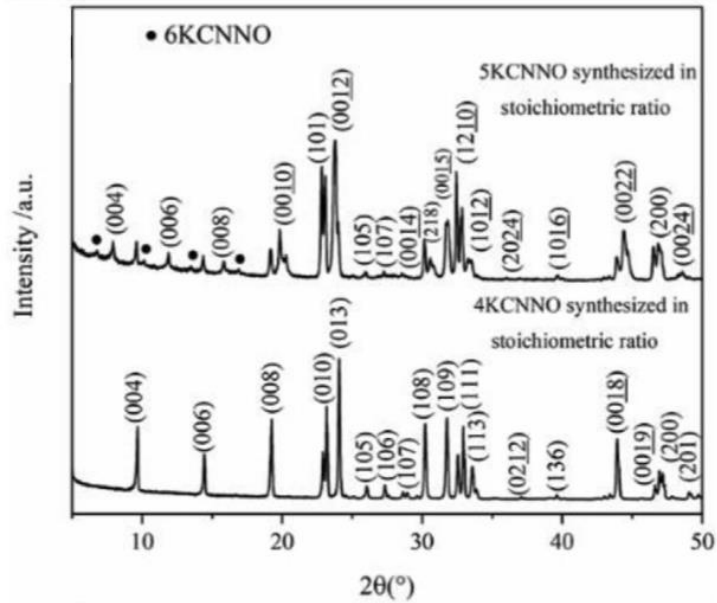
Figure 20. XRD patterns of (a) 4KCNNO ($KCa_2NaNb_4O_{13}$), 5KCNNO ($KCa_2Na_2Nb_5O_{16}$), and 6KCNNO ($KCa_2Na_3Nb_6O_{19}$), synthesized in stoichiometric proportions at a heating rate of 5 °C/ min between 1200 – 1300 °C (Source: Liu et al., 2020).

According to Liu et al. (2020), a single – step synthesis annealing approach was conducted at a heating rate of 5 °C/ min between 1200 – 1300 °C, with stoichiometric proportions. The XRD patterns of $KCa_2NaNb_4O_{13}$, $KCa_2Na_2Nb_5O_{16}$, and $KCa_2Na_3Nb_6O_{19}$ layered materials were shown in Figure 20. It was found that increasing the molar ratio of volatile chemicals at high temperatures resulted in different compounds, such as $KCa_2Na_2Nb_5O_{16}$ and $KCa_2Na_3Nb_6O_{19}$, instead of expected $KCa_2NaNb_4O_{13}$ layered material. Similarly, under the synthesis condition (i) of using an excess of 50% molar K_2CO_3 and Na_2CO_3, unexpected peaks were observed in the XRD patterns of the expected $KCa_2NaNb_4O_{13}$ layered material, as shown in Figure 21 (a). As seen in Figure 20, these peaks overlapped with those of 5KCNNO and 6KCNNO, it was decided not to exceed the stoichiometric amount of volatile chemicals. Furthermore, Figure 21 shows different synthesis conditions of $KCa_2NaNb_4O_{13}$ layered material with a varying heating rate during the annealing processes.
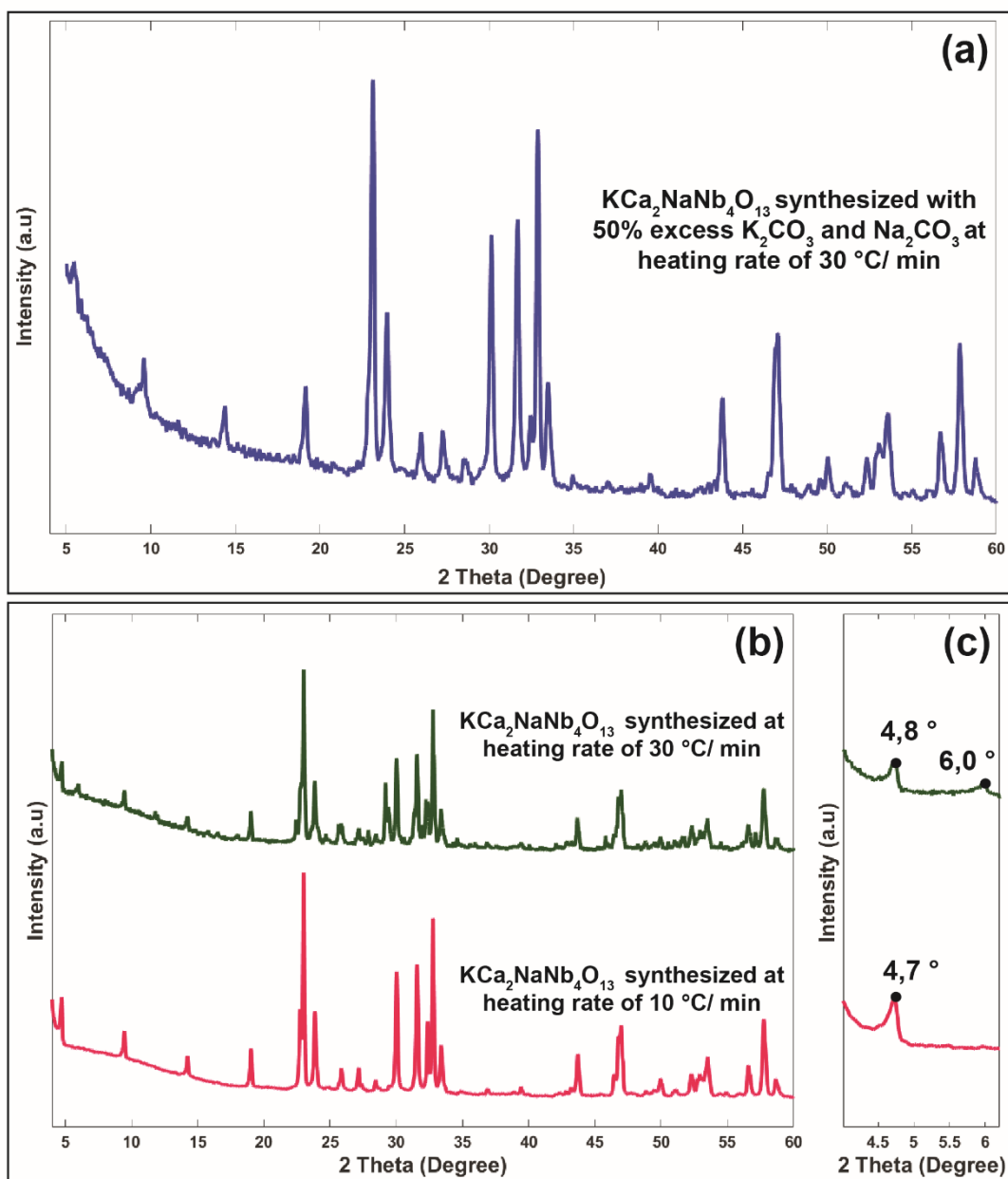
Figure 21. XRD patterns of KCa$_2$NaNb$_4$O$_{13}$ synthesized under (a) (i) condition at heating rate of 30 °C/ min, (b) (ii) condition at heating rate of 30 °C/ min, (iii) condition at heating rate of 10 °C/ min, (c) magnification of the 4 – 6 ° region.

XRD patterns of KCa$_2$NaNb$_4$O$_{13}$ layered material synthesized under conditions (ii) and (iii) are presented in Figure 21 (b). In Figure 21 (c) illustrates the extra peaks, alongside the Bragg peaks, formed in the KCa$_2$NaNb$_4$O$_{13}$ layered material synthesized under condition (ii). These additional peaks have been identified to correspond with the XRD patterns of the KCa$_2$Na$_2$Nb$_5$O$_{16}$ and KCa$_2$Na$_3$Nb$_6$O$_{19}$ layered materials (See in Figure 21). Thus, the XRD patterns of the KCa$_2$NaNb$_4$O$_{13}$ layered material

synthesized at a heating rate of 10 °C/ min under condition (iii) were determined to be consistent with the literature considering (002), (004), (006), and (008) Bragg peaks. Consequently, the material synthesized under condition (iii) was selected for the protonation process.
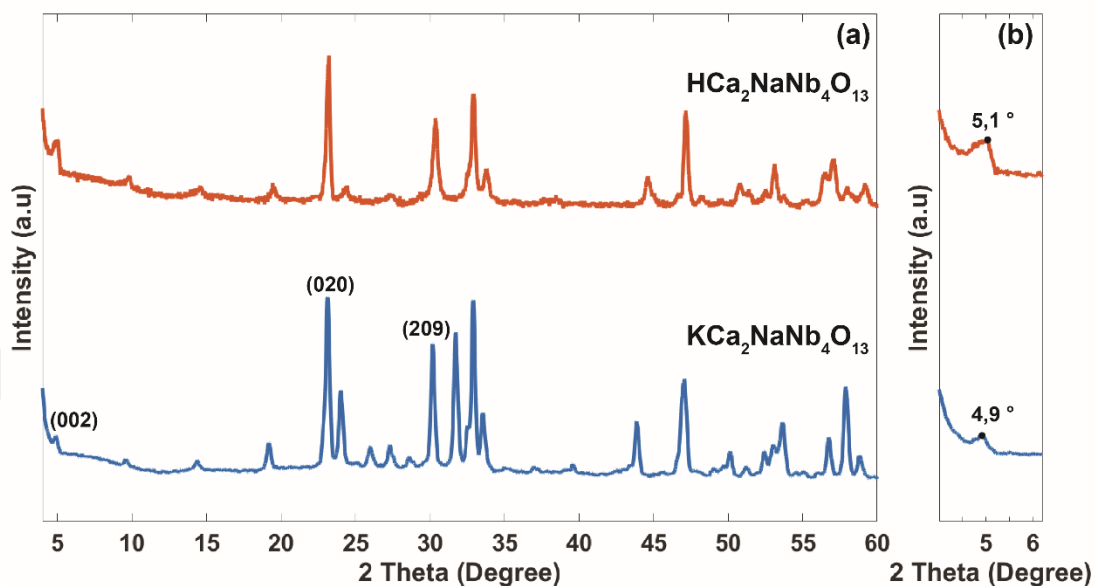
Figure 22. XRD patterns of $KCa_2NaNb_4O_{13}$ and $HCa_2NaNb_4O_{13}$ synthesized under (a) (iii) condition at heating rate of 10 °C/ min, (b) magnification of the $4.5 - 6$ ° region.

The XRD patterns for both layered $KCa_2NaNb_4O_{13}$ and its protonated form, $HCa_2NaNb_4O_{13}$, synthesized under synthesis condition (iii), are illustrated in Figure 22. The lattice parameters for the $KCa_2NaNb_4O_{13}$ layered material, determined to be a = 0.8304 nm (209), b = 0.7684 nm (020), and c = 3.598 nm (002) in the miller indices, correspond to an orthorhombic crystal structure, and these values align with the literature (Knyazev et al., 2019). The effect of protonation process on the layered material, marked by the replacement of K^+ ions with H^+ ions in the interlayer space, was verified by the shift in the (00l) peak to higher angles, as seen in Figure 22.
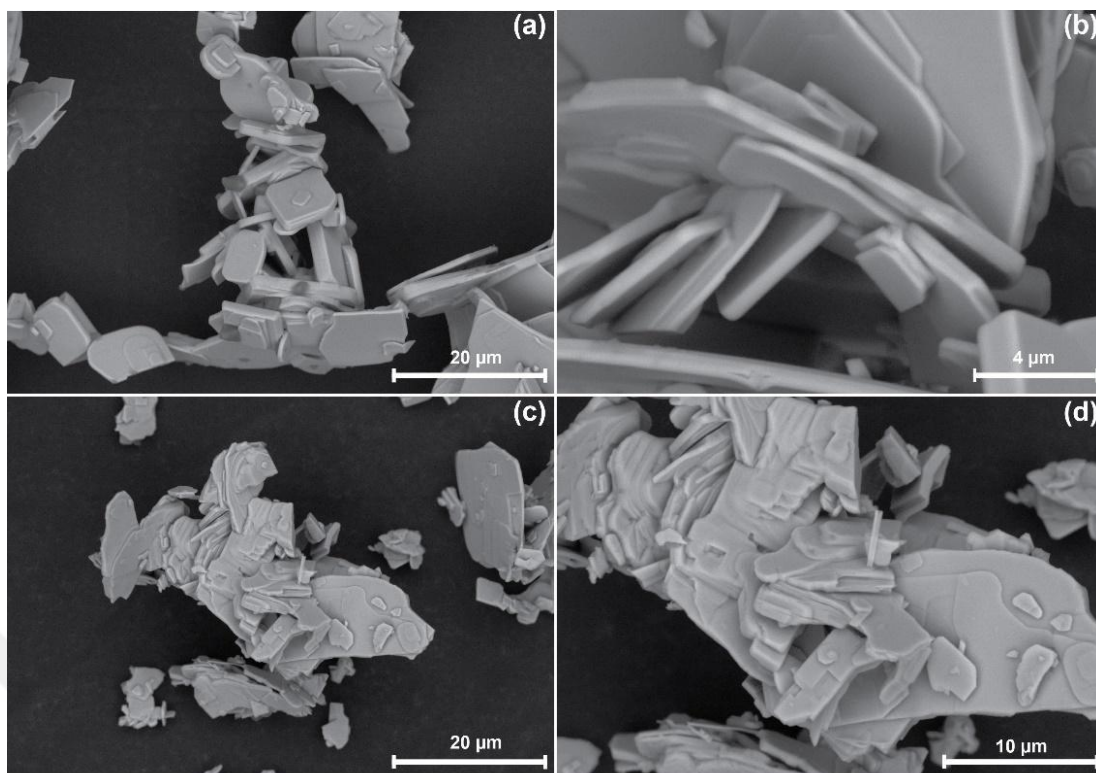
Figure 23. SEM images of (a), (b) $KCa_2NaNb_4O_{13}$ layered material, (c), (d) proton-exchanged layered $HCa_2NaNb_4O_{13}$ material.

In Figure 23 (a), the SEM image illustrating the layered structure, a product of the solid-state reaction, exhibits a uniform, plate – like morphology with dimensions ranging from 4 and 10 μm. As shown in the SEM image in Figure 23 (c), the lateral area of the layered $HCa_2NaNb_4O_{13}$ material appears unchanged, indicating that its plate-like morphological structure is preserved even after the protonation process and subsequent shaking.

Table 6. Energy dispersive X-ray (EDX) analysis of $KCa_2NaNb_4O_{13}$ layered material

Element	Line Type	Weight %	Weight % Sigma	Atomic %
O	K	33.64	0.40	65.90
Na	K	4.93	0.11	6.72
K	K	4.99	0.10	4.00
Ca	K	9.76	0.14	7.63
Nb	L	46.68	0.36	15.75
Total		100.00		100.00

In Table 6, which presents the EDX analysis of the $KCa_2NaNb_4O_{13}$ layered material, calculations were conducted with the minimum percentage value set to 1. Here, the element K has the lowest atomic percentage at 4.00. When considering K as 1 in the formulation, the atomic percentage of the Nb element is calculated to be approximately 4, determined by dividing its atomic percentage of 15.75 by the atomic percentage of K element. Based on this calculation, considering the K:Ca:Na:Nb to be 1:2:1:4, the ratios of the synthesized material have been determined to be 1:1.90:1.68:3.93.

Table 7. Theoretical and actual weights of $KCa_2NaNb_4O_{13}$ layered material

Element	Weight % by EDX	Theoretical Weight %
O	33.64	28.81
Na	4.93	3.18
K	4.99	5.42
Ca	9.76	11.10
Nb	46.68	51.48
Total	100.00	100.00

Therefore, as shown in Table 7, weight percentage obtained by EDX analysis of the elements are in good agreement with the theoretical weight percentages reported in the literature (Liu et al., 2020). It is important to know that EDX analysis is often performed under less controlled measurement conditions, especially considering the state of the sample and the position of the electron beam on morphologically complex surfaces. For this reason, the results of the EDX analysis have been interpreted as acceptable.

3.2. Synthesis and Characterization of 2D Oxide Nanosheets
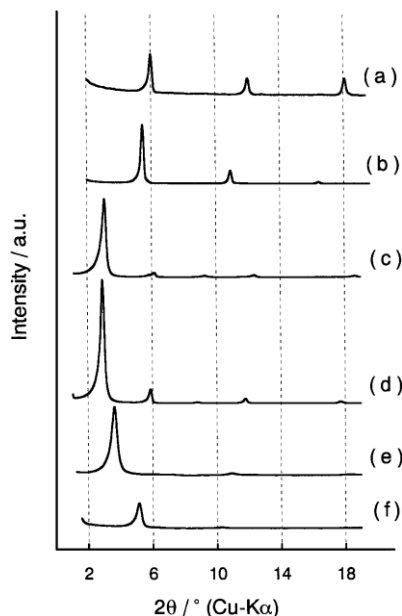
Figure 24. XRD pattern of (a) $KCa_2Nb_3O_{10}$ layered material, (b) protonation process of $KCa_2Nb_3O_{10}$ layered material with 6 M HNO_3 (Source: Shangguan and Yoshida, 2001).

According to literature and as illustrated in Figure 24 (a), the DJ-type $KCa_2Nb_3O_{10}$ layered material experiences leftward shift in the (00l) Bragg peaks after protonation process with 6 M HNO_3 [See in Figure 24 (b)]. Similarly, the $KCa_2NaNb_4O_{13}$ layered material also experiences a leftward shift in the (00l) Bragg peaks within its XRD patterns, indicating an expansion of the lattice structure along the c-axis (Shangguan and Yoshida, 2001). Based on these studies, the protonation of the $Ca_2NaNb_4O_{13}$ nanosheets was conducted by mixing 1 g of the powder in 40 mL of 5 M HNO_3 acid solution for 4 days on an orbital shaker to form $HCa_2NaNb_4O_{13}$ layered material.

Table 8. EDX analysis of $HCa_2NaNb_4O_{13}$ layered material

Element	Line Type	Weight %	Weight % Sigma	Atomic %
O	K	34.81	0.42	69.51
Na	K	2.67	0.10	3.71
K	K	0.36	0.07	0.29
Ca	K	11.29	0.15	9.00
Nb	L	50.87	0.39	17.49
Total		100.00		100.00

According to EDX analysis presented in Table 8, the calculated Ca:Na:Nb ratios were determined to be 2.42:1:4.71. This ratio aligns with the theoretical ratio of 2:1:4.

Moreover, the atomic weight percentage of K being less than 1 indicating the proton exchange has occurred.

Yuan et al. (2016) synthesized nanosheets in colloidal solutions by shaking them for 2 hours and also 7 days on an orbital shaker. Then, they allowed the colloidal solutions to settle for 20 hours before characterizing them on Si substrates. The AFM images obtained from this process are shown in Figure 25.
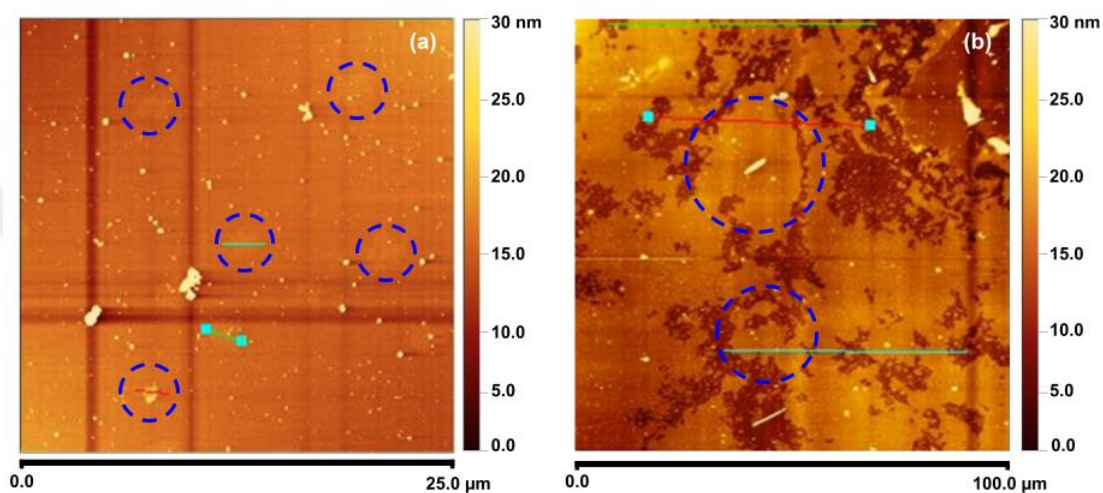
Figure 25. AFM images of colloidal solutions dropped on Si substrate with a TBA$^+$:H$^+$ ratio of 8:1 (a) shaken for 2 hours, (b) shaken for 7 days (dashed blue circles show TBA$^+$ residues).

TBA$^+$ residues were detected from the AFM images of colloidal solutions, consisting of a TBAOH and ultra – pure water mixture with an 8:1 TBA$^+$:H$^+$ ratio, shaken for 2 hours and 7 days, as indicated by dashed blue circles in Figure 25. These residues were approximately 10 nm thick. It was determined that these colloidal solutions, having the same TBA$^+$:H$^+$ ratio and shaking duration, did not result in nanosheet formation.

Further optimization of the exfoliation process, as highlighted in Sasaki and Watanabe (1998), showed that TBA$^+$:H$^+$ ratios below 0.3 prevent the creation of colloidal solutions with nanosheets, while ratios above 0.5 promote it. The optimal ratio for TBA$^+$:H$^+$ is likely between 0.3 and 0.5. The study also emphasized that TBA$^+$

concentration is crucial in the exfoliation process, with high TBA^+ ratios leading to excessive osmotic swelling and low ratios being favorable for nanosheet formation.
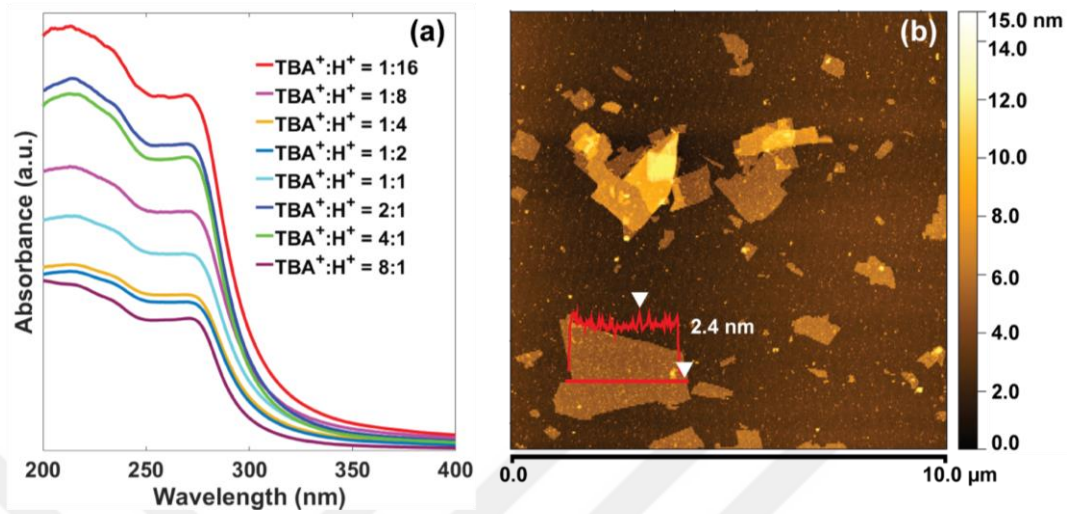
Figure 26. (a) UV/Vis absorption spectra of colloidal solutions containing $Ca_2NaNb_4O_{13}$ single nanosheets at different TBA^+:H^+ molar ratios, (b) AFM image of $Ca_2NaNb_4O_{13}$ single nanosheets on Si substrates.

The UV/Vis absorption spectra of colloidal solutions containing single $Ca_2NaNb_4O_{13}$ nanosheets, shaken for 4 days at 100 rpm at different TBA^+:H^+ molar ratios are presented in Figure 26 (a). The colloidal solution with the highest absorption was determined to have a TBA^+:H^+ molar ratio of 1:16, as demonstrated by its absorption peak at 272 nm in Figure 26 (a). These nanosheets, with an optical band gap of 3.92 eV, effectively absorb UV light and show reduced absorbance in the visible spectrum (Chang et al., 2022). Additionally, Figure 26 (a) shows that the absorption spectra do not increase linearly with the varying TBA^+:H^+ molar ratios.

In Figure 26 (b), single $Ca_2NaNb_4O_{13}$ nanosheets were detected in the AFM analysis by dropping the colloidal solution with TBA^+:H^+ molar ratio of 1:16 on Si substrate. The height profile given in the inset of the AFM image indicates the nanosheets are 2.4 nm thick with slightly thicker edges due to water molecule accumulation. Their lateral size was determined to be approximately 3.5 μm. The thicknesses and lateral sizes of these nanosheets are consistent with studies of quadruple octahedral unit layers (Li et al., 2017).

3.3. Fabrication and Characterization of Nanofilms

3.3.1. Nanofilm fabrication with 2D oxide nanosheets
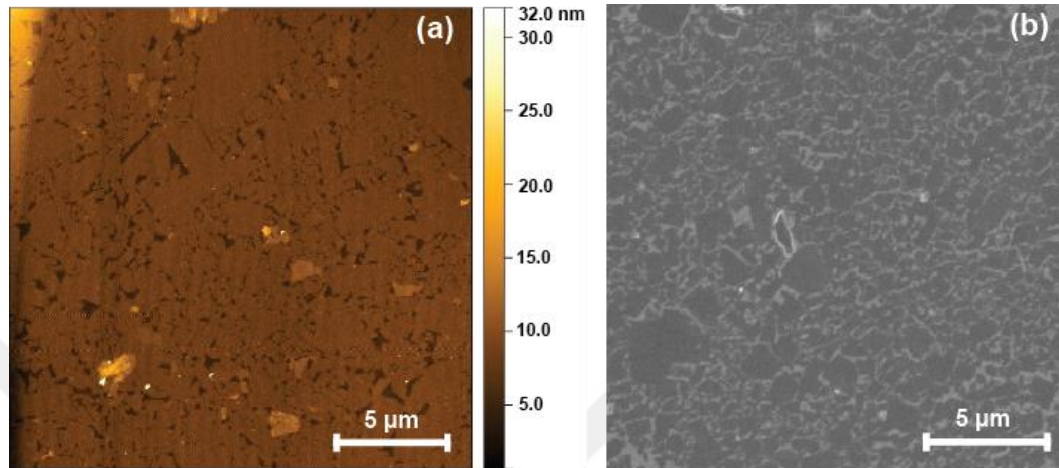
Figure 27. (a) AFM image of monolayer $Ca_2NaNb_4O_{13}$ nanofilm deposited by LB technique on Si substrate, (b) SEM image of monolayer $Ca_2NaNb_4O_{13}$ nanofilm deposited by LB technique on ITO-PET substrate.

The AFM image of a monolayer $Ca_2NaNb_4O_{13}$ nanofilm, deposited on a Si substrate by LB technique was given in Figure 27 (a). To determine the coverage percentage of the monolayer on Si substrates, an analysis of five distinct AFM images were analysed. As indicated in Figure 27 (a), LB deposition technique yielded a notably high coverage of $96.2 \pm 1.1\%$.

The ITO-PET substrate has a rough surface so that a clear detection of nanosheets and nanofilms via AFM was challenging. Therefore, SEM was employed for visualizing of ITO-PET substrates. The SEM image in Figure 27 (b) illustrates the effective deposition of $Ca_2NaNb_4O_{13}$ nanofilm using LB, resulting in a complete coverage of nanosheets over an area of about 20 μm.
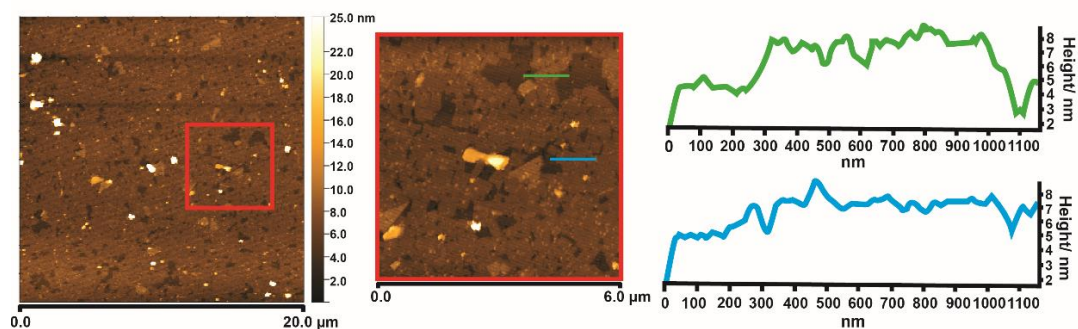
Figure 28. AFM image and height profiles of two-layer $Ca_2NaNb_4O_{13}$ nanofilms deposited by LB technique on Si substrate.

Figure 28 shows the successful deposition of two-layer $Ca_2NaNb_4O_{13}$ nanofilm on Si substrate by LB technique, as indicated by the height profiles. The thickness of the first layer of nanofilm is approximately 3 nm, the height difference between this layer and the second can be examined in the height profile scanned along the green line. In light of these findings, 10-layer deposition of $Ca_2NaNb_4O_{13}$ nanofilms on ITO-PET substrates was conducted by the LB technique with a drying process after each deposition. Noting that the drying process between deposition differs from that on Si substrates due to deformation of ITO-PET substrates with heat. Therefore, ITO-PET substrates were dried at 60 °C for 20 minutes, which is 110 °C for Si substrates. They were then left under UV light for an hour to remove any TBA^+ residues.
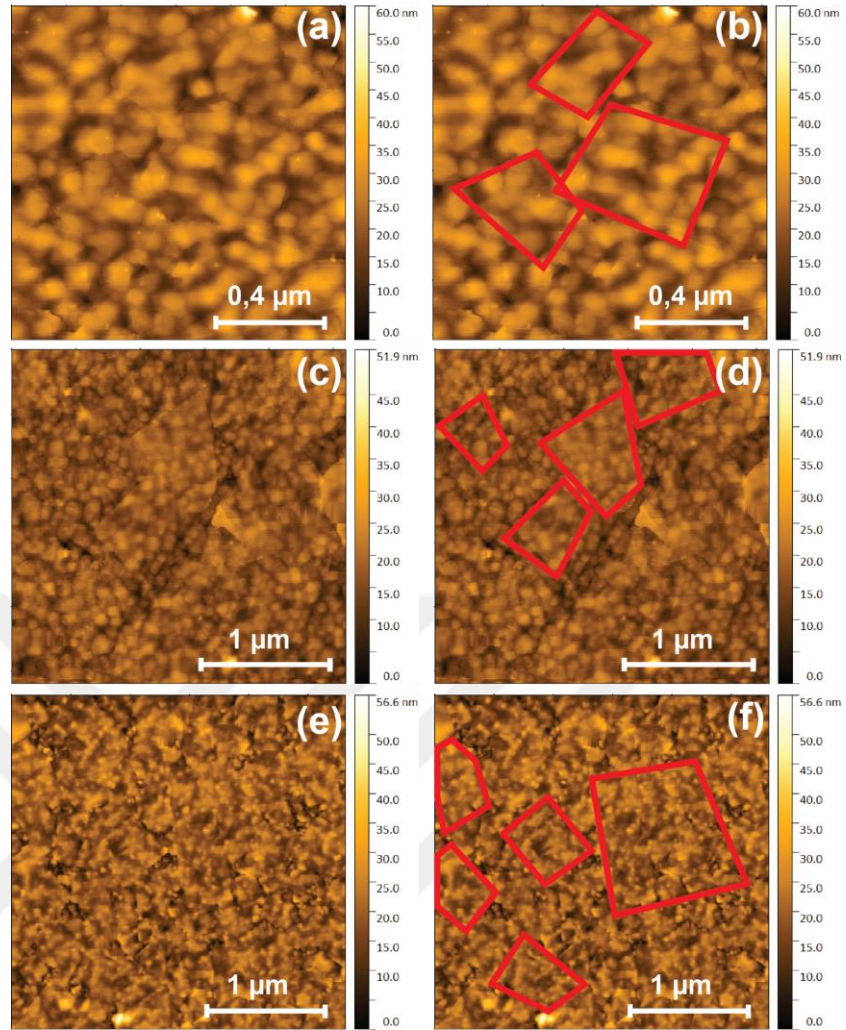
Figure 29. AFM images of two-layer $Ca_2NaNb_4O_{13}$ nanofilms on (a) Ti/Au-glass substrate (b) nanosheets marked on Ti/Au-glass substrate, (c) Ti/Au-Si, (d) nanosheets marked on Ti/Au-Si substrate, (e) ITO-glass substrate, and (d) nanosheets marked on ITO-glass.

The characterization of Ti/Au-glass, Ti/Au-Si, and ITO-glass substrates was conducted using AFM, which confirmed that there were no gaps between the nanosheets and that a complete deposition of two-layer $Ca_2NaNb_4O_{13}$ nanofilms on substrates was achieved. The AFM images of Ti/Au-glass, Ti/Au-Si, and ITO-glass substrates that contains these nanofilms were presented in Figure 29.
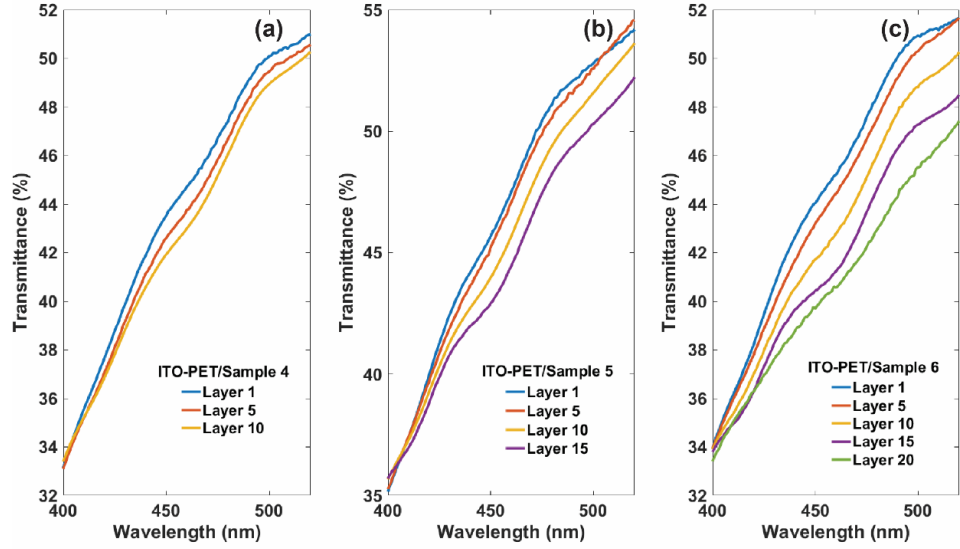
Figure 30. UV/Vis transmittance spectra of (a) 10-layer ITO-PET/Sample4, (b) 15-layer ITO-PET/Sample 5, (c) 20-layer ITO-PET/Sample 6.

Figure 30 shows the UV/Vis transmittance spectra for the 10-layer ITO-PET/Sample 4, the 15-layer ITO-PET/Sample 5, and the 20-layer ITO-PET/Sample 6. A decrease in the transmittance of the ITO-PET substrates was observed with an increasing number of nanofilm layers, corresponding to the thickness of these layers. Considering the $Ca_2NaNb_4O_{13}$ nanosheets are roughly 2.4 nm thick, the transmittance decrease between the 1st and 10th layers was about 2% [See in Figure 30 (a)]. In the case of ITO-PET/Sample 4, as depicted in Figure 30 (b), the transmittance decrease between the 1st and 15th layers was approximately 3% aligning well with the nanosheet thicknesses. For the 15-layer ITO-PET/Sample 6, the decrease in transmittance was about 5%, as shown in Figure 30 (c).

Therefore, the decrease in optical transmittance observed in the $Ca_2NaNb_4O_{13}$ nanofilms deposited on ITO-PET substrates is proportional to the increase in the number of nanofilm layers, indicating that the nanofilms successfully fabricated on ITO-PET substrates.
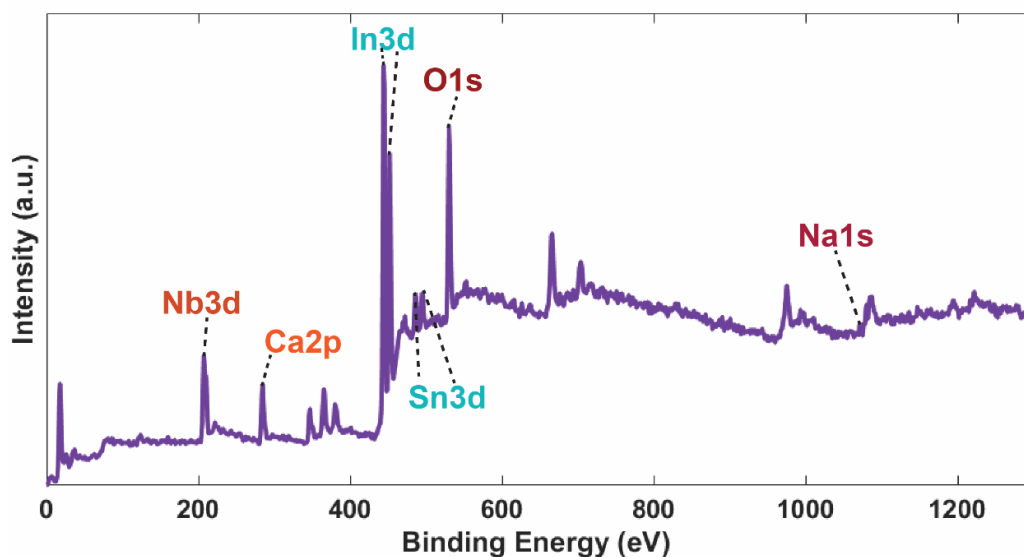
Figure 31. XPS survey spectra of Nb 3d, Ca 2p, O 1s, Na 1s, In 3d, and Sn 3d for nanofilm-deposited ITO-PET substrate.

To verify the LB nanofilm deposition on ITO-PET substrates, XPS analysis were performed. Figure 31 shows the XPS survey spectra of Nb 3d, Ca 2p, O 1s, Na 1s, In 3d, and Sn 3d for nanofilm-deposited ITO-PET substrates. Atomic % Na 1s was determined as 3.41, for Ca 2p as 8.51, and Nb 3d as 16.38, which correlates with the actual formula of $Ca_2NaNb_4O_{13}$ nanosheets when 3.41 percent was considered as 1. The ratio of Ca:Na:Nb becomes 2.5:1:4.8, similar to 2:1:4. According to the XPS survey of Nb 3d, Ca 2p, O 1s, Na 1s, In 3d, and Sn 3d for nanofilm-deposited ITO-PET substrate, the successful nanofilm deposition to these substrates were conducted using LB deposition technique. Furthermore narrow-scan XPS spectra of Nb 3d, Ca 2p, O 1s, Na 1s, In 3d, and Sn 3d was shown in Figure 32.
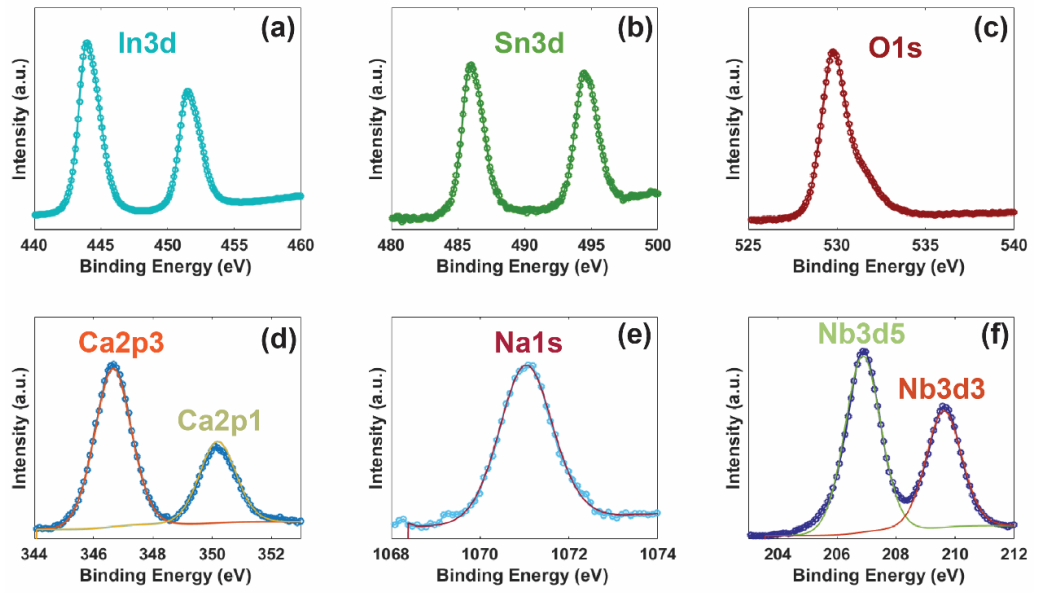
Figure 32. Narrow-scan XPS spectra of (a) In 3d, (b) Sn 3d, (c) O 1s, (d) Ca 2p, (e) Na 1s, and (f) Nb 3d.

The characteristic peaks of In 3d positioned at roughly at 444 and 451.5 eV, aligning with the previously determined values binding energy of O_2-cleaned ITO-PET substrates (Kerner et al., 2019; Hung et al., 2023) [See in Figure 32 (a)]. In Figure 32 (b), narrow-scan XPS results of Sn 3d shows the two characteristic peaks at 486 and 494.5 eV, respectively (Danq et al., 2015). The O 1s peak is observed at binding energy of 529.8 eV, is due to the oxygen in $Ca_2NaNb_4O_{13}$, indicating the presence of oxygen in the O^{2-} oxidation state (Ma et al., 2017), as shown in Figure 32 (c). The binding energies of Ca 2p is presented in Figure 32 (d), the peaks of Ca $2p_{3/2}$ located at 346.7 eV, and the peak for Ca $2p_{1/2}$ at 350.2 eV, aligning with the literature (Ding et al., 2014). Figure 32 (e) presents the characteristic peak of Na 1s, determined at binding energy of 1071 eV (Oswald, 2015). The narrow-scan XPS spectra of Nb 3d is shown in Figure 32 (f), displaying peaks at 206.9 eV and 209.6 eV for $Ca_2NaNb_4O_{13}$ nanosheets-structured nanofilm-deposited ITO-PET substrate, corresponding Nb $3d_{5/2}$ and Nb $3d_{3/2}$, respectively, indicating Nb atom in $Ca_2NaNb_4O_{13}$ nanosheets exists in the Nb^{5+} oxidation state (Atuchin et al., 2005).

3.3.2. Physicochemical characterization of 2D oxide nanosheets on Si and ITO-PET substrates

Table 9. Physicochemical characterization parameters of both bare and nanofilm deposited Si and ITO-PET substrates

	Si	Nanofilm on Si	ITO-PET	Nanofilm on ITO-PET
S_a *(nm)*	2.3 ± 1.4	0.8 ± 0.1	30.5 ± 2.4	16.6 ± 1.9
S_q *(nm)*	4.2 ± 0.9	2.0 ± 0.1	44.5 ± 5.7	25.3 ± 3.6
Θ_{water}	64.3 ± 1.4	30.0 ± 1.2	97.5 ± 0.8	31.5 ± 1.1
$\Theta_{diiodomethane}$	43.8 ± 1.0	38.6 ± 0.9	50.3 ± 2.9	32.8 ± 2.1
γ^p_s *(mJ/m^2)*	17.2	34.2	2.90	32.6
γ^d_s *(mJ/m^2)*	33.6	35.4	32.7	37.7
γ_s *(mJ/m^2)*	50.8	69.6	35.6	70.3
W_{adh} *(in air) (mJ/m^2)*	-	114.7	-	80.8
W_{adh} *(in water) (mJ/m^2)*	-	20.2	-	28.1

The surface roughness parameters (S_a and S_q) for both bare Si and ITO-PET substrates, as well as for nanofilms deposited on these substrates, are provided, along with the contact angles (Θ) of water and diiodomethane on both bare and nanofilm deposited substrates. Additionally, the calculated components of surface tension, both polar (γ^p_s) and apolar (γ^d_s), along with the overall surface tension (γ_s) for the bare substrates and the substrates with nanofilms, are included in Table 9.

As indicated in Table 9, the highest surface roughness was observed for the ITO-PET substrate, which has a rough surface, with S_a and S_q values of 30.5 and 44.5 nm, respectively. The surface roughness values of nanofilm deposited ITO-PET and Si substrates in Table 9 indicate that deposition of nanofilms on the substrates lead to a decrease in surface roughness. In this thesis, the contact angles of water and the highly dispersive diiodomethane measured on Si and ITO-PET substrates fall within the range of previously reported contact angles for water and apolar (dispersive) liquids like diiodomethane, hexadecane, ethylene glycol on Si and ITO substrates (Paniagua et al., 2008; Chen et al., 2019; Ozbay et al., 2020). The findings indicated that the water contact angles on nanofilm deposited Si (30.0 °) and ITO-PET (31.5 °) substrates were

quite similar, and notably lower compared to those measured on the bare substrates [See in Table 9]. The contact angle values on the nanofilms exhibit a higher hydrophilic nature compared to the bare Si and ITO-PET substrates as indicated in Figure 33.
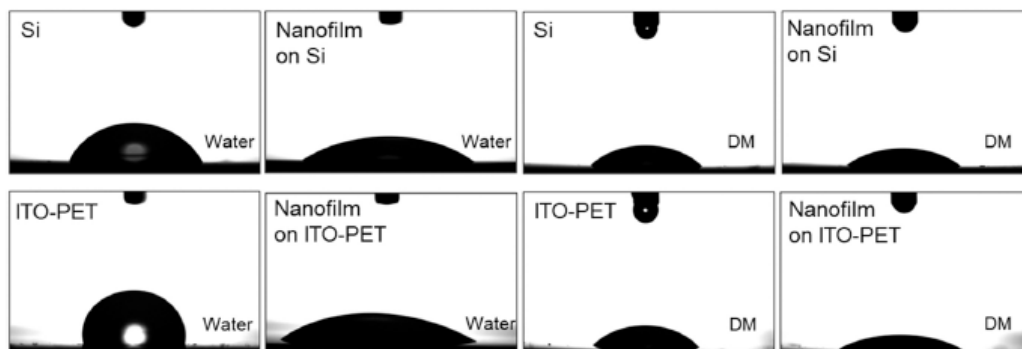
Figure 33. Images of the contact angles of water and diiodomethane (DM) on bare Si and ITO-PET substrate, nanofilm deposited on Si and ITO-PET substrates.

The total surface tensions for nanofilms, as well as for bare Si and ITO-PET substrates, were calculated by summing the polar and apolar surface tensions components. The determined total surface tension values for bare Si and ITO-PET substrates are 50.8 mJ/m^2, 35.6 mJ/m^2, respectively. These values are consistent with the previously measured surface free energy values for Si (44.8 mN/m) (Chai et al., 2014) and ITO (38.9 mJ/m^2) (Ozbay et al., 2020) surfaces, which were calculated using the Owens and Wendt model and the HM model, respectively.

As given in Table 9, the determined surface tension values of nanofilms coated on Si (69.6 mJ/m^2) and ITO-PET (70.3 mJ/m^2) substrates were quite similar. This similarity suggests that the nanofilms were successfully deposited on both Si and ITO-PET substrates using the LB technique.
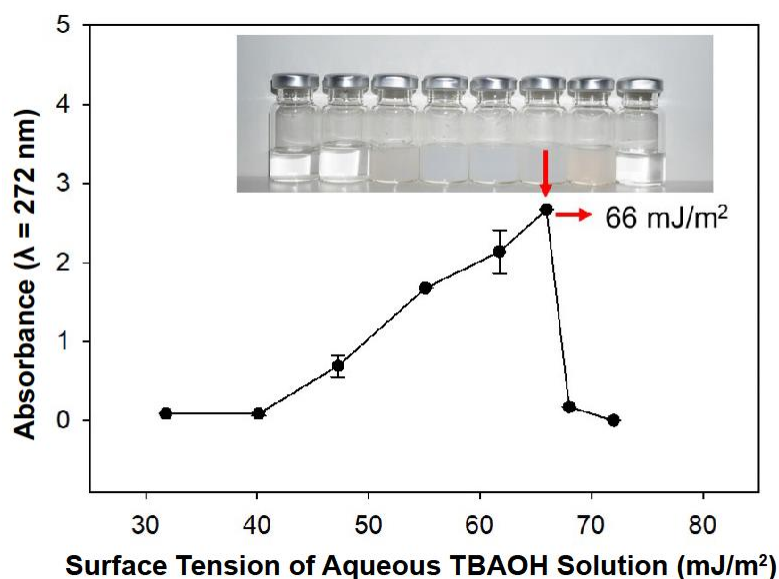
Figure 34. The absorbance values of exfoliated nanosheets measured in relation to the surface tensions of aqueous TBAOH solutions.

To optimize the energy efficiency of exfoliation and dispersion processes, it is ideal to use solvents whose surface energy closely resembles that of 2D materials (Shen et al., 2015). In the liquid-phase exfoliation of layered perovskites, the most favorable thermodynamic conditions for exfoliation and dispersion are achieved when the total surface tension of the solvent matches that of the nanosheets (Chhowalla et al., 2013; Shen et al., 2015; Zhang et al., 2019). As shown in Figure 34, optimal exfoliation and dispersion of nanosheets were attained in TBAOH solution with a surface tension of 66 mJ/m^2. This value, indicative of the surface tension of nanosheets, closely aligns with the total surface tensions of the nanofilms on Si and ITO-PET substrates, as determined from the contact angle measurements and mathematical modeling. Consequently, this correlation confirms the accuracy of the determined total surface tensions for the nanofilms on Si and ITO-PET substrates.
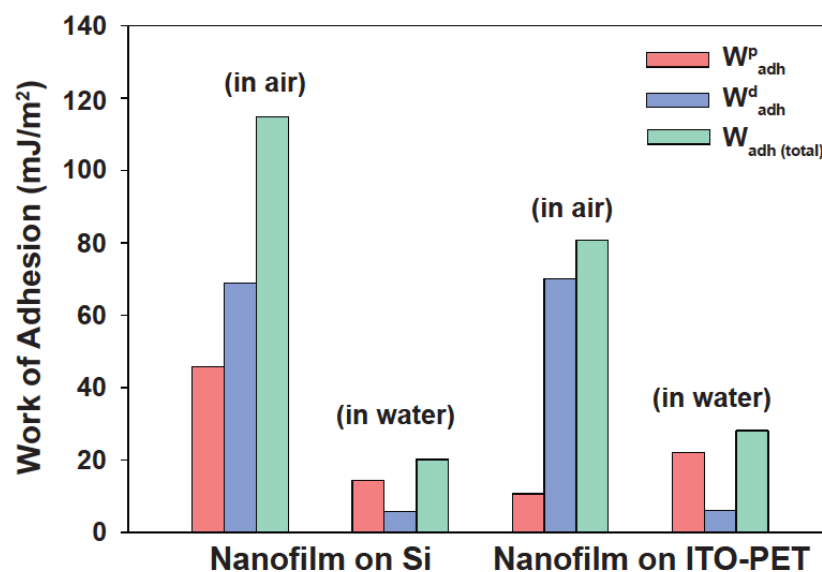
Figure 35. Polar (W^p_{adh}) and apolar (W^d_{adh}) components of work of adhesion, total work of adhesion (W_{adh}), calculated for the interaction between nanofilms and both Si and ITO-PET substrates in air/ water based on the thermodynamic HM model.

The adhesion of nanofilms to Si and ITO-PET substrates were determined to be thermodynamically favorable, as both polar and apolar components of the work of adhesion are positive in both air and water [See in Figure 35]. In air, the adhesion is predominantly driven by dispersive forces, such as van der Waals interactions, while in water, it shifts to polar interactions, especially hydrogen bonding. This stronger polar interaction between the nanosheets and ITO-PET in water is attributed to potential hydrogen bonds between the electronegative oxygen atoms in the nanosheets and ITO, resulting in the total work of adhesion being lower in water than in air (Swint and Bohn, 2004). Additionally, as shown in Figure 35, the nanofilm adheres more strongly to Si in air but demonstrates greater adherence to ITO-PET in water [See in Table 9].

3.4. Patterning of LB Films by EBL and Optic Lithography Techniques and Capacitor Production and Characterization

3.4.1. Patterning of LB films on Si, Ti/Au-glass, Ti/Au-Si and ITO-glass substrates by EBL and their characterization
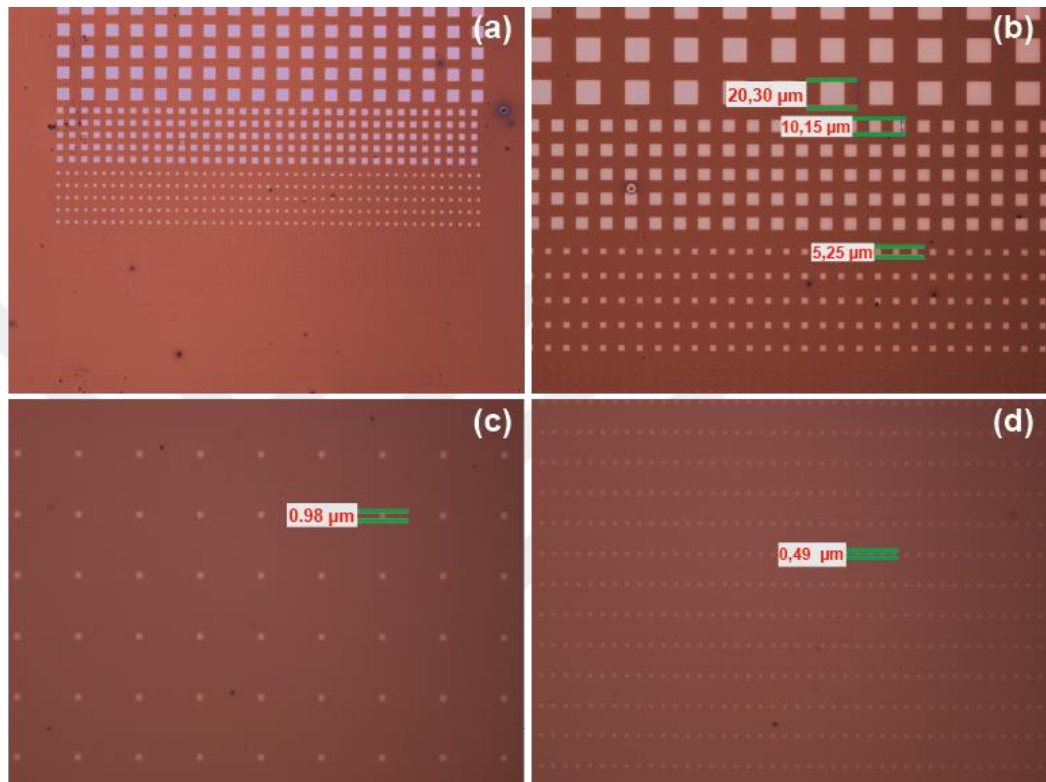
Figure 36. The optical microscope images of (a) patterns obtained by EBL on Si substrate, (b) patterns in the dimensions of 20 x 20 μm^2, 10 x 10 μm^2, and 5 x 5 μm^2, respectively, (c) patterns obtained in the dimensions of 1 x 1 μm^2, (d) patterns obtained with dimensions of 0.5 x 0.5 μm^2.

For ITO-PET/Sample 1, EBL was performed by securing it to a Si substrate, due to the flexible nature of the ITO-PET substrate. This was aimed to ensure a flatter surface for smoother EBL patterning on the flexible ITO-PET substrates. However, despite this approach, ITO-PET/Sample 1 could not be patterned using the EBL technique. The PMMA typically used in EBL ranges between 70-80 nm in thickness. Since magnetic sputtering cannot deposit layers thinner than 70 nm, the initial EBL experiments were carried out on nanofilm-deposited Si substrates. To pattern these substrates, PMMA A4 was replaced with PMMA A2 to decrease the thickness of the

resist. A dose range of 1200-1300 $\mu C/m^2$ was determined as effective for creating patterns. Therefore, square patterns of 20 x 20 μm^2, 10 x 10 μm^2, 5 x 5 μm^2, 1 x 1 μm^2, 500 x 500 nm^2, 300 x 300 nm^2, 200 x 200 nm^2, 100 x 100 nm^2, and 50 x 50 nm^2 were created on the Si substrate. After EBL was performed, the resist was stripped using acetone, and Ti/Au was deposited on the patterned Si substrate to form electrodes on the nanofilm. Figure 36 (a) shows the resultant patterns on the Si substrate, demonstrating the successful application of EBL on the monolayer nanofilm on the Si substrate containing $Ca_2NaNb_4O_{13}$ nanosheets.
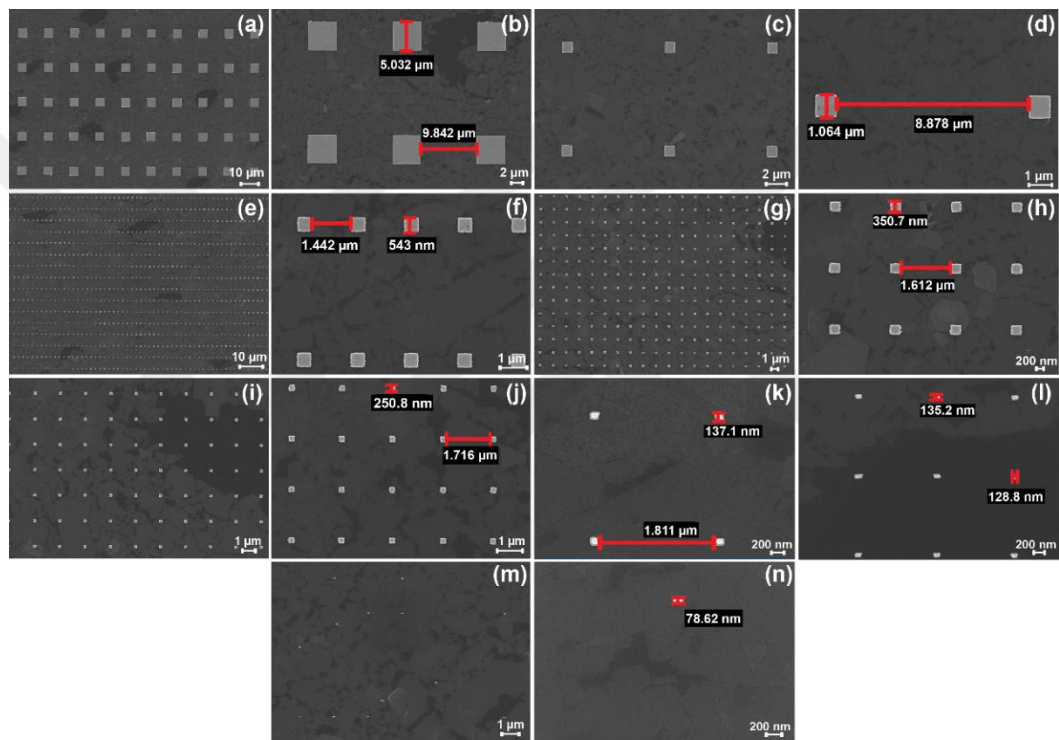
Figure 37. SEM images of EBL application on nanofilm-deposited Si substrates are as follows: (a) a general view of the patterns in 5 x 5 μm^2 dimensions, (b) the horizontal dimensions of 5 x 5 μm^2 patterns, (c) a general image of 1 x 1 μm^2 patterns, (d) the patterns in 1 x 1 μm^2 dimensions and their horizontal spacing, (e) a general view of 500 x 500 nm^2 patterns, (f) an image showing the dimensions of square patterns and their lateral distances from each other, (g) a general view of 300 x 300 nm^2 patterns, (h) an image of the size and horizontal distances of the 300 x 300 nm^2 patterns, (i) an image of 200 x 200 nm^2 patterns and their horizontal spacing, (j) an image of 200 x 200 nm^2 patterns, (k), (l) an image of the patterns in 100 x 100 nm^2 dimensions, (m) a general view of 50 x 50 nm^2 patterns, (n) patterns in 50 x 50 nm^2 dimensions.

Figure 37 (a) illustrates the successful application of EBL for depositing Ti/Au electrodes on nanofilm-deposited Si substrates. As depicted in Figure 37 (b), Ti/Au electrodes measuring 5 x 5 μm^2 were produced, with a spacing of approximately 10 μm between them. The patterned area, shown in Figure 37 (a), is uniformly covered with a monolayer nanofilm. Patterns of 1 x 1 μm^2 dimensions are presented in Figure 37 (c), featuring a horizontal spacing of about 10 μm, and the dimensions of these patterns are around 1 μm, as seen in Figure 37 (d). The SEM image in Figure 37 (e) shows 500 nm square patterns created by EBL, with almost all electrodes positioned on the nanofilm-deposited Si substrate. In Figure 37 (f), the 500 x 500 nm^2 patterns are spaced around 1 μm apart. Figure 37 (g) demonstrates the successful EBL fabrication of 300 nm square Ti/Au electrodes on a monolayer nanofilm on the Si substrate. Most of these electrodes are positioned on the monolayer nanofilms, facilitating their use in AFM measurements. The Ti/Au electrodes in Figure 37 (h) are roughly 350 nm in size, with a spacing of about 2 μm between the patterns. Figure 37 (i) shows 250 nm square patterns on monolayer nanofilm, and Figure 37 (j) shows 250 x 250 nm^2 patterns with a 2 μm spacing between the patterns. Despite their smaller size, the 250 nm square patterns in Figure 37 (i) are neatly patterned. In Figure 37 (k), the patterns are clearly seen on monolayer nanofilm, measured approximately 137 nm in size. The horizontal spacing between the 100 nm square pattern is measured about 2 μm. Also, another image of these patterns provided in Figure 37 (l), showing square patterns measured 135 nm in length and around 130 nm in width. The general view of 50 nm square patterns was given in Figure 37 (m), where these nanoscale electrodes are less orderly positioned than other electrodes. Figure 37 (n) presents that the patterns are approximately 80 nm in size and are mostly positioned on monolayer nanofilm. This shows the first successful instance of metal patterning on nanofilm composed of perovskite nanosheets using EBL technique.
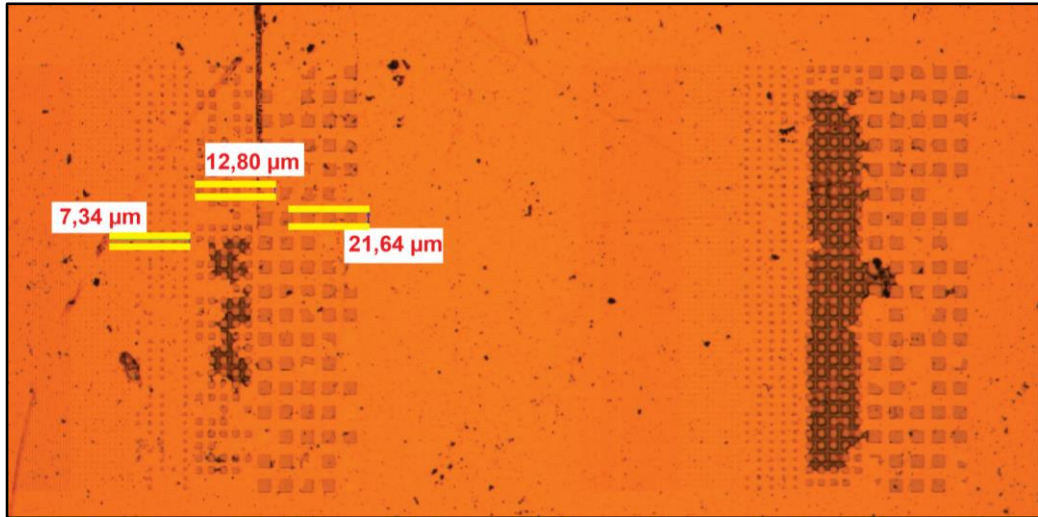
Figure 38. Optical microscope image of the EDL application performed on two-layer nanofilm-deposited Ti/Au-glass substrate, patterns in 5 x 5 μm^2, 10 x 10 μm^2, and 20 x 20 μm^2, respectively.

Figure 38 presents an optical microscope view of the Ti/Au-glass substrate patterned using the EBL technique. The patterns on this substrate include various micro and nanoscale sizes: 20 x 20 μm^2, 10 x 10 μm^2, 5 x 5 μm^2, 1 x 1 μm^2, 500 x 500 nm^2, 300 x 300 nm^2, and 250 x 250 nm^2, as shown in Figure 38. Therefore, Figure 39 presents the SEM images of patterns created on the two-layer nanofilm – deposited Ti/Au-glass substrate using the EBL technique.
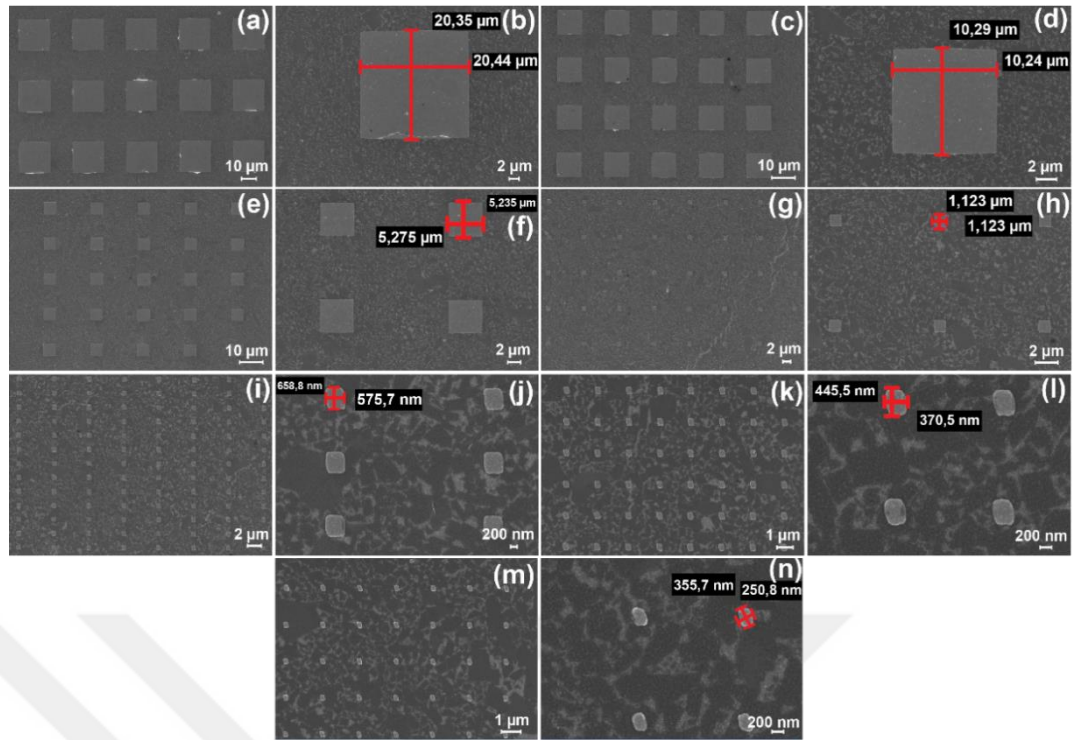
Figure 39. SEM images of the EBL application on two-layer nanofilm-deposited Ti/Au-glass substrates, (a) an overall view of the patterns in 20 x 20 μm^2 dimensions, and (b) their detailed dimensions, (c) an overall view of 10 x 10 μm^2 patterns, with (d) a close-up of their dimensions, (e) a broad general view of 5 x 5 μm^2 Ti/Au electrodes, and (f) their specific dimensions, (g) an overall view of 1 x 1 μm^2 electrodes, with (h) a focus on their dimensions, (i), (j) displaying general and detailed images of the 500 nm square patterns, respectively, (k), (l) presenting both general and detailed views of 300 nm square electrodes, and (m), (n) showing both general and detailed images of the 250 x 250 nm^2 electrodes.

Figure 39 shows the EBL application on the Ti/Au-glass substrate deposited with a two-layer nanofilm. In Figure 39 (a), the effective placement of Ti/Au electrodes on the two-layer nanofilm-deposited Ti/Au-glass substrate using EBL is demonstrated. Figure 39 (b) indicates that the Ti/Au patterns, aimed to be 20 x 20 μm^2 in dimensions, actually measured 20.35 and 20.44 μm. Additionally, Figure 39 (a) confirms that the metal-deposited area is fully covered with nanosheets. The 10 x 10 μm^2 patterns are completely positioned on the nanofilm layer, as shown in Figure 39 (c), and Figure 39 (d) demonstrates that these patterns are approximately 10 μm in size. Figure 39 (e) presents the SEM image of the metal patterns aimed to be 5 x 5 μm^2, while Figure 39

(f) provides a detailed view of these nearly 5 μm metal patterns positioned on the two-layer nanofilm. Figure 39 (g) shows the metal patterns of approximately 1 μm square on the Ti/Au-glass substrate, with their actual size being 1.123 μm, as seen in Figure 39 (h). Figure 39 (i) features a general view of the 500 nm square Ti/Au electrodes, and Figure 39 (j) reveals these patterns to be 558.8 nm and 575.7 nm. The patterns of 300 x 300 nm^2, as shown in Figure 39 (k), are measured to be 370.5 and 445.5 nm in Figure 39 (l). The general view of the 250 nm square patterns is presented in Figure 39 (m), with their dimensions being 355.7 nm in length and 250.8 nm in width, as detailed in Figure 39 (n). Attempts were made to create even smaller patterns in this experiment, but they were not successfully fabricated.
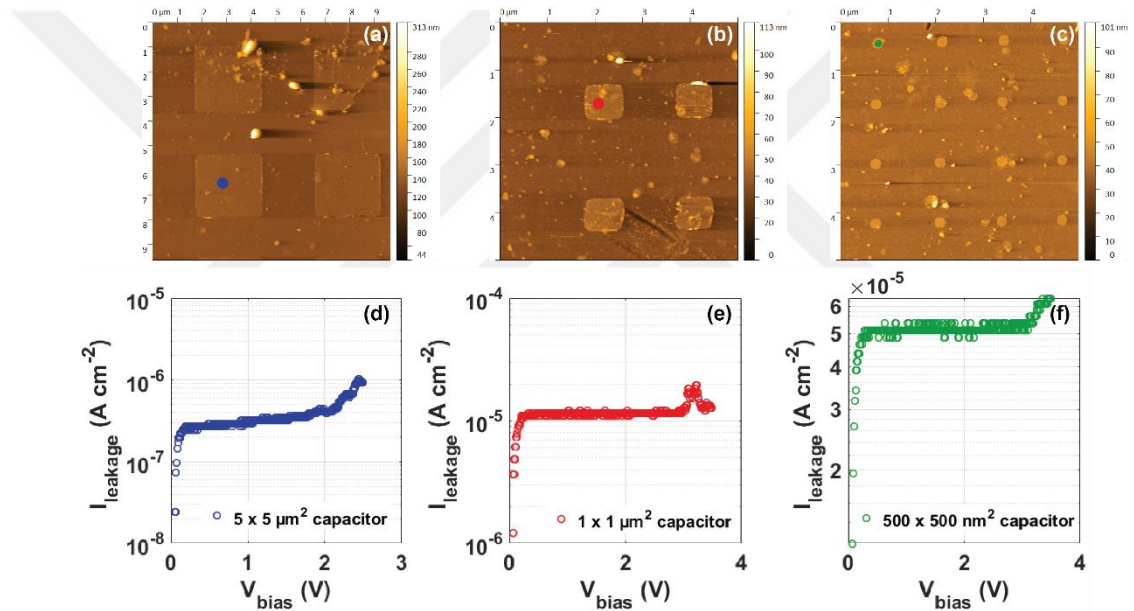
Figure 40. c-AFM measurement on two-layer nanofilm-deposited Ti/Au-glass substrate, AFM images of (a) 5 x 5 μm^2 Ti/Au capacitors, (b) 1 x 1 μm^2 Ti/Au capacitors, (c) 500 x 500 nm^2 Ti/Au capacitors, I-V curves of (d) 5 x 5 μm^2 Ti/Au capacitors, (e) 1 x 1 μm^2 Ti/Au capacitors, and (f) 500 x 500 nm^2 Ti/Au capacitors.

In Figure 40 (a), (b), and (c), the dots on the Ti/Au capacitors indicate the I-V measurement points on the capacitor. In Figure 40 (d), the leakage current values of 5 x 5 μm^2 capacitors were measured as 2.927 x 10^{-7} A/cm^2 at 0.5 V, showing excellent insulating properties compared to previously fabricated $Ca_2Nb_3O_{10}$ nanosheet capacitors on $Ru_{0.95}O_2$ coated quartz substrates (Khan et al., 2017). The breakdown voltage for capacitor is at 2 V with a leakage current of 4.146 x 10^{-7} A/cm^2.

Furthermore, 1 x 1 μm^2 Ti/Au capacitors have a leakage current of 1.158 x 10^{-5} A/cm^2 at 0.5 V [See in Figure 40 (e)]. The breakdown leakage current for 1 x 1 μm^2 Ti/Au capacitors is determined at 3 V as 1.219 x 10^{-5} A/cm^2. This increase in leakage current is due to possible leakage paths occurred during the EBL process. On the other hand, the AFM image in Figure 40 (c) for 500 x 500 nm^2 Ti/Au capacitors reveals the deformation of patterns from square to circular. Despite this deformation, I-V measurement on these nanoscale capacitors was successfully performed. The leakage current at 0.5 V was determined as 5.122 x 10^{-5} A/cm^2, while the breakdown was occurred at 3 V. For the Ti/Au capacitors fabricated on Ti/Au-glass substrates, 5 x 5 μm^2 capacitors exhibited the lowest leakage current and are in good agreement with the literature (Wang et al., 2014).
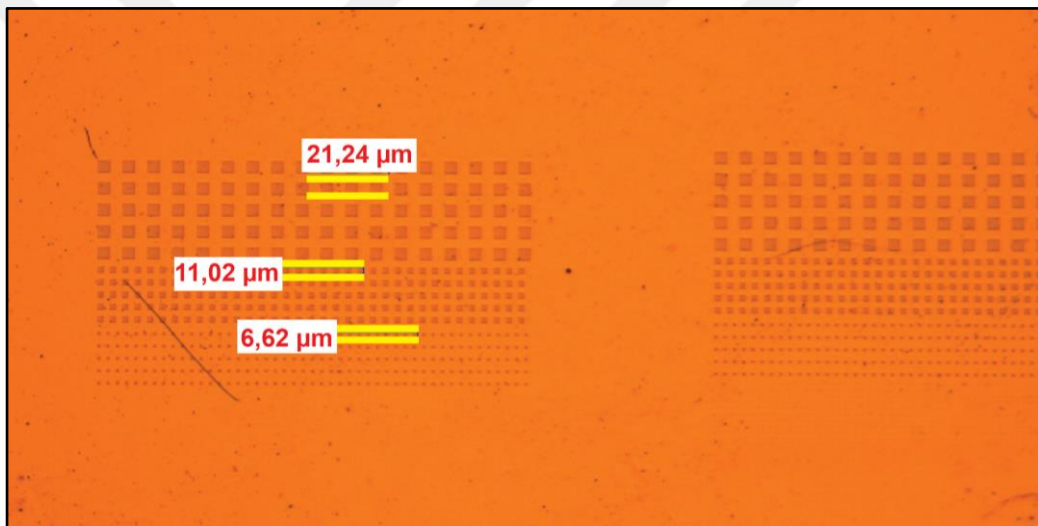
Figure 41. Optical microscope image of EBL application performed on two-layer nanofilm-deposited Ti/Au-Si substrate.

Figure 41 shows the optical microscope image of patterns created on the Ti/Au-Si substrate using the EBL technique with various dimensions: 20 x 20 μm^2, 10 x 10 μm^2, and 5 x 5 μm^2. Figure 41 further provides detailed SEM images, showing a range of square pattern sizes –20 x 20 µm, 10 x 10 µm, 5 x 5 µm, 1 x 1 µm, 500 x 500 nm, 300 x 300 nm, and 250 x 250 nm – that were effectively fabricated on the Ti/Au-Si substrate.
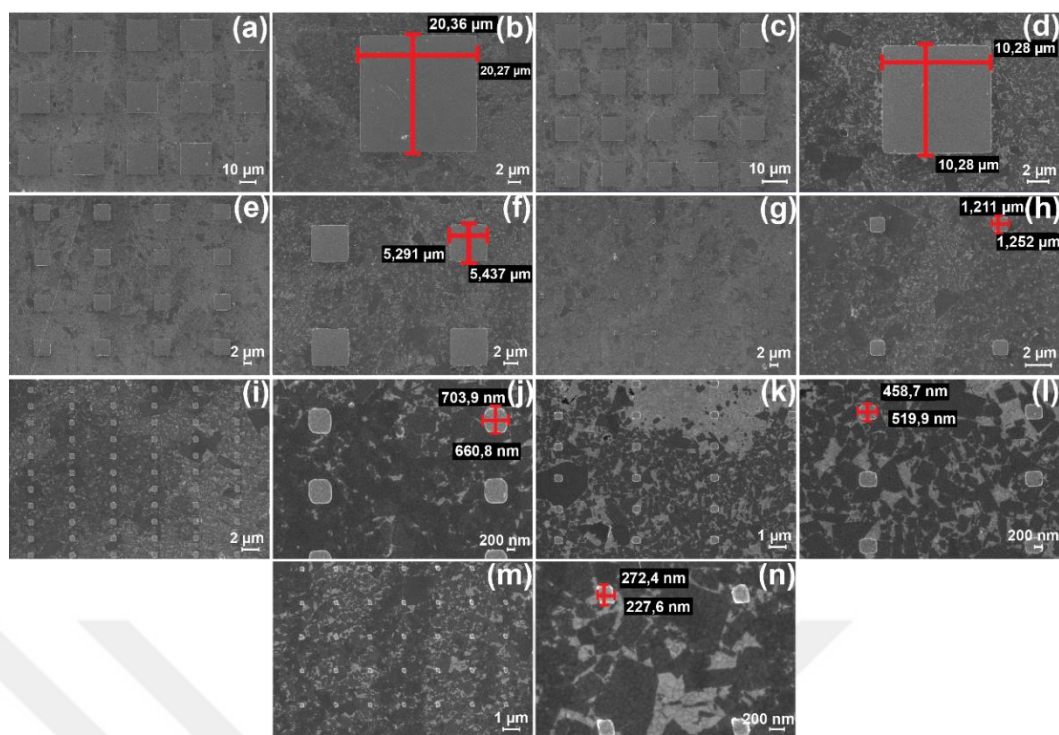
Figure 42. SEM images of EBL application on the two-layer nanofilm-deposited Ti/Au-Si substrate including: (a) a general view of the patterns aimed to be 20 x 20 μm^2 in size, along with (b) their detailed dimensions, (c) an overall view of the 10 μm square Ti/Au electrodes, and (d) their specific dimensions, (e) a general view of 5 x 5 μm^2 electrodes, with (f) detailed dimensions of these patterns, (g) a general view of 1 μm square electrodes, complemented by (h) a close-up of their dimensions, (i) an overall view of 500 x 500 nm^2 electrodes, with (j) a detailed image of these patterns, (k), (l) providing a general and detailed view of 300 nm square electrodes, respectively, and finally, (m) an overall view of the electrodes of 250 x 250 nm^2 dimensions, with (l) a close-up view showing the actual sizes of these patterns.

The SEM images in Figure 42 present the EBL results on the two-layer nanofilm-deposited Ti/Au-Si substrate. Figure 42 (a) demonstrates the effective EBL patterning of Ti/Au electrodes onto two-layer nanofilm containing $Ca_2NaNb_4O_{13}$ nanosheets. As shown in Figure 42 (b), the targeted 20 x 20 μm^2 Ti/Au patterns are approximately 20 μm in size. Figures 42 (c), (d) reveal that the resulting patterns measures around to be 10 μm in both length and width. Figures 42 (e), (f) depict the SEM images of metal patterns aimed to be 5 x 5 μm^2. Figure 42 (g) presents a general view of 1 x 1 μm^2 patterns, which actually measure 1.211 μm in length and 1.252 μm in width, as shown

in Figure 42 (h). The intended 500 x 500 nm^2 patterns, presented in Figure 42 (i), turn out to be larger, measuring 703.9 and 660.8 nm, as detailed in Figure 42 (j). Figure 42 (k) provides a general view of the 300 x 300 μm^2 patterns, found to be larger than expected, as indicated in Figure 42 (l). Figure 42 (m) offers a general view of the 250 nm square patterns, with Figure 42 (n) showing their dimensions as 272.4 nm in length and 227.6 nm in width. Despite their smaller size, the 250 nm patterns in Figure 42 (n) are well-patterned using EBL technique. These patterns were fabricated not only on the two-layer nanofilm but also at their intersections. Overall, Figure 42 confirms the successful placement of all intended Ti/Au electrodes on the nanofilm-deposited Ti/Au-Si substrate.
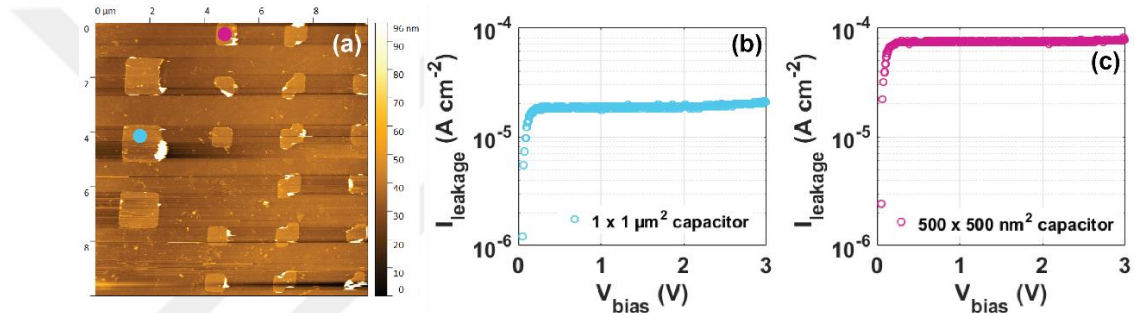
Figure 43. c-AFM measurement on two-layer nanofilm-deposited Ti/Au-Si substrate, AFM images of (a) 1 x 1 μm^2 and 500 x 500 nm^2 Ti/Au capacitors, I-V curves of (b) 1 x 1 μm^2 Ti/Au capacitors, and (c) 500 x 500 nm^2 Ti/Au capacitors.

Figure 43 shows the c-AFM measurement conducted on a two-layer nanofilm deposited on the Ti/Au-Si substrate for the 1 x1 μm^2 and 500 x 500 nm^2 Ti/Au capacitors. The blue dot in Figure 43 (a) indicates the selected I-V measurement point on the Ti/Au capacitor. This selection was based on the current map obtained using the c-AFM to identify which capacitor exhibited current leakage. At low bias, the capacitor demonstrated great insulating properties, as seen in Figure 43 (b). At 0.5 V, the leakage current was measured at 1.829 x 10^{-5} A/cm^2. This value is slightly greater than the previously indicated threshold ($< 10^{-7}$ A/cm^2) of 50 μm diameter Au dot fabricated on nanosheets-structured nanofilms (Wang et al., 2014), attributed to creation of possible leakage currents on the capacitors during the EBL process. For the 500 x 500 nm^2 capacitors, as shown in Figure 43 (a) and indicated with the pink dot, great insulating property was observed, with a slight increase in leakage current at 0.5

V to 7.317 x 10^{-5} A/cm^2. As seen in Figure 43 (a), some of the 500 x 500 nm^2 capacitors have deformation that occurred during the EBL process. 1 x 1 μm^2 capacitors exhibited the lowest leakage current among all capacitors fabricated on the two-layer nanofilm-deposited Ti/Au-Si substrate. The leakage current of 1 x 1 μm^2 capacitors on both Ti/Au-glass and Ti/Au-Si substrates exhibited similar leakage currents, measured as ~10^{-5} A/cm^2 at 0.5 V.
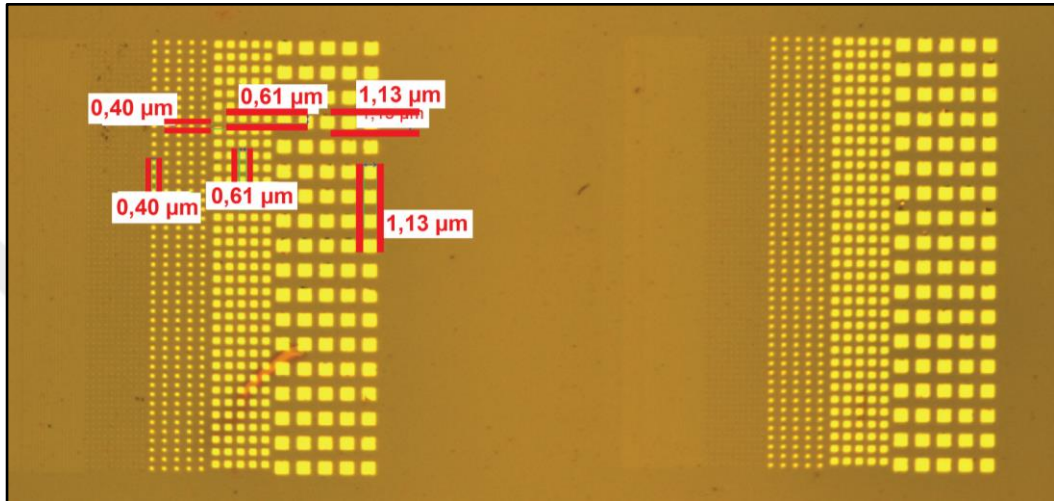
Figure 44. Optical microscope image of the EBL application performed on the two-layer nanofilm-deposited ITO-glass substrate.

Figure 44 presents the optical microscope image of patterns fabricated using the EBL technique on the two-layer nanofilm-deposited ITO-glass substrate. The general layout of the patterns confirms the successful fabrication of Ti/Au electrodes with dimensions of 1 x 1 μm^2, 500 x 500 nm^2, and 300 x 300 nm^2, as shown in Figure 40. The SEM imaging of these patterns verifies the effective EBL patterning of all the planned Ti/Au electrodes on the two-layer nanofilm-deposited ITO-glass substrate [See in Figure 45]. In Figure 45, the nanofilm shows regional variations in the positions of the $Ca_2NaNb_4O_{13}$ nanosheets.
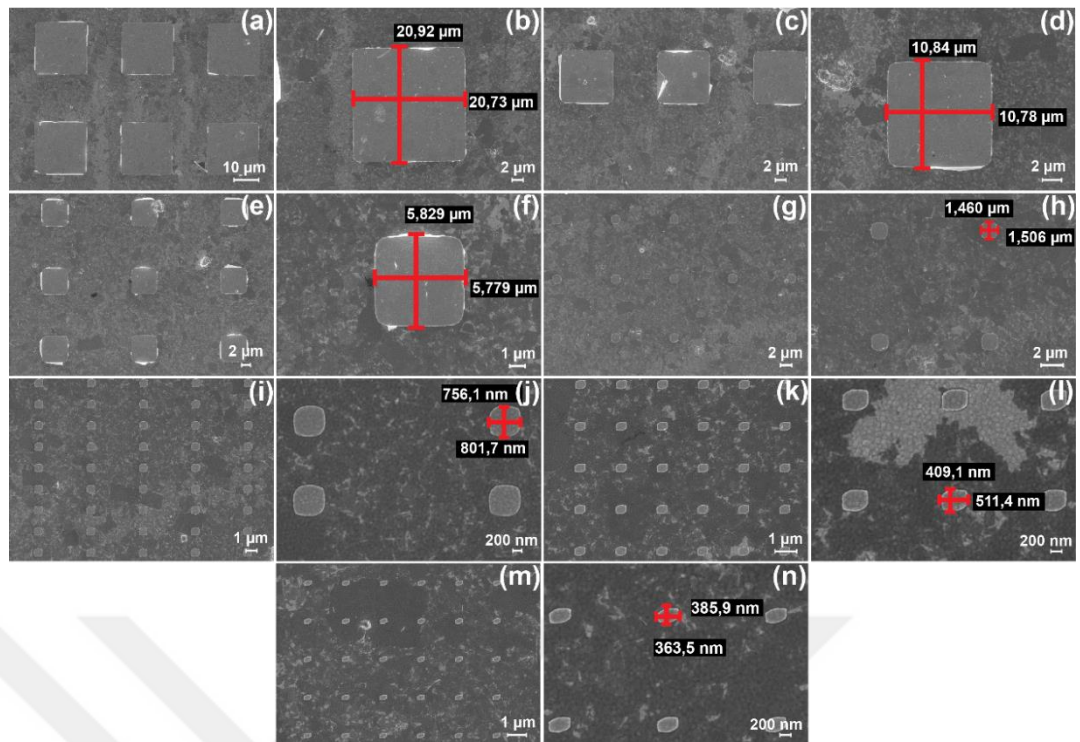
Figure 45. SEM images of the EBL application on the ITO-glass substrate deposited two layers of nanofilm include: (a) an overall view of patterns aimed to be 20 x 20 μm^2, and (b) detailed dimensions of these patterns, (c) an overall view of the 10 μm square Ti/Au electrodes, with (d) their specific dimensions, (e) a general view of the 5 x 5 μm^2 electrodes, with (f) detailed dimensions of these patterns, (g) a general view of the 1 x 1 μm^2 electrodes, complemented by (h) a close-up of their dimensions, (i) an overall view of the 500 nm square electrodes, with (j) a detailed view of these patterns, (k) a general view of the 300 x 300 nm^2 electrodes, and (l) a close-up view of their dimensions, (m) a general view of the electrodes measuring 250 x 250 nm^2, and (n) a detailed view of these patterns.
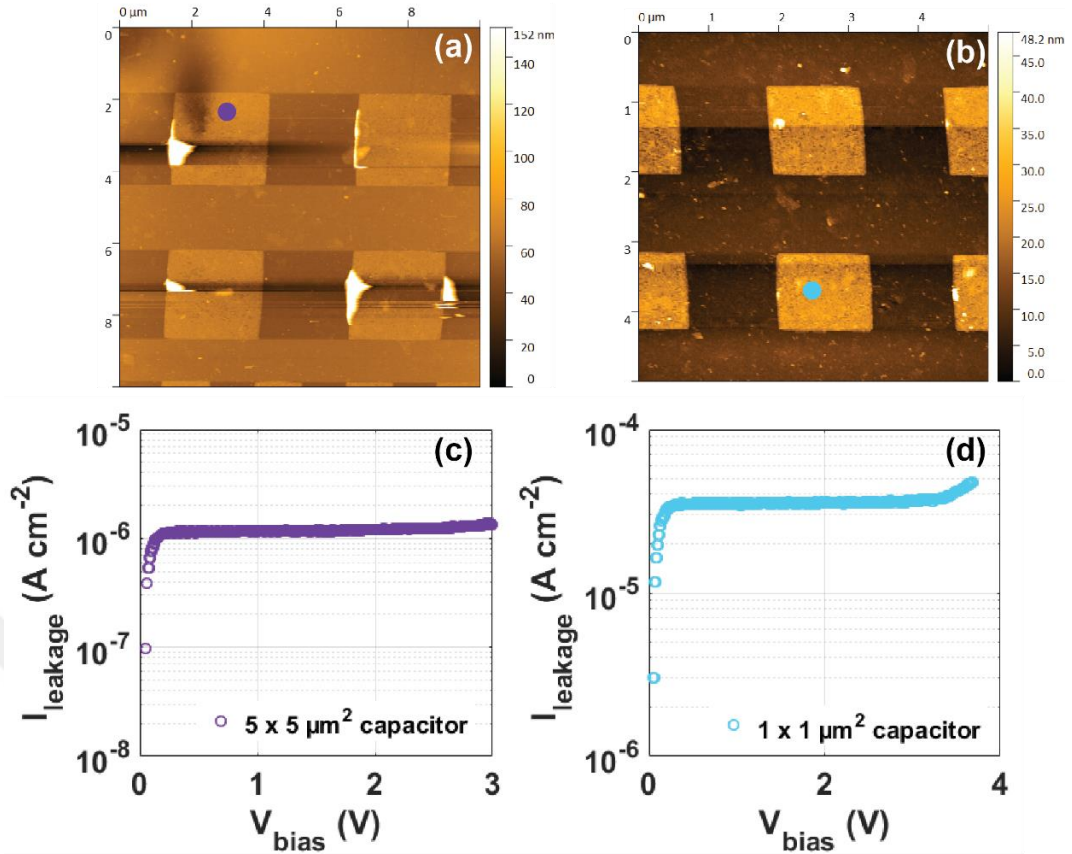
Figure 46. c-AFM measurement on two-layer nanofilm-deposited ITO-glass substrate, AFM images of (a) 5 x 5 µm² Ti/Au capacitors, and (b) 1 x 1 µm² Ti/Au capacitors, I-V curves of (c) 5 x 5 µm² Ti/Au capacitors, and (d) 1 x 1 µm² Ti/Au capacitors.

Figure 46 (a) and (b) displays 5 x 5 µm² and 1 x 1 µm² Ti/Au capacitors fabricated on the two-layer nanofilm-deposited ITO-glass substrate. The AFM images in Figure 46 (a) and (b) clearly show that the Ti/Au capacitors are fabricated on the nanofilms without any major deformation during the EBL process. The leakage current for the 5 x 5 µm² capacitor was measured at 0.5 V as 1.171×10^{-6} A/cm², slightly greater compared to previously determined threshold, suggesting the presence of more significant leakage current paths on the capacitor (Khan et al., 2017). In contrast, the 1 x 1 µm² capacitors exhibited a leakage current of 3.476×10^{-5} A/cm² at 0.5 V. They also showed a breakdown at approximately 3.3 V, with a leakage current of 3.841×10^{-5} A/cm², increasing to 4.756×10^{-5} A/cm² while maintaining their insulating properties at low bias. The differences between these capacitors may be attributed to errors in the Ti/Au deposition during the fabrication step. Again, the leakage current values for 1 x 1 µm² capacitors were similar to those of other 1 x 1 µm² capacitors

fabricated on Ti/Au-glass and Ti/Au-Si substrates, with a slight increase from the previously determined leakage current values (Wang et al., 2014), maintaining good insulating properties at low bias. For 5 x 5 μm^2 capacitors on ITO-glass substrates, there was a slight difference compared to other 5 x 5 μm^2 capacitors fabricated on Ti/Au-glass substrates, with a slight increase from ~10^{-7} A/cm^2 to ~10^{-6} A/cm^2.

Overall, the capacitors fabricated using the EBL technique exhibited great insulating properties. The decrease in the capacitor scales from micro to nanometers resulted in slight deformations on the capacitors, leading to greater leakage current paths. The capacitors fabricated on glass substrates exhibited the lowest leakage currents, and the most suitable scale for capacitor fabrication was determined to be 5 x 5 μm^2.

3.4.2. Patterning of LB films on ITO-PET substrates by optic lithography and characterization of ITO electrodes

Alongside EBL experiments, the optical lithography technique was applied as an alternate method for patterning ITO-PET substrates. As demonstrated in Figure 30, the experiments involved analyzing the UV/Vis transmittance spectrum of 10-layer, 15-layer, and 20-layer $Ca_2NaNb_4O_{13}$ nanofilms, which were deposited on ITO-PET/Sample 4, ITO-PET/Sample 5, and ITO-PET/Sample 6 using the LB method, respectively. Prior to these patterning experiments nanofilm-deposited ITO-PET substrates, the initial application of optical lithography was carried out on a bare ITO-PET substrate.
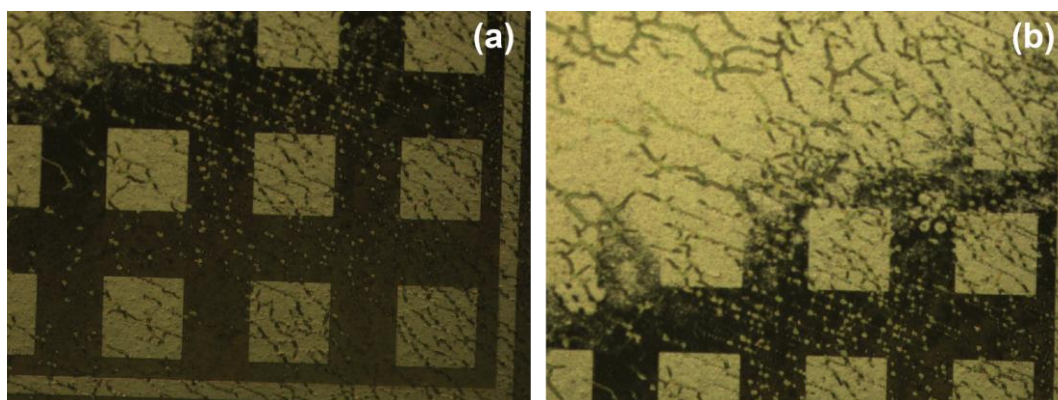
Figure 47. Optical microscope images of the optical lithography application on the bare ITO-PET substrate include: (a) patterns anticipated as a result of the optical lithography, and (b) patterns that were not successfully created by the optical lithography process.

The optical microscope image in Figure 47 (a) demonstrates patterns created on the surface of the bare ITO-PET substrate using the optical lithography technique. However, Figure 47 (b) reveals incomplete exposure of these patterns, leading to difficulties in effectively vacuuming the flexible ITO-PET substrate. Consequently, the optical lithography process was then applied to nanofilm – deposited ITO-PET substrates, specifically to 10-layer nanofilm – deposited ITO-PET/Sample 4, 15- layer ITO-PET/Sample 5, and 20-layer ITO-PET/Sample 6.
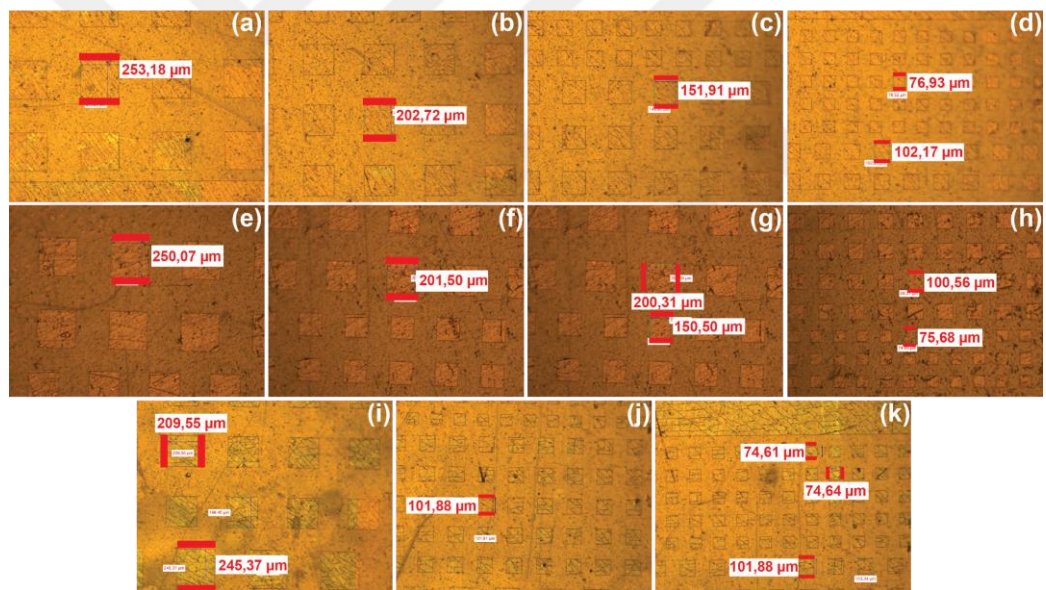
Figure 48. Optical lithography technique was applied to 10 -layer nanofilm-deposited ITO-PET/Sample 4 to create square patterns of various sizes. The optical microscope images show the dimensions of these patterns as follows: (a) 250 x 250 μm^2, (b) 200 x 200 μm^2, (c) 150 x 150 μm^2, and (d) 100 x 100 μm^2 and 75 x 75 μm^2. For 15-layer nanofilm-deposited ITO-PET/Sample 5, the optical lithography patterns were created with dimensions of (e) 250 x 250 μm^2, (f) 200 x 200 μm^2, (g) 150 x 150 μm^2, and (h) 100 x 100 μm^2 and 75 x 75 μm^2 produced. Lastly, for 20-layer nanofilm-deposited ITO-PET/Sample 6, the optical lithography was used to fabricate patterns

measuring (i) 250 x 250 µm^2 and 200 x 200 µm^2, (j) 100 x 100 µm^2, and (k) 75 x 75 µm^2.

Figure 48 shows the optical microscope images of optical lithography applied to 10-layer ITO-PET/Sample 4, 15-layer ITO-PET/Sample 5, and 20-layer ITO-PET/Sample 6. The mask used in these experiments contained square patterns of five different sizes as follows: 250 x 250 µm^2 [See in Figure 48 (a), (e), (i)], 200 x 200 µm^2 [See in Figure 48 (b), (f), (i)], 150 x 150 µm^2 [See in Figure 48 (c), (g)], 100 x 100 µm^2 [See in Figure 48 (d), (h), (j)], and 75 x 75 µm^2 [See in Figure 48 (d), (h), (k)].
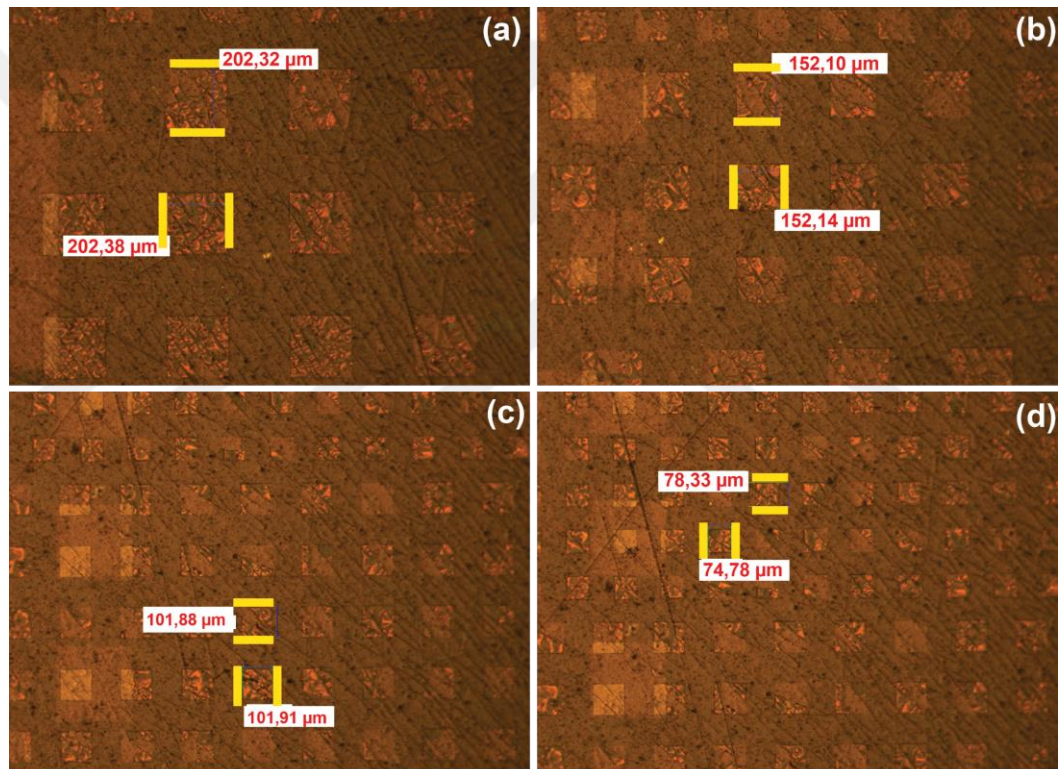
Figure 49. Optical microscope images of ITO-PET/Sample 4, ITO-PET/Sample 5, and ITO-PET/Sample 6 after the optical lithography process, ITO deposition, and resist removal are as follows: (a) dimensions of 200 x 200 µm^2 electrodes, (b) dimensions of 150 x 150 µm^2 electrodes, (c) dimensions of 100 µm square ITO electrodes, and (d) dimensions of 75 x 75 µm^2 electrodes.

After the ITO deposition using magnetic sputtering on 10-layer ITO-PET/Sample 4, 15-layer ITO-PET/Sample 5, and 20-layer ITO-PET/Sample 6, detailed optical

microscope images in Figure 49 show the dimensions of patterns and their distances from each other. Figure 49 (a) reveals that the ITO electrodes, intended to be 200 x 200 μm^2, measured approximately 202 μm in both length and width. The electrodes aimed to be 150 x 150 μm^2 were found to be about 152 μm. The 100 μm square patterns measured around 102 μm. The minor variations in the dimensions of the electrodes are due to the rougher surface of the ITO-PET substrates compared to Si substrates. Thus, it was confirmed that ITO was successfully deposited on the electrodes by magnetic sputtering, and square patterns of five different sizes were effectively created on ITO-PET samples with 10, 15, and 20 layers of nanofilm using optical lithography.

3.5. Structural, Mechanical, Electrical and Optical Characterization of Ultra-Thin Capacitors

3.5.1. Optical analysis of LB nanofilms
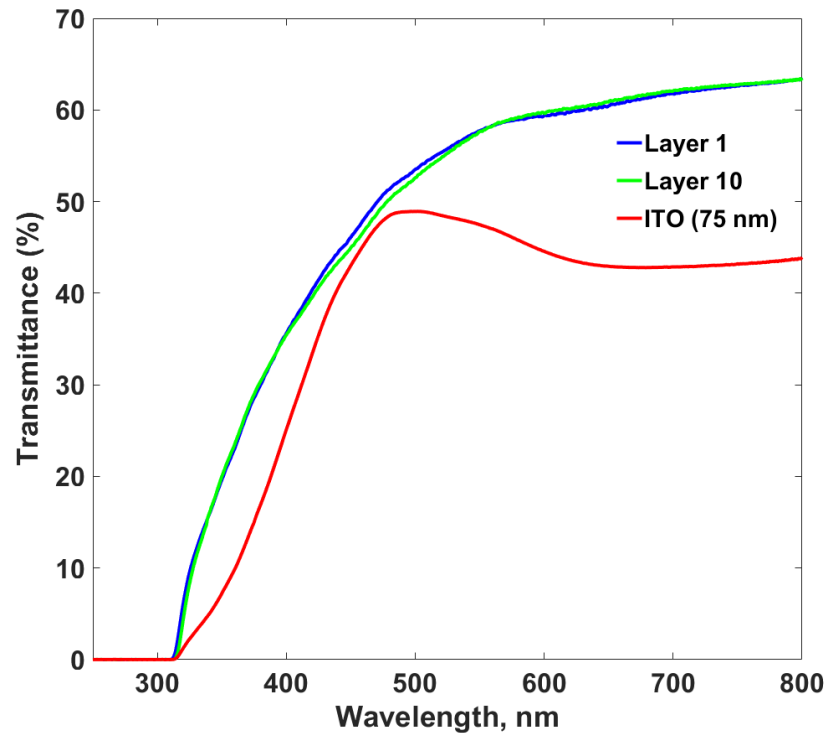
Figure 50. UV/Vis transmittance spectrum of 10-layer nanofilm-deposited ITO-PET/Sample 3 and 75 nm ITO.

Figure 50 shows the UV/Vis transmittance spectra of ITO-PET/Sample 3, which has been deposited with a 10-layer nanofilm and subsequently with 75 nm of ITO

using the magnetic sputtering method, without applying optical lithography. The transparency of nanofilm layers, initially at 65%, decreases by 10% after the ITO deposition. Notably, at the 460 nm wavelength, a 2% decrease in transparency is observed both between Layer 1 and Layer 10, and also between Layer 10 and the ITO layer. This sequential decrease in transparency, as indicated in Figure 50, confirms the effective transfer of coatings onto the ITO-PET substrate.

3.5.2. Spectral reflectance analysis of LB nanofilms

Due to the unknown reflectance values and optical constants of nanofilms containing $Ca_2NaNb_4O_{13}$ nanosheets on ITO-PET substrates, optimal optical modeling was conducted using the TiO_6 octahedral and ITO references from the Filmetrics database. This approach was chosen because of the structural similarity between the TiO_6 octahedral unit and the NbO_6 octahedral unit present in $Ca_2NaNb_4O_{13}$ nanosheets (Kim et al., 2016).
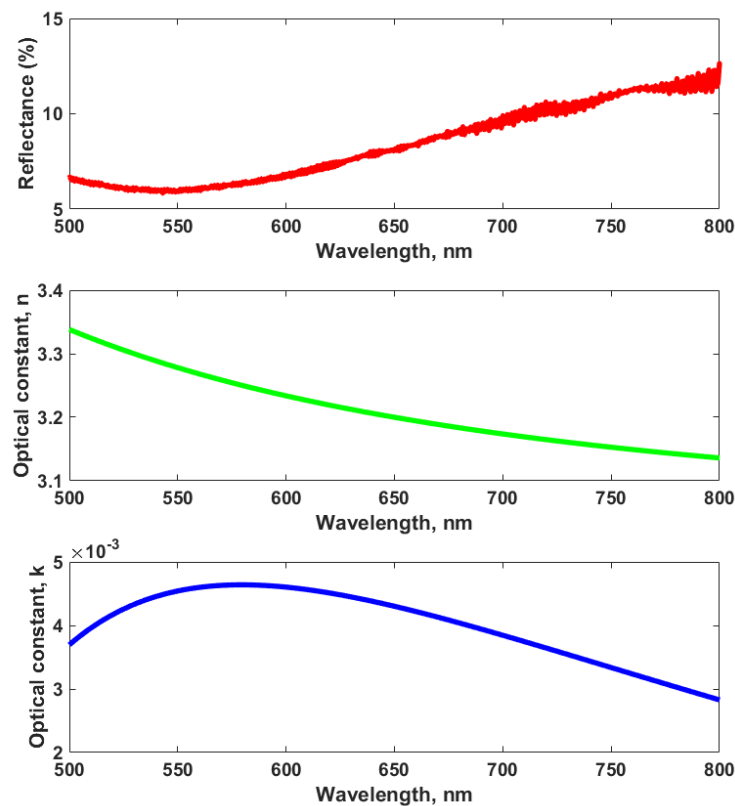
Figure 51. Reflectance spectrum and optical constants of monolayer $Ca_2NaNb_4O_{13}$ containing ITO-PET substrate.

The initial analysis was conducted for the monolayer nanofilm on the ITO-PET substrate. As indicated in Figure 51, the procedure began with measuring reflectance, then proceed to calculate the optical constants 'n' for refractive index and 'k' for another optical constant. The optimal compatibility of the reflectance was measured at 0.96. The fact that this value is close to 1 indicates that the chosen model is the optimal one. Using this model, the thickness of the nanofilm at a 632.8 nm wavelength was determined to be 2.5 nm, with 'n' at 3.2 and 'k' at 0.0044. The reflectance at this wavelength was also recorded at 7%, attributed to the transparent nature of the ITO-PET substrate. The thickness of nanofilm matches that of $Ca_2NaNb_4O_{13}$ nanosheets, indicating that the refractive indices are characteristic of the material (Li et al., 2017). Moreover, similar optical modeling was used to analyze spectral reflectance on 10-layer nanofilm-deposited ITO-PET substrates.
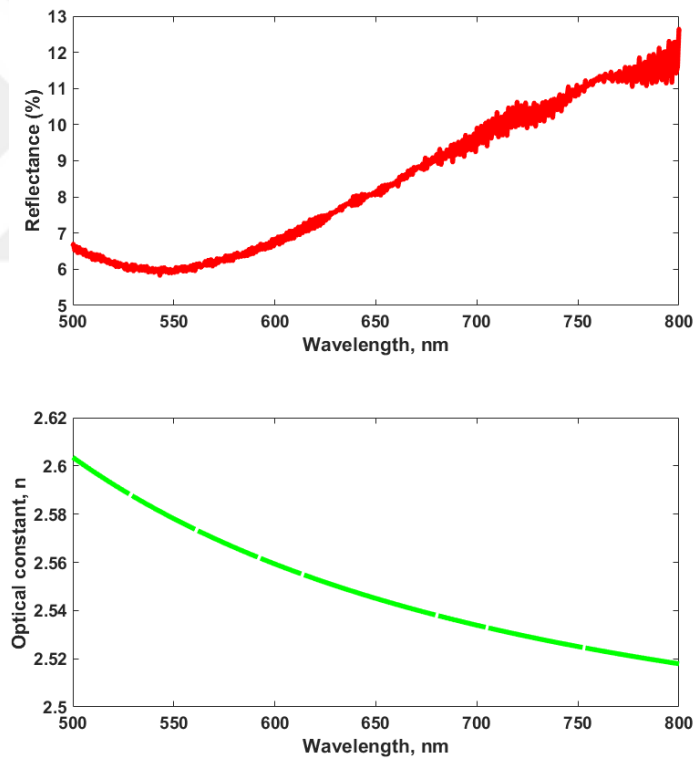
Figure 52. Reflectance spectrum and optical constants of ITO-PET/Sample 1.

In the reflectance analysis presented in Figure 52, the thickness of the ITO-PET/Sample 1 was measured to be 24.8 nm, 'n' at 2.55, and the 'k' value at 0 with a reflectance value of 7% at a wavelength of 632.8 nm. This analysis also revealed that the compatibility for the chosen optical modeling aligns with previously analyzed

monolayer ITO-PET substrate in Figure 51. Moreover, the obtained nanofilm thickness is consistent with the literature, showing agreement with the thickness of 10-layer nanofilms (Li et al., 2017). The 'n' optical constant measured in this analysis can be described as specific to $Ca_2NaNb_4O_{13}$ nanosheets. Due to inability to determine 'k' optical constant, reflectance analyses were also extended to other ITO-PET substrates deposited with 10-layer nanofilms.
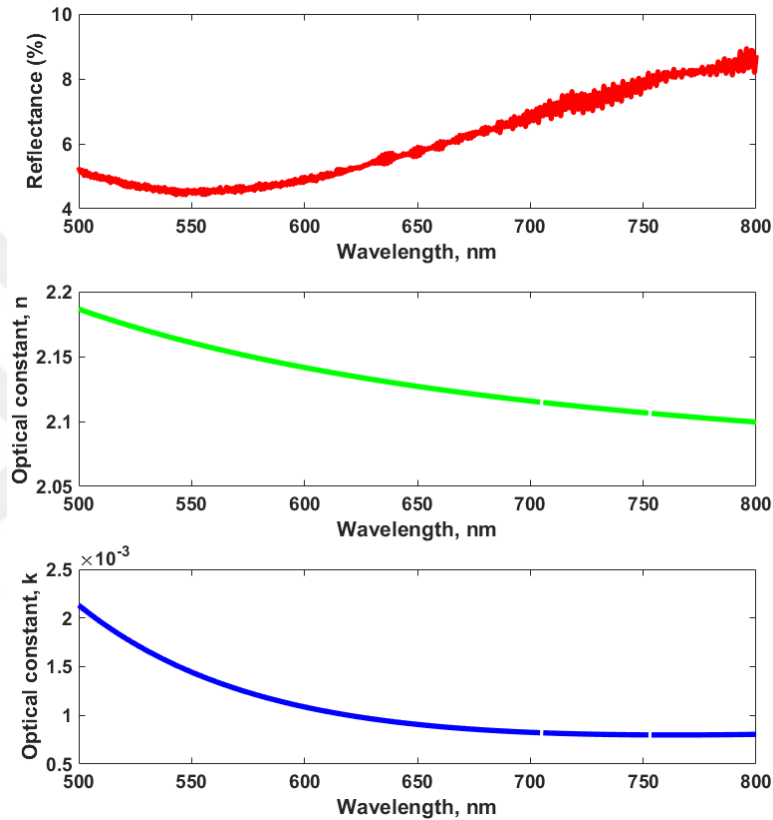
Figure 53. Reflectance spectrum and optical constants of ITO-PET/Sample 2.

Figure 53 presents the reflectance analysis of ITO-PET/Sample 2, where the compatibility of the model was found to be 0.95. The thickness of 10-layer nanofilm on ITO-PET substrate was 24.85 nm, with an 'n' value of 2.13 and 'k' value of 0.0010, and reflectance was 5% at a 632.8 nm wavelength. The thickness of the nanofilm in this analysis being close to 24 nm, suggests that the calculated optical constants are specific to the material. Furthermore, the inability to calculate the optical constant 'k' for ITO-PET/Sample 1 is due to its 'k' value being extremely close to zero.
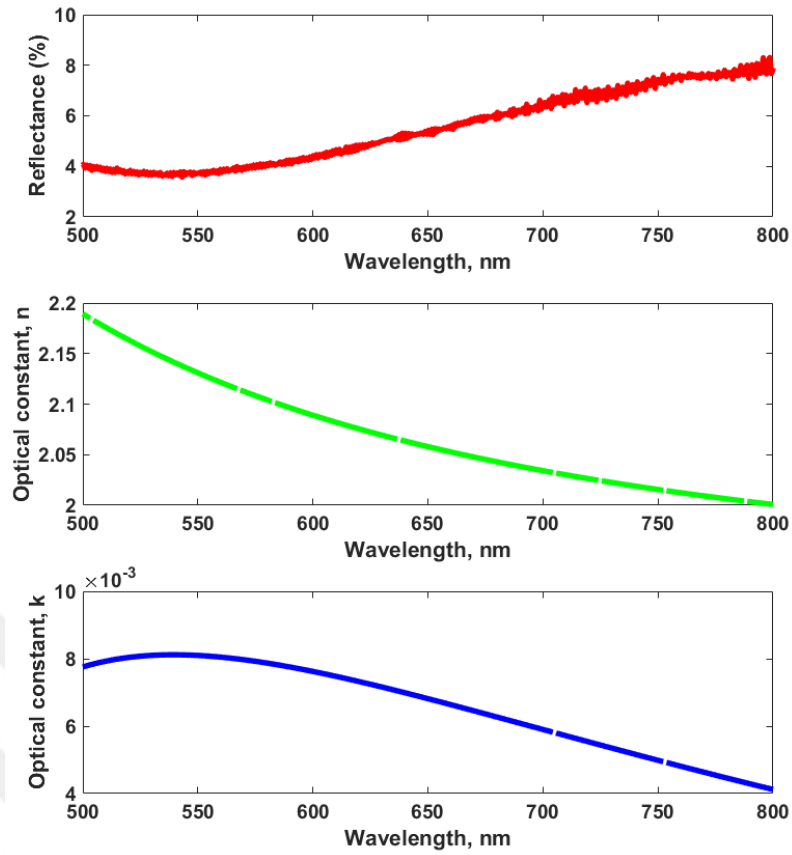
Figure 54. Reflectance spectrum and optical constants of ITO-PET/Sample 3.

The reflectance analysis of ITO-PET/Sample 3 is presented in Figure 54. Similar to ITO-PET/Sample 2, the optical modeling of ITO-PET/Sample 3 exhibited a compatibility of 0.95. The thickness of the 10-layer nanofilms at a 632.8 nm wavelength is measured at 20.02 nm, with 'n' at 2.07 and 'k' at 0.0071, leading to a reflectance of 4.6%. Notably, 'k' value for ITO-PET/Sample 3 is the highest among all the samples analyzed.

The reflectance analyses indicate that for ITO-PET samples deposited with 10-layer nanofilms, the most effective optical modeling at a wavelength of 632.8 nm was achieved. The optical constants at this wavelength were determined, with 'n' values ranging from 2 to 3 and 'k' values fluctuating between 0 and 0.01.

3.5.3. Electrical analysis of capacitors produced in different sizes
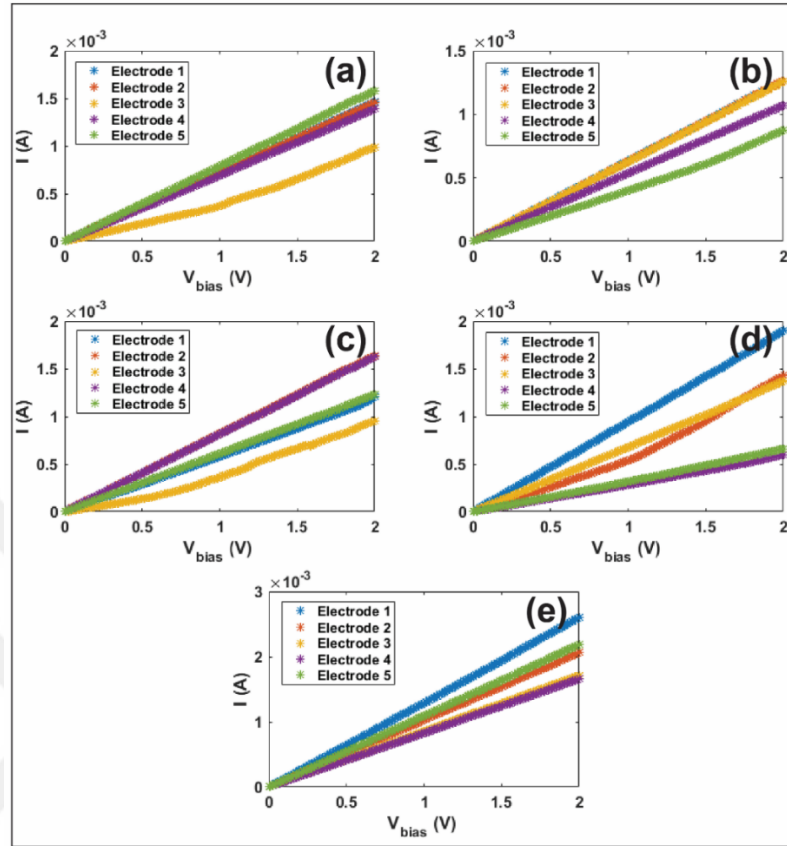
Figure 55. Current (I)-Voltage (V_{bias}) graphs obtained for 10-layer nanofilm-deposited ITO-PET/Sample 4, (a) 75 x 75 μm^2, (b) 100 x 100 μm^2, (c) 150 x 150 μm^2, (d) 200 x 200 μm^2, and 250 x 250 μm^2 electrodes.

Figure 55 (a) shows the I-V measurements of the 75 x 75 μm^2 electrodes for ITO-PET/Sample 4. Top contact measurements were taken from five distinct 75 x 75 μm^2 electrodes. Figure 55 (a) reveals that Electrode 5 in the 75 x 75 μm^2 electrode set exhibits the least current conduction, with a minimum current of 1.81 x 10^{-4} A at 0.5 V. Subsequent I-V measurements on 100 x 100 μm^2 electrodes showed the lowest current at 0.5 V as 1.98 x 10^{-4} A. The I-V graph in Figure 55 (b) indicates no linear progression in the measurements but shows greater current results compared to smaller electrodes. When comparing the 75 and 100 μm square electrodes, it was observed that current conduction remains nearly the same despite increasing electrode size. For the 150 μm square Electrode 3, the lowest current recorded at 0.5 V was 1.36 x 10^{-4} A. I-V measurements on 200 μm square electrodes showed the lowest current at 0.5 V

to be 1.39 x 10^{-4} A, as seen in Figure 55 (d). Figure 55 (e) details the current conduction for 250 μm square electrodes, with the lowest current at 4.12 x 10^{-4} A, identified as the highest current conduction electrode for 10-layer ITO-PET/Sample 4. Moreover, the sample displayed minimal variance in current conduction across electrodes of different sizes.
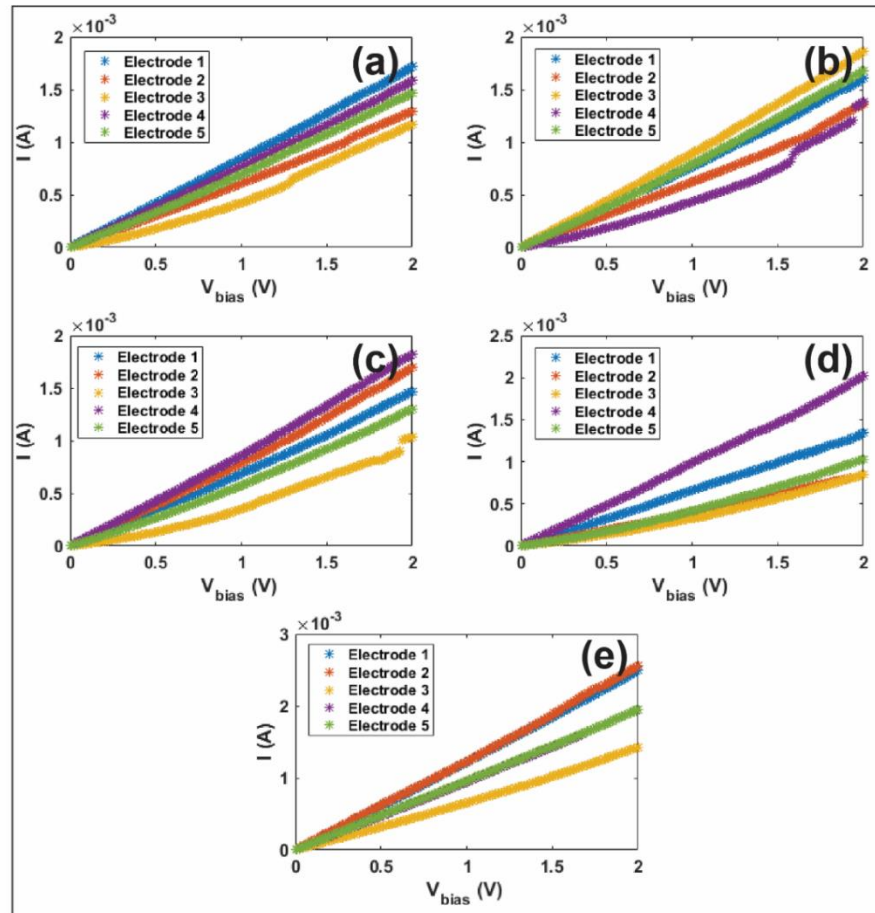
Figure 56. Current (I)-Voltage (V$_{bias}$) graphs obtained for 15-layer nanofilm – deposited ITO-PET/Sample 5, (a) 75 x 75 μm^2, (b) 100 x 100 μm^2, (c) 150 x 150 μm^2, (d) 200 x 200 μm^2, and 250 x 250 μm^2 electrodes.

Figure 56 (a) presents the I -V measurements for the 75 x 75 μm^2 electrodes of ITO-PET/Sample 5. As indicated in Figure 56 (a), the lowest current for the 75 μm square electrode, at 1.76 x 10^{-4} A, was recorded with an applied voltage of 0.5 V. I-V measurements were then carried out on 100 μm square electrodes, and the lowest current conduction from these electrodes at 0.5 V was measure as 1.84 x 10^{-4} A [See in Figure 56 (b)]. For the 150 x 150 μm^2 electrodes, the smallest current conduction,

1.28 x 10^{-4} A, is recorded at 0.5 V, as indicated in Figure 56 (c). The fourth set of I-V measurements on the 200 μm square electrode, as seen in Figure 56 (d), recorded a minimum current of 1.40 x 10^{-4} A. Finally, the fifth I-V measurements for ITO-PET/Sample 5, which involves the 250 μm square electrodes, is depicted in Figure 56 (e). Electrode 3, similar to the 200 μm square electrode with the lowest current conduction, recorded a current of 3.17 x 10^{-4} A at 0.5 V.
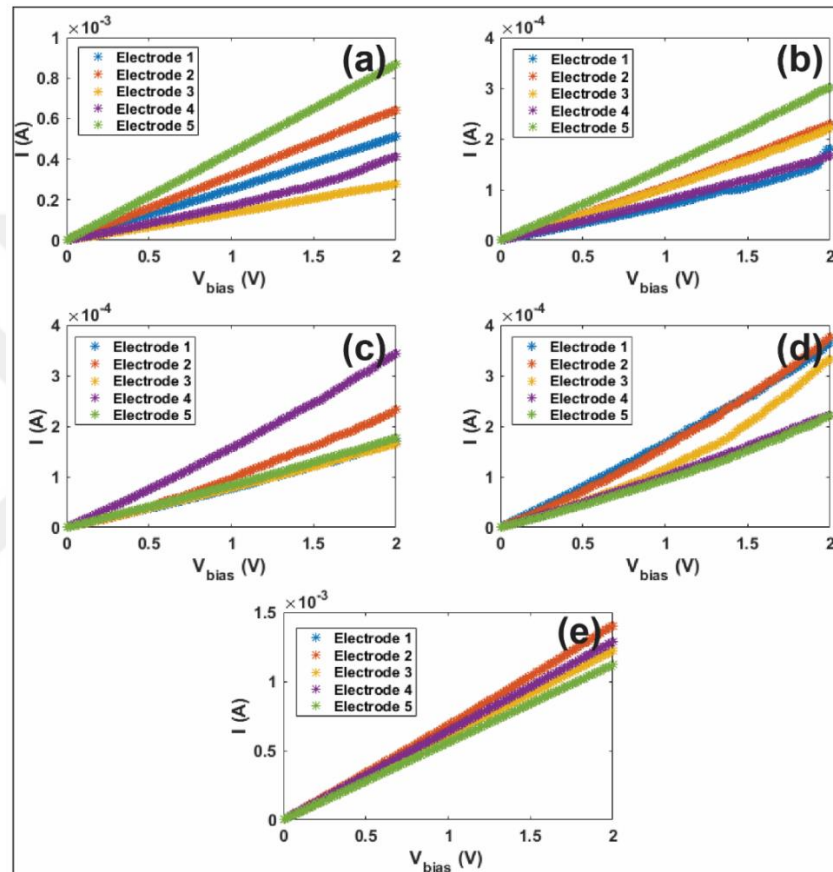
Figure 57. Current (I)-Voltage (V$_{bias}$) graphs obtained for 20-layer nanofilm – deposited ITO-PET/Sample 6, (a) 75 x 75 μm^2, (b) 100 x 100 μm^2, (c) 150 x 150 μm^2, (d) 200 x 200 μm^2, and 250 x 250 μm^2 electrodes.

Figure 57 (a) displays the I-V measurements for the 75 x 75 μm^2 electrodes of ITO-PET/Sample 6. Electrode 5, belonging to the 75 x 75 μm^2 electrodes, is identified in Figure 57 (a) as having the lowest current, with a conduction potential of 6.57 x 10^{-6} A at 0.5 V. Subsequent I-V measurements on 100 x 100 μm^2 electrodes revealed that Electrode 1 had the lowest current conduction at 0.5 V, with a current of 3.33 x 10^{-5} A, as indicated in Figure 57 (b). Comparing the 75 and 100 μm square electrodes, an

increase current conduction with electrode size was observed. For the 150 x 150 μm^2 electrodes, the lowest current conduction was obtained from Electrode 1 as 3.76 x 10^{-5} A at 0.5 V [See in Figure 57 (c)]. In the I-V measurements of the 150 μm square electrode, an increase in current conduction with electrode area was noted, in contrast to the smaller electrodes. The 200 μm square electrode, as seen in Figure 57 (d), also had Electrode 5 conducting the lowest current, measured at 4.41 x 10^{-5} A at 0.5 V. When comparing this with the 150 μm square electrode, a slight increase in current conduction for the 200 μm^2 size was observed, as shown in Figures 57 (c) and (d). Furthermore, Figure 57 (e) presents the I-V measurements for the 250 x 250 μm^2 electrodes of ITO-PET/Sample 6, where Electrode 5, like in the 200 μm square scenario, conducted the lowest current of 2.79 x 10^{-4} A at 0.5 V. However, there was no notable change in current conduction values despite the increased number of layers in the nanofilm.
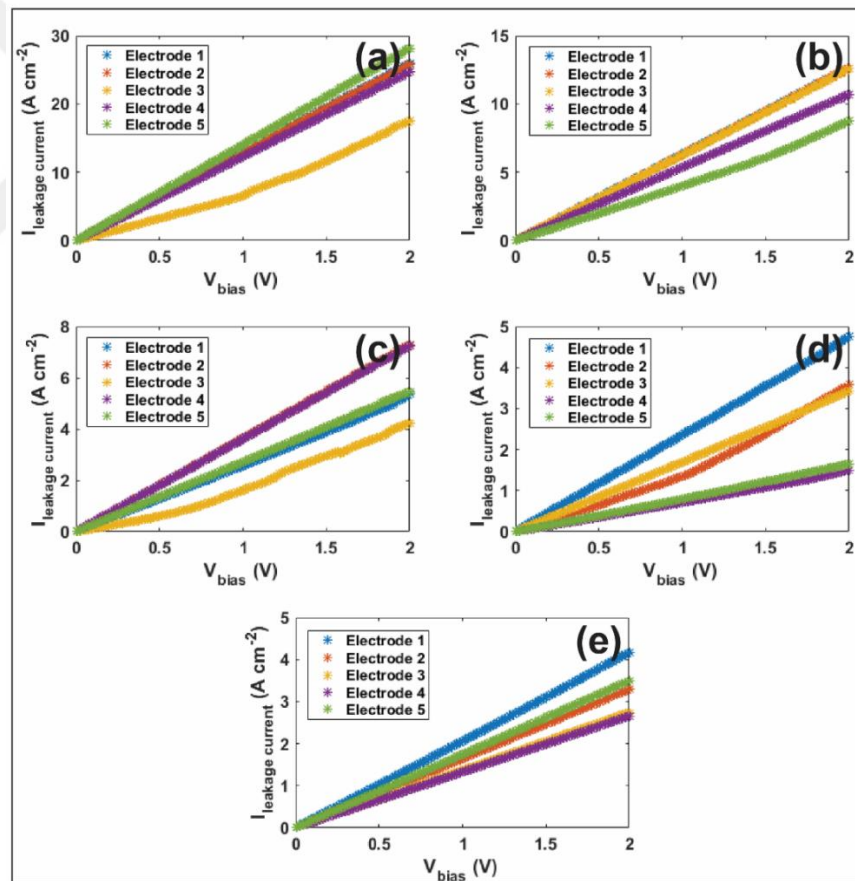
Figure 58. Leakage Current ($I_{leakage}$)-Voltage (V_{bias}) graphs obtained for 10-layer nanofilm – deposited ITO-PET/Sample 4, (a) 75 x 75 μm^2, (b) 100 x 100 μm^2, (c) 150 x 150 μm^2, (d) 200 x 200 μm^2, and 250 x 250 μm^2 electrodes.

Figure 58 (a) presents the leakage current calculations for 75 x 75 μm^2 electrodes of 10-layer nanofilm-deposited ITO-PET/Sample 4, showing a leakage current of 3.22 A/cm^2 at 0.5 V. In the literature, the leakage current of $Ca_2NaNb_4O_{13}$ nanosheets are reported to be ~10^{-9} in the same voltage range (Li et al., 2017). In this study, the leakage current was conducted on 10 x 10 μm size gold electrodes fabricated on $Ca_2NaNb_4O_{13}$ nanosheets-structured nanofilms on $SrRuO_3$ substrate. Unlike the flexible and rougher ITO-PET substrates, the $SrRuO_3$ substrate is smoother. Additionally, the use of gold for the top coat of the electrodes, instead of ITO, contributes to the differences in the leakage current values compared to those in the literature. When 0.5 V was applied to 100 μm square electrodes, the leakage current was 1.98 A/cm^2. Comparing Figures 58 (a) and (b), there is about a 1.5 times difference in the leakage currents at 0.5 V. For the 150 μm square electrodes, the leakage current at 0.5V was 0.604 A/cm^2, decreasing with larger electrode areas compared to 100 μm square electrodes. Figure 58 (d) showing the leakage current for 200 x 200 μm^2 electrodes is lower than that for smaller electrodes, measuring 0.348 A/cm^2 at 0.5 V. This value is also the half of the calculated leakage current values of the 150 x 150 μm^2 electrodes. The detailed leakage current values for 250 μm square electrodes are presented in Figure 58 (e), with the lowest leakage current was calculated at 0.5 V being 0.659 A/cm^2. The 150 x 150 μm^2 electrodes were identified as having the lowest leakage current among all the electrodes produced on ITO-PET/Sample 4.
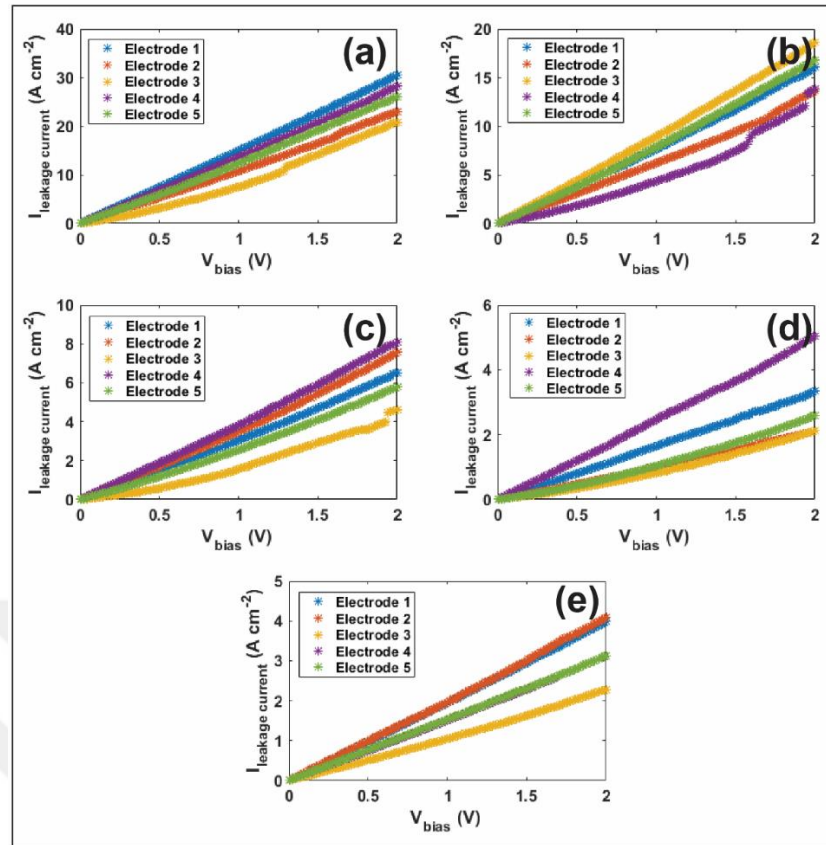
Figure 59. Leakage Current ($I_{leakage}$)-Voltage (V_{bias}) graphs obtained for 15-layer nanofilm – deposited ITO-PET/Sample 4, (a) 75 x 75 μm², (b) 100 x 100 μm², (c) 150 x 150 μm², (d) 200 x 200 μm², and 250 x 250 μm² electrodes.

Figure 59 (a) presents the calculated leakage current values for 75 x 75 μm² electrodes fabricated on 15-layer nanofilm-deposited ITO-PET/Sample 5, showing a leakage current of 3.13 A/cm² at 0.5 V. Leakage current decreased to 1.84 A/cm² for 100 x 100 μm² electrodes at the same voltage, as indicated in Figure 59 (b). A comparison between these results and those from 10-layer nanofilm-deposited ITO-PET/Sample 4 reveals a similar 1.5-fold difference in leakage current. For 150 μm square electrodes, the leakage current was lower, at 0.569 A/cm² [See in Figure 59 (c)]. This trend continued with 200 x 200 μm² electrodes, where the leakage current further decrease to 0.350 A/cm², as indicated in Figure 59 (d). This value was nearly half that of the 150 x 150 μm² electrodes, aligning findings from ITO-PET/Sample 4. Detailed analysis of the 250 μm square electrodes, shown in Figure 59 (e), indicates the lowest calculated leakage current was 0.507 A/cm² at 0.5 V. Furthermore, the 150 μm square electrodes exhibited the lowest leakage current overall. Comparing 15-layer

ITO-PET/Sample 5 with 10-layer ITO-PET/Sample 4, it is apparent that increasing the number of layers leads to reduced leakage current in 150 x 150 μm² electrodes.
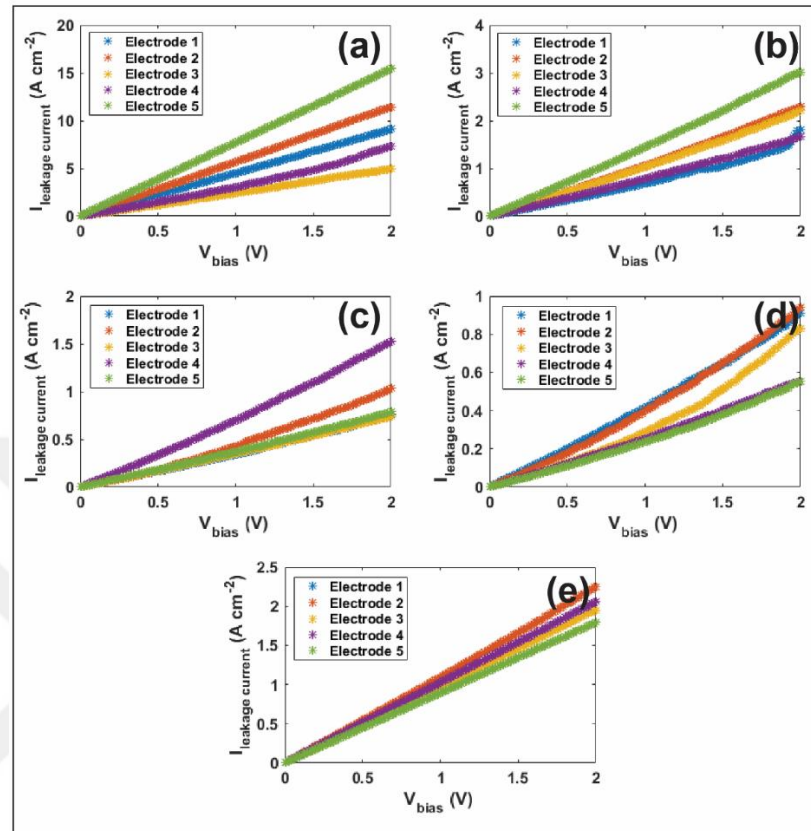
Figure 60. Leakage Current ($I_{leakage}$)-Voltage (V_{bias}) graphs obtained for 20-layer nanofilm – deposited ITO-PET/Sample 4, (a) 75 x 75 μm², (b) 100 x 100 μm², (c) 150 x 150 μm², (d) 200 x 200 μm², and 250 x 250 μm² electrodes.

The leakage current values calculated for 75 x 75 μm² electrodes of 20-layer nanofilm-deposited ITO-PET/Sample 6 are indicated in Figure 60 (a), where a current leakage of 1.17 A/cm² was recorded at 0.5 V. Leakage current values decreased to 0.333 A/cm² for 100 x 100 μm² electrodes and further to 0.167 A/cm² for 150 μm square electrodes under the same voltage, as shown in Figure 60 (b) and (c). This trend continued with larger electrodes of 200 x 200 μm² and 250 x 250 μm², where leakage current further decreased to 0.110 A/cm² for 200 μm square electrodes [See in Figure 60 (d)] and 0.446 A/cm² for 250 μm square electrodes [See in Figure 60 (e)]. The 150 μm square electrodes exhibited the lowest leakage current, and when compared to 10 and 15-layer ITO-PET samples, the 20-layer ITO-PET/Sample 6 had significantly

lower leakage currents, about five times less than the other samples. This result indicates that increasing the number of layers leads to reduced leakage currents.

As show in the I-V graphs, electrode area plays a crucial role in determining leakage current values. For capacitor applications, 75 x 75 μm^2 electrodes ITO-PET substrates are determined to be the optimal. Moreover, 20-layer ITO-PET/Sample 6 was found to have the lowest leakage current among the 10, 15-layer samples, affirming that more layers result in lower leakage currents.
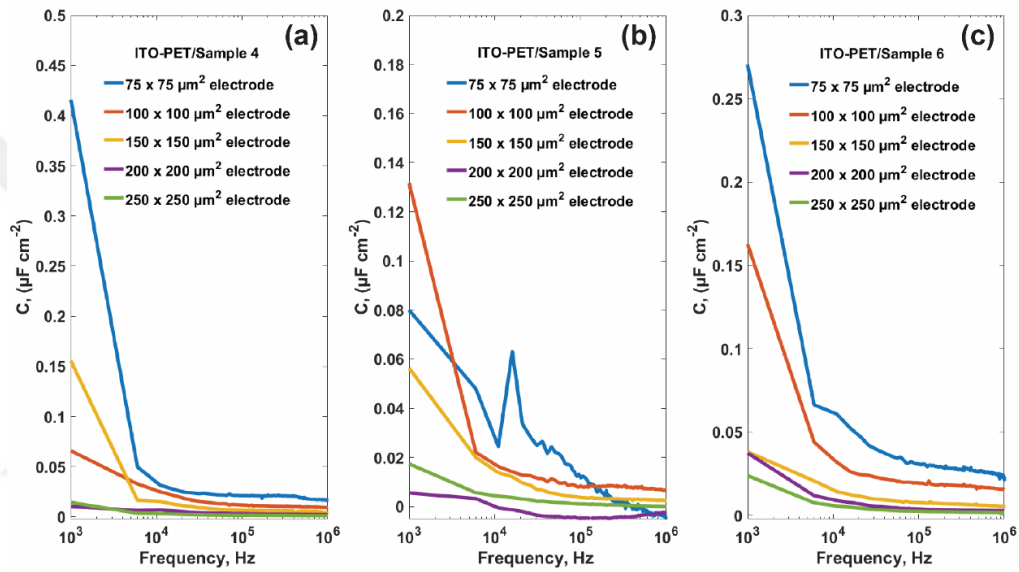
Figure 61. Frequency-dependent capacitance values of (a) 10-layer nanofilm-deposited ITO-PET/Sample 4, (b) 15-layer nanofilm-deposited ITO-PET/Sample 5, and (c) 20-layer nanofilm-deposited ITO-PET/Sample 6.

Figure 61 (a) presents the frequency-dependent capacitance values for 10-layer ITO-PET/Sample 4. The 75 x 75 μm^2 electrodes exhibited the highest capacitance at 1 kHz, with a value of 0.42 $\mu F/cm^2$. The 100 x 100 μm^2 electrodes showed a capacitance of 0.066 $\mu F/cm^2$ at 1 kHz, which then leveled off at 0.021 $\mu F/cm^2$ up to 1 MHz. The 150 μm square electrodes had a slightly higher capacitance of 0.16 $\mu F/cm^2$ at 1 kHz compared to the 100 μm square electrodes. From 10 kHz to 1 MHz, the capacitance values for these electrodes remained constant at around 0.017 $\mu F/cm^2$. The 200 x 200 μm^2 electrodes maintained a constant frequency-dependent capacitance of 0.010 $\mu F/cm^2$ from 1 kHz to 1 MHz. According to Figure 61 (a), all electrodes except

the 200 μm square electrodes experienced sharp decreases in capacitance starting from 1 kHz. The 250 μm square electrodes, while having smaller decreases in capacitance than the others, showed a value of 0.023 μF/cm². The 200 x 200 μm² electrodes were identified as having the lowest frequency-dependent capacitance. Therefore, 75 x 75 μm² electrodes were chosen for dielectric measurements.

The frequency-dependent capacitance values for 15-layer ITO-PET/Sample 5 is shown in Figure 61 (b), which the 100 x 100 μm² electrodes exhibited the highest capacitance at 1 kHz, with a value of 0.13 μF/cm². The capacitance for the 75 x 75 μm² electrodes was recorded as 0.080 μF/cm² at 1 kHz, which later decreased, settling at 0.063 μF/cm². Similar ITO-PET/Sample 4, the capacitance values remained steady at about 0.028 μF/cm² between 10 kHz and 1 MHz. For the 200 x 200 μm² electrodes, the capacitance at 1 kHz was measured as 0.0056 μF/cm². As shown in Figure 61 (b), all electrodes except for the 75 μm square electrodes experienced sudden drops in capacitance starting from 1 kHz. The 250 μm square electrodes, while showing similar decreases in capacitance compared to the others, had a capacitance of 0.027 μF/cm². Therefore, the lowest frequency-dependent capacitance was recorded in the 200 x 200 μm² electrodes. Additionally, a comparison of the capacitance values of 10-layer ITO-PET/Sample 4 and 15-layer ITO-PET/Sample 5 revealed that the highest capacitance for ITO-PET/Sample 4 was 0.42 μF/cm², while it was 0.13 μF/cm² for ITO-PET/Sample 5.

Figure 61 (c) details the frequency-dependent capacitance values for 20-layer ITO-PET/Sample 6. The 75 x 75 μm² electrodes demonstrated the highest capacitance at 1 kHz, with a value of 0.27 μF/cm². At the same frequency, 100 x 100 μm² electrodes showed a capacitance of 0.16 μF/cm², which subsequently decreased to 0.026 μF/cm² and stabilized until 1 MHz. The 150 μm square electrodes recorded a capacitance of 0.038 μF/cm² at 1 kHz. Similar to ITO-PET/Sample 4 and 5, the capacitance values for these electrodes remained constant at around 0.0080 μF/cm² from 10 kHz to 1 MHz. For the 200 x 200 μm² electrodes, the capacitance at 1 kHz was 0.037 μF/cm². Notably, the capacitance values for the 150 and 200 μm square electrodes were closely aligned at 1 kHz for ITO-PET/Sample 6. According to Figure 61 (c), all electrodes except the 75 μm square electrodes experienced an abrupt drop in capacitance starting from 1 kHz. The 250 x 250 μm² electrodes, while showing smaller decreases in

capacitance compared to the other electrodes, had the lowest capacitance of 0.024 $\mu F/cm^2$.

Wang et al. (2014) conducted a study in which they developed a capacitor structured with $Ru_{0.95}O_{20.02}^-$ and $Ca_2Nb_3O_{10}^-$ nanosheets and fabricated Au electrodes on quartz glass substrates before conducting dielectric measurements. They found that the dielectric constants ranged from 130 to 150 at 1 kHz. In this thesis, nanofilms structured with $Ca_2NaNb_4O_{13}$ nanosheets were deposited on ITO-PET substrates and patterned with optical lithography, followed by the deposition of 75 nm ITO to fabricate electrodes of various sizes. Working with these flexible and rougher substrates led to an expectation of lower frequency-dependent capacitance in the produced capacitors. However, since the results did not align with the literature, an increase in the nanofilm layer thickness was undertaken, as previously mentioned.
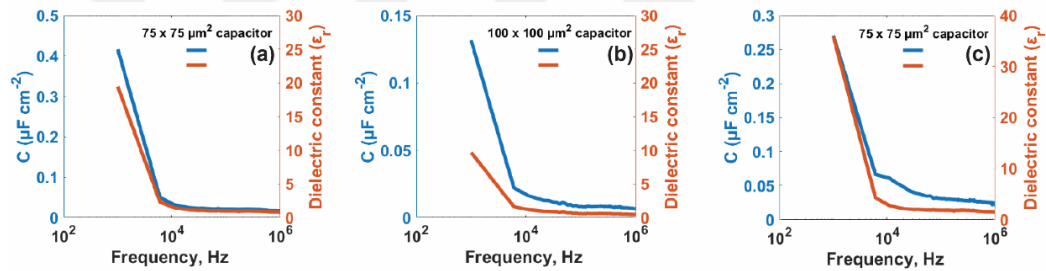
Figure 62. Frequency-dependent capacitance values and dielectric constants (ε_r) of (a) 75 x 75 μm^2 electrodes of ITO-PET/Sample 4, (b) 100 x 100 μm^2 electrodes of ITO-PET/Sample 5, and (c) 75 x 75 μm^2 electrodes of ITO-PET/Sample 6.

To calculate dielectric constants, nanofilm thicknesses listed in Table 5 were used. Figure 62 (a) shows the impact of frequency-dependent capacitance (on the left y-axis) on the dielectric constant (on the right y-axis) for 75 x 75 μm^2 ITO electrodes on 10-layer ITO-PET/Sample 4. At 1 kHz, the dielectric constant for the 75 x 75 μm^2 electrode was calculated as 19.41. Conversely, the highest capacitance values for 15-layer ITO-PET/Sample 5 were recorded at 100 x 100 μm^2 electrodes, as shown in Figure 61 (b). Thus, the dielectric constant for these electrodes, using the nanofilm thickness of 65.140 nm, was calculated to be 9.683 at 1 kHz, as seen in Figure 62 (b). Lastly, Figure 62 (b) presents the frequency-dependent capacitance and dielectric

constant values for 20-layer ITO-PET/Sample 6, whit the dielectric constant at 1 kHz for 75 x 75 µm² electrodes calculated as 35.88.

In a comparison between 20-layer ITO-PET/Sample 6 and 10-layer ITO-PET/Sample 4, the highest frequency-dependent capacitance values were observed in the 75 µm square electrodes. The capacitance value for 10-layer ITO-PET/Sample 4 was found to be about 1.5 times greater than that of 20-layer ITO-PET/Sample 6. However, 20-layer ITO-PET/Sample 6 exhibited a dielectric constant of 35.88, compared to 19.41 for ITO-PET/Sample 4. This suggests that an increase in number of layers leads to higher dielectric constants with lower capacitance values.

3.5.4. Bending strength analysis of capacitors produced in different sizes

Bending strength analysis were carried out by compressing the ITO-PET samples five times in the same direction and by the same amount.
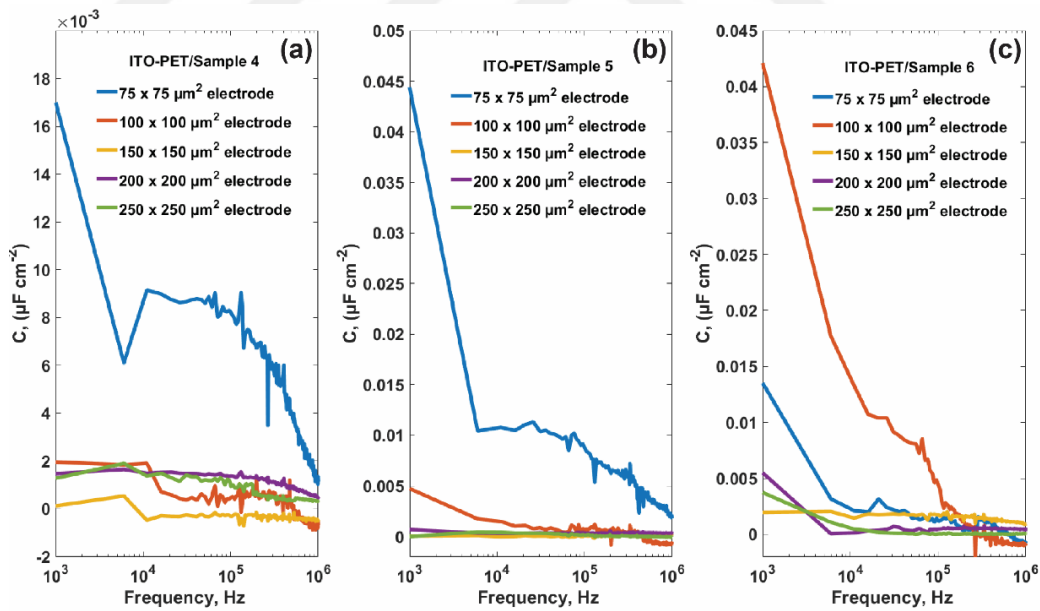
Figure 63. Frequency-dependent capacitance values obtained after bending for (a) 10-layer ITO-PET/Sample 4, (b) 15-layer ITO-PET/Sample 5, and (c) 20-layer ITO-PET/Sample 6.

After bending, the frequency-dependent capacitance at 1 kHz for 10-layer ITO-PET/Sample 4 is measured as follows: 0.017 µF/cm² for the 75 x 75 µm² electrode,

0.0020 µF/cm^2 for the 100 x 100 µm^2 electrode, 0.00012 µF/cm^2 for the 150 x 150 µm^2 electrode, 0.0015 µF/cm^2 for the 200 x 200 µm^2 electrode, and 0.0013 µF/cm^2 for the 250 x 250 µm^2 electrode [See in Figure 63 (a)]. Specifically, the capacitance for the 75 µm square electrodes reduced from 0.017 µF/cm^2 to 0.0061 µF/cm^2. The 100 µm square electrode's capacitance decreased from 0.0020 µF/cm^2 to 0.000374 µF/cm^2 and then stabilized, as depicted in Figure 63 (a). The capacitance values for the 150, 200, and 250 µm square electrodes experienced a similar reduction, stabilizing at around 0.00044 µF/cm^2.

At 1 kHz for 15-layer ITO-PET/Sample 5, the electrodes exhibited the following frequency-dependent capacitance values: 0.044 µF/cm^2 for the 75 x 75 µm^2 electrode, 0.0047 µF/cm^2 for the 100 x 100 µm^2 electrode, 0.000059 µF/cm^2 for the 150 x 150 µm^2 electrode, 0.00068 µF/cm^2 for the 200 x 200 µm^2 electrode, and 0.000090 µF/cm^2 for the 250 x 250 µm^2 electrode [See in Figure 63 (b)]. The 75 µm square electrodes showed a decrease from 0.044 µF/cm^2 to 0.0104 µF/cm^2, eventually reaching 0.0020 µF/cm^2 at 1 MHz. The capacitance of the 100 µm square electrodes decreased from 0.0047 µF/cm^2 to 0.0015 µF/cm^2 and then stabilized, as detailed in Figure 63 (b). The capacitance changes for the 150, 200, and 250 µm square electrodes average around 0.00044 µF/cm^2 and remained constant. After bending, a comparison of 15-layer ITO-PET/Sample 5 with 10-layer ITO-PET/Sample 4 revealed that the capacitance value for the 15-layer was about 2.5 times greater than that of the 10-layer sample, demonstrating an increase in frequency-dependent capacitance values with the deposition of more layers on ITO-PET substrates.

Figure 63 (c) presents the frequency-dependent capacitance values after bending for the 20-layer ITO-PET/Sample 6. The capacitance values at 1 kHz are as follows: 0.014 µF/cm^2 for the 75 x 75 µm^2 electrode, 0.042 µF/cm^2 for the 100 x 100 µm^2 electrode, 0.020 µF/cm^2 for the 150 x 150 µm^2 electrode, 0.0055 µF/cm^2 for the 200 x 200 µm^2 electrode, and 0.0037 µF/cm^2 for the 250 x 250 µm^2 electrode. All the electrodes for ITO-PET/Sample 6 experienced a decrease in capacitance. Specifically, the 75 µm square electrodes saw a decrease from 0.014 µF/cm^2 to 0.0021 µF/cm^2, remaining constant until 1 MHz. The capacitance of the 100 µm square electrodes decreased from 0.042 µF/cm^2 to 0.0029 µF/cm^2 starting from 1 kHz to 1 MHz, as seen in Figure 63 (c). The capacitance values for the 150 µm square electrodes stabilized at

0.0014 µF/cm^2, while those for the 200 µm square electrodes reduced from 0.0055 µF/cm^2 to 0.000048 µF/cm^2 and then remained constant. The 250 µm square electrodes started at 0.0037 µF/cm^2 and decreased to 0.00032 µF/cm^2, remaining constant until 1 MHz. A comparison of 20-layer ITO-PET/Sample 6 with 15-layer ITO-PET/Sample 5 showed no significant differences in the frequency-dependent capacitance values after bending, particularly for the 100 µm square electrodes.

The frequency-dependent capacitance values measured after compressing the ITO-PET samples five times in the same direction are presented in Figure 63. A comparison between capacitance values before and after bending reveals a decrease in capacitance after bending. Additionally, it has been observed that as the number of dielectric layers in the sample increases, there is a corresponding increase in the frequency-dependent capacitance values following bending strength.

3.6. Biofilm Formation on Nanofilms Composed of 2D Oxide Nanosheets on Si and ITO-PET Substrates

Biofilm formation of *E. coli* on bare Si and ITO-PET substrates and monolayer-deposited nanofilms Si-monolayer (Si-ML) and ITO-PET-monolayer (ITO-PET-ML) susbtrates were analyzed using CV staining method at a wavelenght of 595 nm. The CV staining procedure was performed using the 12-well plate, with a total of 30 wells were analyzed with triplicate experiments. This analysis was conducted using the gram-negative bacteria *E. coli* to understand the interaction of $Ca_2NaNb_4O_{13}$ nanosheets-structured monolayer nanofilms on substrates with *E. coli.*
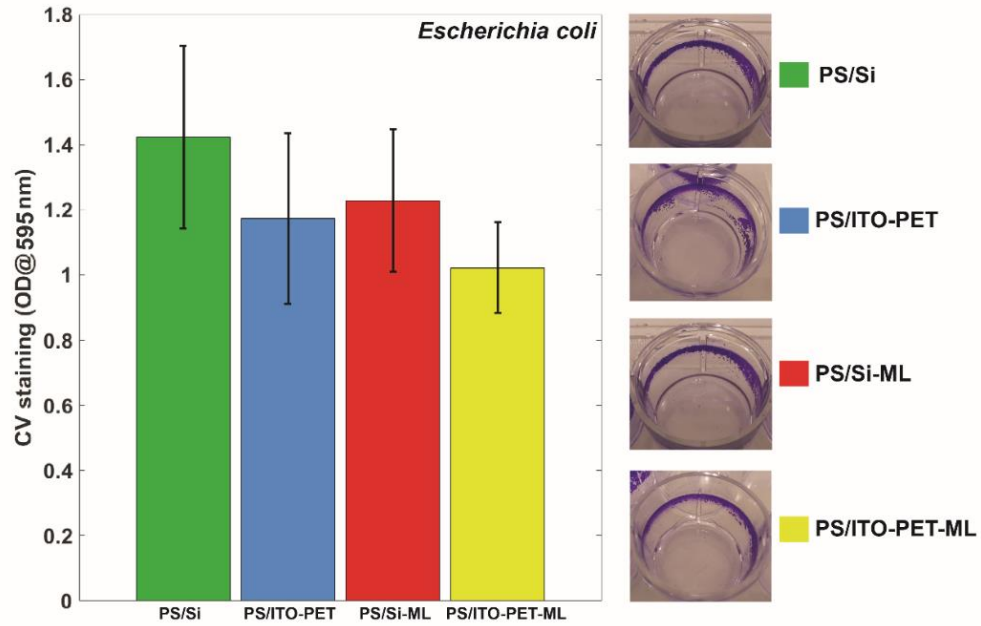
Figure 64. Biofilm formation properties of bacterial cells on polystyrene (PS) surfaces after the substrates have been removed, as determined by CV staining. PS/Si, PS/ITO-PET, PS/Si-ML and PS/ITO-PET-ML refer to the PS surfaces after Si, ITO-PET, Si-ML and ITO-PET-ML substrates have been removed, respectively.

Figure 64 presents the biofilm formation of *E. coli* cells on the surfaces of PS/Si, PS/ITO-PET, PS/Si-ML, PS/ITO-PET-ML. The term 'PS/(substrate) refers to the biofilm formed on the walls of the PS wells after the substrates have been removed. These average values were determined by adding 95% alcohol inside the wells to dissolve the PS within the wells. These were done after removing the substrates from the 12-well plates. According to the graph in Figure 64, PS/Si has the highest average at 1.4223, indicating greater biofilm formation on the walls of the wells rather than bare Si substrates. This could be attributed to the bacteria's preference for the walls of the wells over the bare substrates. Furthermore, it has been observed that less biofilm formation occurred in the well with PS/Si-ML compared to PS/Si. However, PS/ITO-PET-ML exhibited the lowest average among all tested groups. The surfaces of ITO-PET and Si became hydrophilic after nanofilm deposition, as mentioned in our previous work (Küçükcan et al., 2023), leading to greater biofilm formation on the nanofilms rather than on the walls of wells, as observed in Figure 64.
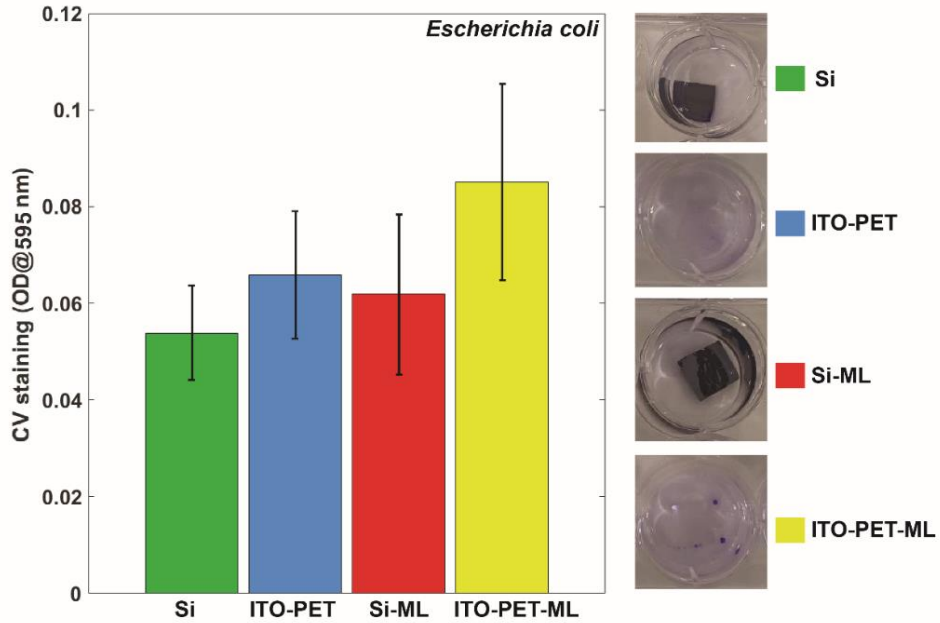
Figure 65. Biofilm formation of bacterial cells on Si, ITO-PET, Si-ML, ITO-PET-ML surfaces, as determined by CV staining.

Si, ITO-PET, Si-ML, ITO-PET-ML substrates were removed from PS wells and placed into another 12-well plate to dissolve the CV present on the substrates' surfaces using 95% alcohol. As shown in Figure 65, ITO-PET-ML had the highest average value at 0.0851 among all the tested substrates. This higher value is due to its hydrophilic nature after nanofilm deposition, leading to increased biofilm formation compared to bare ITO-PET substrates. Moreover, ITO-PET substrates are rougher and their adhesion was determined to be stronger in water environment compared to Si substrates, and nanofilm deposition on these substrates makes them more hydrophilic, resulting in greater bacterial adhesion than on bare substrates (Yadav et al., 2017; Küçükcan et al., 2023).

According to the CV staining results presented in Figure 64 and 65, greater biofilm formation was observed on the monolayer nanofilm-deposited ITO-PET-ML and on PS/Si (PS walls after Si was removed). For ITO-PET-ML, the biofilm formation was significantly influenced by the rough and hydrophilic surface of the nanofilm-deposited substrate. In contrast, PS/Si was more influenced by the hydrophobic surface of bare Si substrate, which led to an increased interaction of bacteria on the walls of the wells. In future studies, another strain of *E. coli* and gram-positive bacteria will be

cultivated in the 12-well plates with both bare and monolayer nanofilm-deposited substrates. Additionally, growth analysis will be performed at a wavelength of 600 nm with higher experimental repetitions. For more accurate data analysis, statistical comparisons will be performed as well. This preliminary work aims to provide insight into the interaction of 2D oxide nanosheets with bacteria and other materials.

CHAPTER 4: CONCLUSION

In this thesis, DJ-type $KCa_2NaNb_4O_{13}$ layered materials were successfully synthesized by the solid-state calcination method at 1200 °C with a heating rate of 10 °C/ min, which resulted in crystalline materials with an orthorhombic structure. The layered materials were treated with various acid solutions for protonation process, with the optimal condition was treatment with 5 M HNO_3 solution for four days. For nanosheet production, TBAOH solutions of different concentrations were analyzed using UV/Vis absorbance spectroscopy, leading to the observation of the most effective $TBA^+:H^+$ molar ratio of 1:16. These optimal conditions allowed for the production and detection of $Ca_2NaNb_4O_{13}$ single nanosheets with a thickness of 2.4 nm and a lateral size of 3.5 μm on Si substrates using AFM. These nanosheets then deposited on ITO-PET substrates using LB deposition technique at a surface tension of 15 mN/m. This surface tension was determined ideal for creating monolayer nanofilms on the substrates. The transparency decrease of ITO-PET substrates were confirmed using UV/Vis spectroscopy. This thesis highlights the potential of LB nanofilms made of single $Ca_2NaNb_4O_{13}$ nanosheets on ITO-PET substrates as innovative dielectric materials for next-generation energy and data storage devices, including flexible, transparent capacitors and small-scale nanoarchitectures. Spectral analyses were also carried out on 10-layer ITO-PET substrates containing $Ca_2NaNb_4O_{13}$ nanosheets. The optimal optical model for 10-layer ITO-PET samples was determined at a wavelength of 632.8 nm. The findings indicated that the refractive index 'n' consistently ranged between 2 and 3, while the other optical constant 'k' varied from 0 to 0.01. LB nanofilms on ITO-PET substrates were characterized through XPS analysis, which determined the corresponding binding energies of elements present in $Ca_2NaNb_4O_{13}$ nanosheets. These findings were found to align with existing literature.

Using the LB deposition technique, $Ca_2NaNb_4O_{13}$ single oxide nanosheets were successfully deposited on ITO-PET substrates, producing nanofilms with 10, 15, and 20 layers. These deposited nanofilms then patterned using optical lithography technique and deposited with ITO thin film, resulting in the fabrication of capacitors with electrodes ranging in size from 75 x 75 μm^2 to 250 x 250 μm^2. Comprehensive

electrical analyses were performed on these electrodes of various dimensions, including I-V and frequency-dependent capacitance measurements. For the ITO-PET samples deposited with 10, 15, and 20 nanofilm layers, the study focused on understanding how the size of the ITO electrodes influenced their current transmission and capacitance values. It was determined that the 75 x 75 μm^2 electrodes in the 20-layer nanofilm-deposited capacitors exhibited the lowest current transmission. This observation indicates an increase in the number of nanofilm layers effectively reduces leakage currents and enhances dielectric constants. Additionally, the effect of bending strength to frequency-dependent capacitance on 10, 15, and 20-layer ITO-PET samples was determined. The analysis revealed a decrease in capacitance values after the capacitors subjected to uniform compression five times. Moreover, the analysis noted that increasing the number of nanofilm layers resulting in higher capacitance values after bending, indicating a correlation between nanofilm layers and bending strength.

EBL process for ITO-PET substrates was performed by fixing 10-layer ITO-PET/Sample 1 to a Si substrate to ensure smoother patterning process. However, it was observed that no patterns fabricated during the EBL process. In EBL, the typical thickness for PMMA is usually in the range of 70-80 nm. In this case, the ITO layer should be deposited thinner than PMMA for effective lift off, which is impractical using magnetron sputtering device to achieve a thickness below 70 nm. Consequently, the focus shifted other conductive substrates, including Si, Ti/Au-Si, Ti/Au-glass, and ITO-glass. These substrates were deposited $Ca_2NaNb_4O_{13}$ nanosheets-structured nanofilms using the LB method. The nanofilms were patterned using EBL and deposited 20 nm Ti/Au to fabricate electrodes in various sizes. The optimal doses for EBL were determined as 1200-1300 $\mu C/cm^2$ for Si and ITO-glass, while the dose test was 100-600 $\mu C/cm^2$ for Ti/Au-Si and Ti/Au-glass substrates. I-V measurements of capacitors fabricated using the EBL process were conducted by the c-AFM. The 5 x 5 μm^2 Ti/Au capacitors on glass substrates exhibited excellent insulating properties. The decrease in the electrode areas resulted in deformations on the patterns leading to the creation of greater leakage currents. Despite challenges related to potential inaccuracies in the Ti/Au capacitors, c-AFM measurements were effectively carried out.

The physicochemical interaction of $Ca_2NaNb_4O_{13}$ nanosheets-structured nanofilms on Si and ITO-PET substrates were studied. Contact angle measurements were conducted, and using surface thermodynamics-based mathematical modeling, the polar and apolar surface tension components of both the nanofilms and the substrates were determined. Additionally, the adhesive strength of the nanofilms to substrates was calculated using this mathematical model. It was observed that adherence was stronger in air for the Si substrates compared to ITO-PET substrates. However, in water, where polar interactions are more significant, the nanofilms exhibited stronger adherence to ITO-PET than to Si substrates. Building on this understanding of the physicochemical interactions of $Ca_2NaNb_4O_{13}$ nanosheets-structured nanofilms, the interaction of these nanofilms with bacteria was studied using the CV staining method. The study revealed significant bacterial biofilm formation on monolayer nanofilm-deposited ITO-PET substrates, due to their hydrophilic nature post-nanofilm-deposition. As expected, in aqueous environments like bacterial cultures, bacteria showed greater adhesion to the hydrophilic monolayer nanofilm-deposited ITO-PET compared to Si substrates.

REFERENCES

Akatsuka, K., Haga, M. A., Ebina, Y., Osada, M., Fukuda, K. and Sasaki, T. (2009) *Construction of Highly Ordered Lamellar Nanostructures Through Langmuir-Blodgett Deposition of Molecularly Thin Titania Nanosheets Tens of Micrometers Wide and Their Excellent Dielectric Properties*. ACS Nano, Vol. 3(5), pp. 1097–1106.

Altissimo, M. (2010) *E-Beam Lithography for Micro-/Nanofabrication*. Biomicrofluidics, Vol. 4(2), 026503.

Atuchin, V. V., Kalabin, I. E., Kesler, V. G. and Pervukhina, N. V. (2005) *Nb 3d And O 1s Core Levels and Chemical Bonding in Niobates*. Journal of Electron Spectroscopy and Related Phenomena, Vol. 142(2), pp. 129–134.

Baba, M., Sano, T., Iguchi, N., Iida, K., Sakamoto, T. and Kawaura, H. (2003) *DNA Size Separation Using Artificially Nanostructured Matrix*. Applied Physics Letters, Vol. 83(7), pp. 1468–1470.

Chawda, N., Basu, M., Majumdar, D., Poddar, R., Mahapatra, S. K. and Banerjee, I. (2019) *Engineering of Gadolinium-Decorated Graphene Oxide Nanosheets for Multimodal Bioimaging and Drug Delivery*. ACS Omega, Vol. 4(7), pp. 12470–12479.

Chang, C. W., Nurpratiwi, A. A. and Su, Y. H. (2022) *A Comparison Study of Molten-Salt and Solid-State Method for The Photoelectrochemical Water Splitting Performance of Dion-Jacobson Layers* perovskite $Ca_2Na_{n-3}Nb_nO_{3n+1}^-$ *(n= 4, 5, and 6) nanosheets.* International Journal of Hydrogen Energy, Vol. 47(96), pp. 40573–40581.

Chen, B., Yang, H., Zhao, L., Miao, J., Xu, B., Qiu, X.G., Zhao, B.R., Qi, X.Y. and Duan, X.F. (2004) *Thickness and Dielectric Constant of Dead Layer in Pt/(Ba$_{0.7}$Sr$_{0.3}$) TiO$_3$/YBa$_2$Cu$_3$O$_{7-x}$ Capacitor*. Applied Physics Letters, Vol. 84(4), pp. 583–585.

Chen, L., Ngo, D., Luo, J., Gong, Y., Xiao, C., He, X., Yu, B., Qian, L. and Kim, S.H. (2019) *Dependence of Water Adsorption on The Surface Structure of Silicon Wafers Aged Under Different Environmental Conditions*. Physical Chemistry Chemical Physics, Royal Society of Chemistry, Vol. 21(47), pp. 26041–26048.

Chhowalla, M., Shin, H.S., Eda, G., Li, L.J., Loh, K.P. and Zhang, H. (2013) *The Chemistry of Two-Dimensional Layered Transition Metal Dichalcogenide Nanosheets*. Nature chemistry, Vol. 5(4), pp. 263–275.

Chiu, G.L.T. and Shaw, J.M. (1997) *Optical Lithography: Introduction*. IBM Journal of Research and Development, Vol. 41(1–2), pp. 3–6.

Choi, W., Choudhary, N., Han, G.H., Park, J., Akinwande, D. and Lee, Y.H. (2017) *Recent Development of Two-Dimensional Transition Metal Dichalcogenides and Their Applications*. Materials Today, Vol. 20(3), pp. 116–130.

Choudhary, P. and Das, S.K. (2019) *Bio-Reduced Graphene Oxide as a Nanoscale Antimicrobial Coating for Medical Devices*. ACS Omega, Vol. 4(1), pp. 387–397.

Comyn, J. (2021) *What are adhesives and sealants and how do they work?* 2nd edition. Adhesive Bonding, Cambridge: Woodhead Publishing, pp. 41-78.

Dang, M.T., Lefebvre, J. and Wuest, J.D. (2015) *Recycling Indium Tin Oxide (ITO) Electrodes Used in Thin-Film Devices with Adjacent Hole-Transport Layers of Metal Oxides*. ACS Sustainable Chemistry and Engineering, Vol. 3(12), pp. 3373–3381.

DeRose, G.A., Zhu, L., Poon, J.K., Yariv, A. and Scherer, A. (2008) *Periodic Sub-Wavelength Electron Beam Lithography Defined Photonic Crystals for Mode Control in Semiconductor Lasers*. Microelectronic Engineering, Vol. 85(5–6), pp. 758–760.

Ding, J., Hong, B., Luo, Z., Sun, S., Bao, J. and Gao, C. (2014) *Mesoporous Monoclinic CaIn$_2$S$_4$ with Surface Nanostructure: An Efficient Photocatalyst for Hydrogen Production Under Visible Light*. Journal of Physical Chemistry C, Vol. 118(48), pp. 27690–27697.

Ebina, Y., Akatsuka, K., Fukuda, K. and Sasaki, T. (2012) *Synthesis and in Situ X-Ray Diffraction Characterization of Two-Dimensional Perovskite-Type Oxide Colloids with A Controlled Molecular Thickness*. Chemistry of Materials, Vol. 24(21), pp. 4201–4208.

Evangelou, E.K., Mavrou, G., Dimoulas, A. and Konofaos, N. (2007) *Rare Earth Oxides as High- K Dielectrics for Ge Based MOS Devices: An Electrical Study of Pt/Gd$_2$O$_3$/Ge Capacitors*. Solid-state electronics, Vol. 51(1), pp. 164–169.

Ewa, A Jurak, M., Gozdecka, A. and Worzakowska, M. (2017) *Interfacial Properties of PET And PET / Starch Polymers Developed by Air Plasma Processing*. Colloids and Surfaces A: Physicochemical and Engineering Aspects, Vol. 532, pp. 323–331.

Ewa, A., Gozdecka, A., Jurak, M., Przykaza, K. and Terpiłowski, K. (2018) *Wettability of Plasma Modified Glass Surface with Bioglass Layer in Polysaccharide Solution*. Colloids and Surfaces A: Physicochemical and Engineering Aspects, Vol. 551, pp. 185–194.

Gao, W., Zhu, Y., Wang, Y., Yuan, G. and Liu, J.M. (2020) *A Review of Flexible Perovskite Oxide Ferroelectric Films and Their Application*. Journal of Materiomics, Vol. 6(1), pp. 1–16.

Gates, B.D., Xu, Q., Stewart, M., Ryan, D., Willson, C.G. and Whitesides, G.M. (2005) *New Approaches to Nanofabrication: Molding, Printing, and Other Techniques.* Chemical reviews, Vol. 105(4), pp. 1171-1196.

Gordesli, F.P. and Abu-Lail, N.I. (2012) *The Role of Growth Temperature in The Adhesion and Mechanics of Pathogenic L. Monocytogenes: An AFM Study*. Langmuir, Vol. 28(2), pp. 1360–1373.

Gunay, B., Sarıyar, E., Unal, U., Karagonlar, Z.F. and Sağlam, Ö. (2021) *Upconversion Properties of Tm^{3+}-Er^{3+} Co-Doped Layered Perovskites and In-Vitro Cytotoxicity of Their Exfoliated Nanomaterials*, Colloids and Surfaces A: Physicochemical and Engineering Aspects, Vol. 612, pp. 126003.

Gunay, B., Süer, Ö., Döğer, H., Arslan, Ö., Unal, U. and Sağlam, Ö. (2022) *Synthesis of Upconverting Nanosheets Derived from Er-Yb and Tm-Yb Co-Doped Layered Perovskites and Their Layer-By-Layer Assembled Films*. Colloids And Surfaces A: Physicochemical and Engineering Aspects, Vol. 649, pp. 129502.

Günay, B., Döğer, H., Karagonlar, Z.F. and Sağlam, Ö. (2022) *Ag-Intercalation of Tm^{3+}/Er^{3+} Co-Doped Layered Perovskites and Their Exfoliated 2D Nanosheets with An Enhanced Antibiofilm and Antibacterial Activity*. Materials Today Communications, Vol. 33, pp. 104972.

Huff, H.R. and Gilmer, D.C. (2005) *High Dielectric Constant Materials*: *VLSI MOSFET Applications*. New York: Springer Science & Business Media, Vol 16.

Hung, C.M., Mai, C.L., Wu, C.C., Chen, B.H., Lu, C.H., Chu, C.C., Wang, M.C., Yang, S.D., Chen, H.C., Yeh, C.Y. and Chou, P.T. (2023) *Self-Assembled Monolayers of Bi-Functionalized Porphyrins: A Novel Class of Hole-Layer-Coordinating Perovskites and Indium Tin Oxide in Inverted Solar Cells*. Angewandte Chemie, Vol. 135(40), pp. e202309831.

Hussain, S., Javed, M.S., Ullah, N., Shaheen, A., Aslam, N., Ashraf, I., Abbas, Y., Wang, M., Liu, G. and Qiao, G. (2019) *Unique Hierarchical Mesoporous Lacro$_3$ Perovskite Oxides for Highly Efficient Electrochemical Energy Storage Applications*. Ceramics International, Vol 45(12), pp. 15164-15170.

Im, J., Auciello, O., Baumann, P.K., Streiffer, S.K., Kaufman, D.Y. and Krauss, A.R. (2000) *Composition-Control of Magnetron-Sputter-Deposited (Ba$_x$sr$_{1-x}$)Ti$_{1+y}$o$_{3+z}$ Thin Films for Voltage Tunable Devices*. Applied Physics Letters, Vol. 76(5), pp. 625-627.

Influence of Droplet Volume on Contact Angle (2016). Attension Technology Note 6, Stockholm: Biolin Scientific-Surface Science Instruments.

Jantsky, L., Okamoto, H., Thomas, M., Karen, P., Hauback, B.C., Rosseinsky, M.J. and Fjellvag, H. (2014) *Complex Magnetic Behavior in The Prsr$_3$(Fe$_{1-x}$co$_x$)$_3$O$_{10-Δ}$ N = 3 Ruddlesden-Popper- Type Solid Solution with High Valent Cobalt and Iron*. Chemistry of Materials, Vol. 26(2), pp. 886-897.

Jiang, D., Wang, T., Xu, Q., Li, D., Meng, S. and Chen, M. (2017) *Perovskite Oxide Ultrathin Nanosheets/G-C$_3$N$_4$ 2D-2D Heterojunction Photocatalysts with Significantly Enhanced Photocatalytic Activity Towards the Photodegradation of Tetracycline*. Applied Catalysis B: Environmental, Vol. 201, pp. 617-628.

Junquera, J. and Ghosez, P. (2003) *Critical Thickness for Ferroelectricity in Perovskite Ultrathin Films*. Nature, Vol. 422(6931), pp. 506–509.

Jurak, M., Ewa, A. and Terpiłowski, K. (2016) *Properties Of PEEK-Supported Films of Biological Substances Prepared by The Langmuir-Blodgett Technique*. Colloids And Surfaces A: Physicochemical and Engineering Aspects, Vol. 510, pp. 263–274.

Jurak, M., Mroczka, R., Łopucki, R. and Wiącek, A.E. (2019) *Applied Surface Science Structure and Wettability of Heterogeneous Monomolecular Films of Phospholipids with Cholesterol or Lauryl Gallate*. Applied Surface Science, Vol. 493, pp. 1021–1031.

Kerner, R.A. and Rand, B.P. (2019) *Electrochemical and Thermal Etching of Indium Tin Oxide by Solid-State Hybrid Organic-Inorganic Perovskites*. ACS Applied Energy Materials, Vol. 2(8), pp. 6097–6101.

Khan, M.S., Kim, H.J., Kim, Y.H., Ebina, Y., Sugimoto, W., Sasaki, T. and Osada, M. (2020) *Scalable Design of Two-Dimensional Oxide Nanosheets for Construction of Ultrathin Multilayer Nanocapacitor*. Small, Vol. 16(39), pp. 2003485.

Khan, M.S., Osada, M., Dong, L., Kim, Y.H., Ebina, Y. and Sasaki, T. (2020) *Rational Assembly of Two-Dimensional Perovskite Nanosheets as Building Blocks for New Ferroelectrics*. ACS Applied Materials & Interfaces, Vol. 13(1), pp. 1783-1790.

Kim, B.S., Oh, S.H., Son, S.Y., Park, K.W., Choi, D.K., Dai, Z.R. and Ohuchi, F.S. (2000) *The Effect of Interface on The Electrical Properties of (Ba,Sr)TiO$_3$ Adopting the Perovskite Electrodes*. Journal of Applied Physics, Vol. 87(9), pp. 4425-4429.

Kim, H.J., Osada, M., Ebina, Y., Sugimoto, W., Tsukagoshi, K. and Sasaki, T. (2016) *Hunting for Monolayer Oxide Nanosheets and Their Architectures*. Scientific Reports, Vol. 6(1), pp. 19402.

Kim, H. J., Osada, M., and Sasaki, T. (2016) *Advanced Capacitor Technology Based on Two-Dimensional Nanosheets*. Japanese Journal of Applied Physics, Vol. 55(11), pp. 1102A3.

Knobloch, T., Illarionov, Y.Y., Ducry, F., Schleich, C., Wachter, S., Watanabe, K., Taniguchi, T., Mueller, T., Waltl, M., Lanza, M. and Vexler, M.I. (2021) *The Performance Limits of Hexagonal Boron Nitride as An Insulator for Scaled CMOS Devices Based on Two-Dimensional Materials*. Nature Electronics, Vol. 4(2), pp. 98-108.

Knyazev, A.V., Krasheninnikova, O.V., Syrov, E.V., Kyashkin, V.M., Lelet, M.I. and Smirnova, N.N. (2019) *Thermodynamic and X-ray studies of layered perovskite KCa$_2$NaNb$_4$O$_{13}$*. The Journal of Chemical Thermodynamics, Vol. 138, pp. 255-261.

Küçükcan, B., Günay, B., Gordesli-Duatepe, F.P. and Sağlam, Ö. (2023) *Langmuir-Blodgett Deposition and Physicochemical Surface Characterization of Two-Dimensional Perovskite Nanosheets on ITO-PET Substrates*. Colloids and Surfaces A: Physicochemical and Engineering Aspects, Vol. 666, pp. 131338.

Li, B.W., Osada, M., Akatsuka, K., Ebina, Y., Ozawa, T.C. and Sasaki, T. (2011) *Solution-Based Fabrication of Perovskite Multilayers and Superlattices Using Nanosheet Process*. Japanese Journal of Applied Physics, Vol. 50(9S2), pp. 09NA10.

Li, B.W., Osada, M., Kim, Y.H., Ebina, Y., Akatsuka, K. and Sasaki, T. (2017) *Atomic Layer Engineering of High-κ Ferroelectricity in 2D Perovskites*. Journal of the American Chemical Society, Vol. 139(31), pp. 10868-10874.

Liu, S., Zeng, T.H., Hofmann, M., Burcombe, E., Wei, J., Jiang, R., Kong, J. and Chen, Y. (2011) *Antibacterial Activity of Graphite, Graphite Oxide, Graphene Oxide, and Reduced Graphene Oxide: Membrane and Oxidative Stress*. Acs Nano, 5(9), pp. 6971-6980.

Liu, Y., Wen, J., Gao, Y., Li, T., Wang, H., Yan, H., Niu, B. and Guo, R. (2018) *Antibacterial Graphene Oxide Coatings on Polymer Substrate*. Applied Surface Science, Vol. 436(2010), pp. 624–630.

Liu, Y. et al. 2018. *Highly Defective Layered Double Perovskite Oxide for Efficient Energy Storage via Reversible Pseudocapacitive Oxygen-Anion Intercalation.* Advanced Energy Materials, Vol. 8(11), pp. 1702604.

Liu, R., Feng, B., Ma, Y., Liu, H., Cui, J., Yang, D. and Yuan, H. (2020) *Synthesis of Layered-Perovskite $KCa_2Na_{n-3}Nb_nO_{3n+1}$ with Different Layer Thickness*. Materials Letters, Vol. 281, pp. 128635.

Lu, C.J., Qiao, Y., Qi, Y.J., Chen, X.Q. and Zhu, J.S. (2005) *Large Anisotropy of Ferroelectric and Dielectric Properties for $Bi_{3.15}Nd_{0.85}Ti_3O_{12}$ Thin Films Deposited on $Pt/Ti/SiO_2/Si$.* Applied Physics Letters, Vol. 87(22), pp. 1-3.

Ma, R. and Sasaki, T. (2015) *Two-Dimensional Oxide and Hydroxide Nanosheets: Controllable High-Quality Exfoliation, Molecular Assembly, And Exploration of Functionality Published as Part of The Accounts of Chemical Research Special Issue "2D Nanomaterials Beyond Graphene".* Accounts of chemical research, Vol. 48(1), pp. 136–143.

Ma, X., Jiang, D., Xiao, P., Jin, Y., Meng, S. and Chen, M. (2017) *2D/2D Heterojunctions of WO_3 Nanosheet/$K^+Ca_2Nb_3O_{10}^-$ Ultrathin Nanosheet with Improved Charge Separation Efficiency for Significantly Boosting Photocatalysis*. Catalysis Science & Technology, Vol. 7(16), pp. 3481–3491.

Madou, M.J. (2002) *Fundamentals of Microfabrication: The Science of Miniaturization.* 2nd edition. Boca Raton: CRC Press.

Majee, R., Islam, Q.A., Mondal, S. and Bhattacharyya, S. (2020*) An Electrochemically Reversible Lattice with Redox Active A-Sites of Double Perovskite Oxide Nanosheets to Reinforce Oxygen Electrocatalysis*. Chemical science, Vol. 11(37), pp. 10180-10189.

Manzeli, S., Ovchinnikov, D., Pasquier, D., Yazyev, O.V. and Kis, A. (2017) *2D Transition Metal Dichalcogenides*. Nature Reviews Materials, Vol. 2(8), pp. 1-15.

Menon, R., Patel, A., Gil, D. and Smith, H.I. (2005) *Maskless Lithography*. Materials Today, Vol. 8(2), pp. 26–33.

Moore, G.E. (1965) *Cramming More Components onto Integrated Circuits.* Electronics, Vol. 38, pp. 114–117.

Moore, G.E. (1975) *Progress in Digital Integrated Electronics*. IEDM Tech. Digest, Vol. 21, pp. 11–13.

Muramatsu, M., Akatsuka, K., Ebina, Y., Wang, K., Sasaki, T., Ishida, T., Miyake, K. and Haga, M.A. (2005) *Fabrication of Densely Packed Titania Nanosheet Films on Solid Surface by Use of Langmuir-Blodgett Deposition Method Without Amphiphilic Additives*. Langmuir, Vol. 21(14), pp. 6590–6595.

Müller, J., Polakowski, P., Mueller, S. and Mikolajick, T. (2015) *Ferroelectric Hafnium Oxide Based Materials and Devices: Assessment of Current Status and Future Prospects Ferroelectric Hafnium Oxide Based Materials and Devices*. ECS Journal of Solid State Science and Technology Vol. 4(5), pp. N30

Nan, H.S., Hu, X.Y. and Tian, H.W. (2019) *Recent Advances in Perovskite Oxides for Anion-Intercalation Supercapacitor: A Review*. Materials Science in Semiconductor Processing, Vol. 94, pp. 35-50.

Nashed, O., Koh, J.C.H. and Lal, B. (2016) *Physical-Chemical Properties of Aqueous TBAOH Solution for Gas Hydrates Promotion*. Procedia Engineering, Vol. 148, pp. 1351–1356.

Nomura, K., Takagi, A., Kamiya, T., Ohta, H., Hirano, M. and Hosono, H. (2006) *Amorphous Oxide Semiconductors for High-Performance Flexible Thin-Film Transistors.* Japanese Journal of Applied Physics, Vol. 45(5S), pp. 4303.

Novoselov, K.S., Geim, A.K., Morozov, S.V., Jiang, D.E., Zhang, Y., Dubonos, S.V., Grigorieva, I.V. and Firsov, A.A. (2004) *Electric Field Effect in Atomically Thin Carbon Films*. Science, Vol. 306(5696), pp. 666-669.

Novoselov, K.S., Geim, A.K., Morozov, S.V., Jiang, D., Katsnelson, M.I., Grigorieva, I.V., Dubonos, S. and Firsov, A.A. (2005) *Two-Dimensional Gas of Massless Dirac Fermions in Graphene.* Nature, Vol. 438(7065), pp. 197-200.

Ogino, H., Matsumura, Y., Katsura, Y., Ushiyama, K., Horii, S., Kishio, K. and Shimoyama, J.I. (2009) *Superconductivity at 17 K in (Fe_2P_2)($Sr_4Sc_2O_6$): A New Superconducting Layered Pnictide Oxide with A Thick Perovskite Oxide Layer.* Superconductor Science and Technology, Vol. 22(7), pp. 075008.

Osada, M., and Sasaki, T. (2009) *Exfoliated Oxide Nanosheets: New Solution to Nanoelectronics.* Journal of Materials Chemistry, Vol. 19(17), pp. 2503–2511.

Osada, M., Akatsuka, K., Ebina, Y., Kotani, Y., Ono, K., Funakubo, H., Ueda, S., Kobayashi, K., Takada, K. and Sasaki, T. (2008) *Langmuir-Blodgett Fabrication of Nanosheet-Based Dielectric Films Without an Interfacial Dead Layer*. Japanese Journal of Applied Physics, Vol. 47(9S), pp. 7556.

Osada, M., Akatsuka, K., Ebina, Y., Funakubo, H., Ono, K., Takada, K. and Sasaki, T. (2010) *Robust High-κ Response in Molecularly Thin Perovskite Nanosheets*. ACS Nano, Vol. 4(9), pp. 5225–5232.

Osada, M., Takanashi, G., Li, B.W., Akatsuka, K., Ebina, Y., Ono, K., Funakubo, H., Takada, K. and Sasaki, T. (2011) *Controlled Polarizability of One-Nanometer-Thick Oxide Nanosheets for Tailored, High- κ Nanodielectrics*. Advanced Functional Materials, Vol. 21(18), pp. 3482–3487.

Osada, M. and Sasaki, T. (2018) *Nanoarchitectonics in Dielectric/Ferroelectric Layered Perovskites: From Bulk 3D Systems to 2D Nanosheets*. Dalton Transactions, Vol. 47(9), pp. 2841-2851.

Oswald, S. (2015) *Binding Energy Referencing for XPS In Alkali Metal-Based Battery Materials Research (I): Basic Model Investigations*. Applied Surface Science, Vol. 351, pp. 492–503.

Ozbay, S., Erdogan, N., Erden, F., Ekmekcioglu, M., Ozdemir, M., Aygun, G. and Ozyuzer, L. (2020) *Surface Free Energy Analysis Of ITO/Au/ITO Multilayer Thin Films on Polycarbonate Substrate by Apparent Contact Angle Measurements*. Applied Surface Science, Vol. 529, pp. 147111.

Paniagua, S.A., Hotchkiss, P.J., Jones, S.C., Marder, S.R., Mudalige, A., Marrikar, F.S., Pemberton, J.E. and Armstrong, N.R. (2008) *Phosphonic Acid Modification of Indium-Tin Oxide Electrodes: Combined XPS/UPS/ Contact Angle Studies*. The Journal of Physical Chemistry C, Vol. 112(21), pp. 7809–7817.

Park, B. and Abu-Lail, N.I. (2011) *The Role of The PH Conditions of Growth on The Bioadhesion of Individual and Lawns of Pathogenic Listeria Monocytogenes Cells*. Journal of colloid and interface science, Vol. 358(2), pp. 611–620.

Pease, R.F. and Chou, S.Y. (2008) *Lithography and Other Patterning Techniques for Future Electronics*. Proceedings of the IEEE, Vol. 96(2), pp. 248–270.

Perreault, F., De Faria, A.F., Nejati, S. and Elimelech, M. (2015) *Antimicrobial Properties of Graphene Oxide Nanosheets: Why Size Matters*. ACS Nano, Vol. 9(7), pp. 7226–7236.

Pfeiffer, H.C. (2010) *Direct Write Electron Beam Lithography: A Historical Overview*. Photomask Technology 2010, Vol. 7823, pp. 782316.

Pimpin, A. and Srituravanich, W. (2012) *Reviews on Micro- and Nanolithography Techniques and Their Applications*. Engineering Journal, Vol. 16(1), pp. 37–55.

Przykaza, K., Woźniak, K., Jurak, M., Wiącek, A.E. and Mroczka, R. (2019) *Properties of the Langmuir and Langmuir–Blodgett Monolayers of Cholesterol-Cyclosporine A On Water and Polymer Support*. Adsorption, Vol. 25(4), 923–936.

Rondinelli, J.M., May, S.J. and Freeland, J.W. (2012) *Control of Octahedral Connectivity in Perovskite Oxide Heterostructures: An Emerging Route to Multifunctional Materials Discovery*. MRS bulletin, Vol. 37(3), pp. 261–270.

Sasaki, T. and Watanabe, M. (1998) *Osmotic Swelling to Exfoliation. Exceptionally High Degrees of Hydration of a Layered Titanate*. Journal of the American Chemical Society, Vol. 120(19), pp. 4682–4689.

Schaak, R.E. and Mallouk, T.E. (2002) *Perovskites by Design: A Toolbox of Solid-State Reactions*. Chemistry of Materials, Vol. 14(4), pp. 1455–1471.

Scott, J. F. (1998) *High-Dielectric Constant Thin Films for Dynamic Random Access Memories (DRAM)*. Annual review of materials science, Vol. *28*(1), pp. 79-100.

Sekine, Y., Akiyoshi, R. and Hayami, S. (2022) *Recent Advances in Ferroelectric Metal Complexes*. Coordination Chemistry Reviews, Vol. 469, pp. 214663.

Shangguan, W. and Yoshida, A. (2001) *Modification of the Interlayer in $K[Ca_2Na_{n-3}Nb_nO_{3n+1}]$ and Their Photocatalytic Performance for Water Cleavage*. Journal of Materials Science, Vol. 36(20), pp. 4989–4993.

Shen, J., He, Y., Wu, J., Gao, C., Keyshar, K., Zhang, X., Yang, Y., Ye, M., Vajtai, R., Lou, J. and Ajayan, P.M. (2015) *Liquid Phase Exfoliation of Two-Dimensional Materials by Directly Probing and Matching Surface Tension Components*. Nano letters, 15(8), pp. 5449-5454.

Shimizu, K.I., Tsuji, Y., Hatamachi, T., Toda, K., Kodama, T., Sato, M. and Kitayama, Y. (2004) *Photocatalytic water splitting on hydrated layered perovskite tantalate $A_2SrTa_2O_7 \cdot nH_2O$ (A = H, K, and Rb)*. Physical Chemistry Chemical Physics, Vol. 6(5), pp. 1064-1069.

Swint, A.L. and Bohn, P.W. (2004) *Effect of Acidic and Basic Surface Dipoles on The Depletion Layer of Indium Tin Oxide as Measured by In-Plane Conductance*. Applied Physics Letters, Vol. 84(1), pp. 61–63.

Szafran, K., Jurak, M., Mroczka, R. and Wiącek, A.E. (2022) *Surface Properties of The Polyethylene Terephthalate (PET) Substrate Modified with The Phospholipid-Polypeptide-Antioxidant Films: Design of Functional Biocoatings*. Pharmaceutics, Vol. 14(12), pp. 2815.

Tang, P., Han, L., Li, P., Jia, Z., Wang, K., Zhang, H., Tan, H., Guo, T. and Lu, X. (2019) *Mussel-Inspired Electroactive and Antioxidative Scaffolds with Incorporation of Polydopamine-Reduced Graphene Oxide for Enhancing Skin Wound Healing*. ACS applied materials & interfaces, Vol. 11(8), pp. 7703-7714.

Van Oss, C.J. (2006) *Interfacial forces in aqueous media*, 2nd edition. Boca Raton: CRC press.

Wang, L., Zhang, S., Wang, Q., Chen, J., Jiang, W. and Chen, R.T. (2009) *Fabrication of Three-Dimensional (3D) Woodpile Structure Photonic Crystal with Layer by Layer E-Beam Lithography*. Applied Physics A, Vol. 95, pp. 329–334.

Wang, C., Osada, M., Ebina, Y., Li, B.W., Akatsuka, K., Fukuda, K., Sugimoto, W., Ma, R. and Sasaki, T. (2014) *All-Nanosheet Ultrathin Capacitors Assembled Layer-By-Layer via Solution-Based Processes*. ACS nano, Vol. 8(3), pp. 2658–2666.

Wang, Q., Yang, D., Qiu, Y., Zhang, X., Song, W. and Hu, L. (2018) *Two-Dimensional ZnO Nanosheets Grown on Flexible ITO-PET Substrate for Self-Powered Energy-Harvesting Nanodevices*. Applied Physics Letters, Vol. 112(6), pp. 063906.

Wu, S. (1971) *Calculation of Interfacial Tension in Polymer Systems*. Journal of Polymer Science Part C: Polymer Symposia, Vol. 34(1), pp. 19–30. New York: Wiley Subscription Services, Inc., A Wiley Company.

Xiong, P., Ma, R., Wang, G. and Sasaki, T. (2019) *Progress and Perspective on Two-Dimensional Unilamellar Metal Oxide Nanosheets and Tailored Nanostructures from Them for Electrochemical Energy Storage*. Energy Storage Materials, Vol. 19, pp. 281–298.

Yadav, N., Dubey, A., Shukla, S., Saini, C.P., Gupta, G., Priyadarshini, R. and Lochab, B. (2017) *Graphene Oxide-Coated Surface: Inhibition of Bacterial Biofilm Formation Due to Specific Surface-Interface Interactions*. ACS Omega, Vol. 2(7), pp. 3070–3082.

Yadav, N., Kumar, N., Prasad, P., Shirbhate, S., Sehrawat, S. and Lochab, B. (2018) *Stable Dispersions of Covalently Tethered Polymer Improved Graphene Oxide Nanoconjugates as An Effective Vector for SiRNA Delivery*. ACS applied materials & interfaces, Vol. 10(17), pp. 14577–14593.

Yim, H., Yoo, S.Y., Kim, Y.H., Chae, K.H., Kim, Y.H., Kim, S.K., Baek, S.H., Lee, C.H. and Choi, J.W. (2021) *Defect-Controlled, Scalable Layer-by-Layer*

Assembly of High-κ Perovskite Oxide Nanosheets for All Two-Dimensional Nanoelectronics. Chemistry of Materials, 33(22), pp. 8685-8692.

Yin, F., Hu, K., Chen, Y., Yu, M., Wang, D., Wang, Q., Yong, K.T., Lu, F., Liang, Y. and Li, Z. (2017) *SiRNA Delivery with PEGylated Graphene Oxide Nanosheets for Combined Photothermal and Genetherapy for Pancreatic Cancer*. Theranostics, Vol. 7(5), pp. 1133.

Yuan, H., Lubbers, R., Besselink, R., Nijland, M. and Ten Elshof, J.E. (2014) *Improved Langmuir–Blodgett Titanate Films via in Situ Exfoliation Study and Optimization of Deposition Parameters*. ACS applied materials & interfaces, Vol. 6(11), pp. 8567–8574.

Yuan, H., Timmerman, M., van de Putte, M., Gonzalez Rodriguez, P., Veldhuis, S. and ten Elshof, J.E. (2016) *Self-Assembly of Metal Oxide Nanosheets at Liquid–Air Interfaces in Colloidal Solutions*. The Journal of Physical Chemistry C, Vol: 120(44), pp. 25411–25417.

Zhang, X., Ge, J., Xue, Y., Lei, B., Yan, D., Li, N., Liu, Z., Du, Y. and Cai, R. (2015) *Controlled Synthesis of Ultrathin Lanthanide Oxide Nanosheets and Their Promising PH-Controlled Anticancer Drug Delivery*. Chemistry-A European Journal, Vol. 21(34), pp. 11954–11960.

Zhang, K., Feng, Y., Wang, F., Yang, Z. and Wang, J. (2017) *Two Dimensional Hexagonal Boron Nitride (2D-Hbn): Synthesis, Properties And Applications*. Journal of Materials Chemistry C, Vol. 5(46), pp. 11992-12022.

Zhang, X., Cai, X., Jin, K., Jiang, Z., Yuan, H., Jia, Y., Wang, Y., Cao, L. and Zhang, X. (2019) *Determining the Surface Tension of Two-Dimensional Nanosheets by A Low-Rate Advancing Contact Angle Measurement*. Langmuir, Vol. 35(25), pp. 8308–8315.

Zhang, P., Fu, Y., Zhang, X., Zhang, X., Li, B.W. and Nan, C.W. (2022) *Flexible High-Performance Microcapacitors Enabled by All-Printed Two-Dimensional Nanosheets*. Science Bulletin, Vol. 67(24), pp. 2541-2549.

Zheng, B., Mao, L., Shi, J., Chen, Q., Hu, Y., Zhang, G., Yao, J. and Lu, Y. (2021) *Facile Layer-by-Layer Self-Assembly of 2D Perovskite Niobate and Layered Double Hydroxide Nanosheets for Enhanced Photocatalytic Oxygen Generation*. International Journal of Hydrogen Energy, Vol. 46(69), pp. 34276-34286.

Zheng, S., Bawazir, M., Dhall, A., Kim, H.E., He, L., Heo, J. and Hwang, G. (2021) *Implication of Surface Properties, Bacterial Motility, and Hydrodynamic Conditions*

on Bacterial Surface Sensing and Their Initial Adhesion. Frontiers in Bioengineering and Biotechnology, Vol. 9, pp. 643722.